

**Improved Mass Spectrometry-Based Approaches to Screening and Structural Analysis in
Drug Development**

by

LeeAnne Wang

A dissertation submitted in partial fulfillment
of the requirements for the degree of
Doctor of Philosophy
(Chemistry)
in the University of Michigan
2022

Doctoral Committee:

Professor Kristina Håkansson, Chair
Professor Robert T. Kennedy
Professor Brandon T. Ruotolo
Professor Anna S. Schwendeman

LeeAnne Wang

leeanne@umich.edu

ORCID iD: 0000-0002-2793-4693

© LeeAnne Wang 2022

To AFN my TLC

Acknowledgements

My journey in chemistry would not have been possible without the many talented and brilliant individuals guiding me. First, I must thank my advisor, Dr. Kristina Håkansson for her support and mentorship as well as my doctoral committee members Professor Robert T. Kennedy, Professor Brandon T. Ruotolo, and Professor Anna Schwendeman for their valuable insight and feedback in helping me meet the graduation requirements. Special thanks to all Håkansson lab members past and present: James Brunemann, Steven DeFiglia, Dr. Eunju Jang, Dr. Hye Kyong Kweon, Dr. Nhat Le, Josh Salem, Carson Szot, and Dr. Qingyi Wang. Going through the shutdown really made me appreciate all the time we spend together, and I cannot imagine graduate life without it.

I am eternally grateful for my collaborators Dr. Natalija Cernaka, Dr. Stephanie Chun, and Angela Fan for sharing their joy in science and patience while we drowned in plates. Special thanks to team Merck SSF for the many invaluable conversations and lifelong companions that helped me figure out where I want to go next. Additionally, none of this work would have been possible without funding from the Agilent Thought Leader Award, NIH grants, Winter Departmental Fellowship, Rackham Travel Grant, and Rackham Doctoral Intern Fellowship.

Certainly, I would not be who I am today if not for the many scientists and specialists on the other end of the phone providing support. Sincere thanks to Stephen Coales, Kyle Murray, and Tom Tobien from Trajan and Malvina Papanastasiou from the Broad Institute for taking the time

to welcome me into the HDX community and their kind encouragement. The three-letter acronym that ties us together does not even begin to untangle the many moving parts involved.

Living in Michigan for five years has been the longest I have been away from home in California, and I am hugely grateful to the people who have contributed to this personally and intellectually stimulating time in my life. I would like to thank my mom, older brothers, and Oma for their eternal support; as well as my forever partner Charlie, without whom my world would be less blue. I am so excited and delighted for our future and all the adventures that await!

31 July 2022

Table of Contents

Dedication.....	ii
Acknowledgements.....	iii
List of Tables	ix
List of Figures.....	x
List of Equations	xiv
List of Abbreviations	xv
Abstract.....	xviii
Chapter 1: Introduction.....	1
1.1 Directed Evolution for Biocatalysis	1
1.2 Antibody Drug-Conjugates (ADCs).....	3
1.3 Mass Spectrometry Sample Introduction and Ionization	7
1.3.1 Droplet-MS.....	8
1.3.2 Electrospray Ionization.....	9
1.3.3 Supercharging in Electrospray Ionization	11
1.4 Mass Spectrometry Instrumentation.....	13
1.4.1 Triple-Quadrupole Mass Spectrometry	13
1.4.2 Quadrupole-Time-of-Flight Mass Spectrometry	14
1.4.3 Fourier Transform Ion Cyclotron Resonance Mass Spectrometry.....	14
1.4.4 Orbitrap Fourier Transform Mass Spectrometry.....	17
1.5 Tandem Mass Spectrometry (MS/MS)	18
1.5.1 Collision Induced Dissociation (CID).....	19

1.5.2 Electron Transfer Dissociation (ETD).....	20
1.6 Hydrogen/Deuterium Exchange (HDX).....	21
1.7 Dissertation Overview.....	23
Chapter 2: Droplet Microfluidics-Mass Spectrometry for Whole Cell High Throughput Screening of Saxitoxin Biosynthetic Enzyme Directed Evolution Towards Non-Native Substrates in Chemoenzymatic Synthesis	25
2.1 Introduction.....	25
2.2 Experimental Methods	27
2.2.1 Chemicals and Reagents.....	27
2.2.2 Whole-cell library reactions with <i>M. wollei</i> ACP-AONS-didomain variants	27
2.2.3 Droplet Generation from Multi-well Plate (MWP).....	28
2.2.4 Simulated Conversion Standards.....	29
2.2.5 MS Analysis	30
2.3 Results and Discussion.....	31
2.3.1 Droplet Generation and Assay Optimization	31
2.3.2 MS Optimization	35
2.3.3 Screening results.....	37
2.4 Conclusions	39
Chapter 3: Structure-Activity Relationships for Cathepsin-Mediated Release of Model Amine-Containing Payloads from Cleavable Linker Conjugates.....	41
3.1 Introduction	41
3.2 Experimental Methods	43
3.2.1 Chemicals and Reagents.....	43
3.2.2 Enzyme Assay	44
3.2.3 LC-MS Analysis.....	45
3.3 Results and Discussion.....	46

3.3.1 Cleavage of Gly-Gly-Phe-Gly Aniline Substrates	46
3.3.2 Cleavage of Gly-Gly-Phe-Gly-Aliphatic and Benzylic Amine Substrates	50
3.3.3 Cleavage of peptide conjugates other than GGFG	55
3.3.4 Cleavage of Gly-Gly-Phe-Gly conjugates with other peptidases.....	58
3.4 Conclusions	59
Chapter 4: Supercharging in Hydrogen/Deuterium Exchange-Mass Spectrometry Workflows for Increased Antibody Sequence Coverage and Electron-Transfer Dissociation Efficiency.....	61
4.1 Introduction	61
4.2 Experimental Methods	62
4.2.1 Chemicals and Reagents.....	62
4.2.2 Offline pepsin digestion	62
4.2.3 Mixing Tee	63
4.2.4 LC-MS Parameters	64
4.2.5 Database search parameters.....	66
4.3 Results and Discussion.....	66
4.3.1 Increased Average Charge State MS1	66
4.3.2 Improved Sequence Coverage and PSM count	69
4.3.3 Supercharging Effects in ETD MS/MS of Antibody Peptic Peptides.....	71
4.4 Conclusions	75
Chapter 5: Conclusions and Future Directions	76
5.1 Dissertation Summary	76
5.2 Future Directions.....	77
5.2.1 Continuous Droplet Generation.....	77
5.2.2 Determining Efficient Cathepsin-Mediated Release in vivo.....	79
5.2.3 Supercharging Automated HDX for Ion Mobility-MS	80
Appendix.....	81

Bibliography 132

List of Tables

Table 2-1 SRM Parameters for whole-cell reaction monitoring by droplet-MS	31
Table 3-1 CatB-mediated cleavage of GGFG-Anilides.....	47
Table 3-2 CatB mediated cleavage of GGFG-alkylamines	51
Table 3-3 CatB mediated cleavage of GGFG-benzylamines.....	53
Table 3-4 CatB mediated cleavage of peptide conjugates with 40a	56
Table 4-1 LC HCD MS/MS outcome for IgG1 pepsin digests with and without SCA.....	70
Table 4-2 LC HCD MS/MS outcome for Herceptin pepsin digest with and without SCA.....	70
Table 4-3 LC HCD MS/MS outcome for Remicade pepsin digest with and without SCA.....	71

List of Figures

Figure 1-1 Molecular biology workflow for directed evolution. Beginning with a gene of interest, a mutant library is generated. Subsequently, the mutant genes are expressed to conduct an activity assay in which variants demonstrating desirable properties are isolated and undergo further rounds of directed evolution ⁸	2
Figure 1-2 Schematic representation of an ADC.....	4
Figure 1-3 Selected examples of cathepsin cleavable linker payloads for FDA approved ADCs. Cleavage site highlighted in red.....	5
Figure 1-4 PABC elimination reaction mechanism for payload release.....	6
Figure 1-5 Schematic of parallel droplet generation (a) and direct infusion of segmented droplets (b) ⁴⁶	8
Figure 1-6 Schematic representation of ESI process in positive mode ⁵⁸	9
Figure 1-7 ESI process models: (a) ion evaporation model (IEM), (b) charged residue model (CRM), and (c) chain ejection model (CEM) ⁶⁰	10
Figure 1-8 Cartoon representation of native protein ESI without (A-D) and with (E-H) supercharging ⁶³	11
Figure 1-9 Three CEM scenarios of an unfolded protein from a 47+ droplet. Normal conditions of a 10+ protein lead to H ⁺ migration from the droplet onto the protein chain until ejection at 23+ (a). Normal conditions of a 33+ protein undergoing reverse H ⁺ migration before ejection at 23+ (b). Supercharged ESI conditions of a 33+ protein where reverse H ⁺ migration is suppressed due to SCA forming charge-dipole contacts stabilizing H ⁺ on ejecting protein generating a supercharged 27+ protein ⁶⁴	12
Figure 1-10 Instrument schematic of Agilent 6410 triple quadrupole mass spectrometer (Agilent Technologies).....	13
Figure 1-11 Instrument schematic of Xevo G2-XS QTOF mass spectrometer (Waters Corporation).....	14
Figure 1-12 Cylindrical closed static electromagnetic ion trap highlighting detection, excitation, trapping electrodes designated D, E, and T respectively ⁷⁶	15

Figure 1-13 Schematic of positively charged ion cyclotron motion. Due to Lorenz force, ions are bent into a circular orbit perpendicular to the magnet field axis ⁷⁶	16
Figure 1-14 Instrument schematic of a 7T Solarix quadrupole FT-ICR mass spectrometer (Bruker Daltonics).	17
Figure 1-15 Instrument schematic of an Orbitrap Fusion Lumos mass spectrometer (Thermo Scientific).	18
Figure 1-16 Nomenclature of peptide fragment ions in MS/MS and corresponding tandem technique.	19
Figure 1-17 General workflow for bottom-up HDX-MS. A protein is incubated in D ₂ O for varying amounts of time before the labeling is quenched by reducing temperature and pH. The labeled protein is then proteolyzed with the resulting peptides desalted during a rapid separation. Each deuterium incorporated into the peptide results in a 1 Da mass shift to the right in the MS spectra. Comparing the plots of deuterium uptake for different conditions can provide conformational dynamics information ¹⁰¹	21
Figure 1-18 Principle of selectively labeled model peptide gas phase H/D scrambling as a result of fragmentation. When scrambling occurs, localized deuterium content is lost.	23
Figure 2-1 General reaction scheme of SxtA AONS domain converting an α -amino acid to an α -aminoketone using ACP domain-bound ketone substrate.	26
Figure 2-2 Biocatalytic platform for synthesis of tryptophan ethyl ketone 2.2. The AONS domain catalyzes decarboxylative condensation of the amino acid 2.1 with ACP domain-bound ethyl ketone loaded from thiophenyl (PhS)-ethyl ketone substrate 2.3.	27
Figure 2-3 Image of droplet generation from MWP setup. Syringe pump shown on left and XYZ-positioner with epoxied MWP shown on right.	28
Figure 2-4 Microscope image of generated droplet with micro ruler in background to determine droplet volume.	29
Figure 2-5 Triple-tube coaxial sheath flow sprayer used for droplet-MS.	30
Figure 2-6 Droplet trace of tryptophan ethyl ketone product standard with simulated 1% and 10% substrate conversion in reaction buffer (left) and simulated 1%, 2.5%, 5%, 7.5%, and 10% substrate conversion spiked into cell lysate (right).	32
Figure 2-7 Calibration curve of Trp in reaction buffer containing cell lysate. Each data point is an average of five replicates. Error bars are not visible as they are smaller than the data points.	32
Figure 2-8 Calibration curve of tryptophan ethyl ketone product in reaction buffer containing cell lysate. Each data point is an average of five replicates. Error bars are not visible as they are smaller than the data points.	33

Figure 2-9 Droplet traces of Trp ethyl ketone product for 1, 10, 5, 3, and 7% simulated conversion (in red) and Trp substrate (in blue). Sample droplet packets are separated by five blank droplets containing only reaction buffer.....	34
Figure 2-10 Figure 2 10 MS (top) and MS/MS (bottom) spectra of protonated tryptophan.	35
Figure 2-11 MS (top) and MS/MS (bottom) spectra of protonated tryptophan ethyl ketone product (WPdt).....	36
Figure 2-12 Fragmentation pathways for tryptophan (top) and its ethyl ketone product (bottom) ^{124,125}	37
Figure 2-13 Droplet trace of tryptophan (blue) and tryptophan ethyl ketone product (red) with simulated 1% conversion sample on the left followed by sample droplets from row E of plate 1. Samples analyzed in replicates of five.....	39
Figure 2-14 Droplet MS of calibration droplets (left) and potential hits of enzyme variants with some activity towards the non-native tryptophan substrate variants (right). The 1% standard (left) is equivalent to 1% conversion (10 μ M) to tryptophan ethyl ketone.....	39
Figure 3-1 Schechter and Berger nomenclature. P designates the substrate residues while S denotes the enzyme's active site ¹³²	42
Figure 3-2 Reaction mechanism for (CatB)-mediated cleavage of linker substrates. Cathepsin B cleaves the amide bond between the linker and payload (red).	42
Figure 3-3 Scheme for substrates 44 through 58.	56
Figure 3-4 Relative substrate cleavage scores with different peptidases. All data reported as an average of 3 runs.	59
Figure 4-1 Schematic representation of mixing tee used for SCA addition without impacting separation. Arrows indicate flow directionality. LC eluent was set to 200 μ L/min while <i>m</i> -NBA was infused at 10 μ L/min. All tubing was 130 μ m i.d.	64
Figure 4-2 Bar graphs representing charge state distributions for IgG1 peptic peptides without (left) and with (right) 0.1% <i>m</i> -NBA. Calculated average charge states for each are shown in the upper right of each bar graph.	67
Figure 4-3 MS1 spectra of peptide from pepsin digest of IgG1 with and without 0.1% <i>m</i> -NBA collected on a 7T SolariX Q-FT-ICR mass spectrometer.	68
Figure 4-4 IgG1 structure consisting of four units, two heavy chains and two light chains connected via disulfide bonds. Heavy chains shown in dark blue while light chains shown in yellow.	70
Figure 4-5 ETD MS/MS spectrum of the quadruply protonated peptic peptide YYCCSYAGDYTPGVVFGGGTKL from IgG1 only identified following supercharging with an XCorr score of 7.85.....	72

Figure 4-6 ETD MS/MS spectrum of the quadruply protonated peptic peptide YTLPPSRDELTKNQVSL from IgG1 with an XCorr score of 6.75. 73

Figure 4-7 ETD MS/MS spectrum of the triply protonated peptic peptide VSWNSGALTSGVHTFPAVL from IgG1 with an XCorr score of 6.08. 74

Figure 5-1 Schematic representation of continuous and simultaneous droplet generation and infusion using valves. Valves would be programmed to switch so that syringe #1 infuses droplets to the MS while syringe #2 generates droplets. Once syringe #1 empty and syringe #2 full, valves would switch. 78

Figure 5-2 Design of valve for handling droplets without disrupting droplet stability or inducing carryover^{165,166}. Dashed line indicates axis of rotation of the lavender piece. 79

List of Equations

Equation 1-1	16
Equation 1-2	17
Equation 1-3	19
Equation 1-4	20
Equation 2-1	29
Equation 4-1	66

List of Abbreviations

ACN	acetonitrile
ACP	acyl carrier protein
ADC	antibody drug conjugate
AONS	8-amino-7-oxononanoate synthase
CatB	cathepsin B
CatL	cathepsin L
CatS	cathepsin S
CE	capillary electrophoresis
CEM	charge ejection model
CI	confidence interval
CID	collision induced dissociation
CNC	computer numerical control
CRM	charge residue model
DAR	drug-to-antibody ratio
DMSO	dimethylsulfoxide
DTT	dithiothreitol
ECD	electron capture dissociation
EDTA	ethylenediaminetetraacetic acid
EIC	extracted ion chromatogram

ETD	electron transfer dissociation
ESI	electrospray ionization
FA	formic acid
FT MS	Fourier transform mass spectrometry
FT-ICR	Fourier transform-ion cyclotron resonance
HCD	higher-energy collision dissociation
HDX	hydrogen deuterium exchange
HPLC	high-performance liquid chromatography
HTS	high throughput screening
IEM	ion ejection model
i.d.	inner diameter
IPA	isopropyl alcohol
IS	internal standard
LC	liquid chromatography
LOD	limit of detection
mAb	monoclonal antibody
MeOH	methanol
<i>m</i> -NBA	<i>m</i> -nitrobenzyl alcohol
MRM	multiple reaction monitoring
MS	mass spectrometry
MS/MS	tandem mass spectrometry
MW	molecular weight
MWP	multi-well plate

<i>m/z</i>	mass-to-charge ratio
o.d.	outer diameter
PABC	<i>p</i> -aminobenzyloxycarbonyl
PCR	polymerase chain reaction
PFD	perfluorodecalin
PSM	peptide spectrum match
QQQ	triple quadrupole
QTOF	quadrupole time-of-flight
RPLC	reverse phase liquid chromatography
SAR	structure activity relationship
SCA	supercharging agent
S/N	signal-to-noise ratio
SRM	single reaction monitoring
STX	saxitoxin
TCEP	tris(2-carboxyethyl)phosphine
TE	thioester
TIC	total ion chromatogram
TOF	time-of-flight
Trp	tryptophan
UPLC	ultra performance liquid chromatography
WT	wildtype
XCorr	cross-correlation

Abstract

Mass spectrometry (MS)-based analysis is highly versatile and provides powerful tools for addressing a plentitude of analytical challenges. For example, MS allows for high-throughput screening via direct analysis of microfluidic droplets, label-free quantification of enzyme-catalyzed reactions, and probing of protein structures and stability by coupling with hydrogen/deuterium exchange (HDX).

This dissertation focuses on expanding the role of MS in drug development beginning with the development of a droplet microfluidic-MS workflow for whole cell screening of the catalytic efficiency of a saxitoxin biosynthetic enzyme for directed evolution towards non-native substrates in chemoenzymatic synthesis (Chapter 2). Specifically, variants of the polyketide-like synthase, saxitoxin biosynthetic module A (SxtA) from the cyanobacterium *Cylindrospermopsis raciborskii* T3, capable of transforming α -amino acids to α -aminoketones, are screened for activity with the non-native substrate tryptophan. Direct infusion of droplets containing whole cell lysate with overexpressed enzyme and substrates, increased screening throughput to 362 samples/h from 4 samples/h with a previous liquid chromatography (LC)-MS workflow.

A structure-activity relationship (SAR) study of cathepsin B-mediated release of model amine-containing payloads from cleavable linkers employed in antibody drug-conjugate (ADC) design is discussed in Chapter 3. While there has been significant development on linker optimization for efficient payload release, no studies to date have investigated amine substrate (i.e., drug) dependent release rates as currently available payload options are extremely limited. Our results indicate that, in addition to aniline substrates, aryl amines and substituted ortho pyridyl

methyl amines cleave at similar rates, thus eliminating the spacer requirement for efficient release and enabling access to more options for payload chemistries. In addition to the established tetrapeptide Gly-Gly-Phe-Gly, various capping groups were conjugated to the N-terminus of the dipeptide valine-citrulline (Val-Cit) and screened for efficient cathepsin-mediated release with results indicating a strong preference for capped peptides. Additional purified peptidases besides cathepsin B as well as rat liver lysosomes were included to assess substrate performance using a scoring system to determine relative rates. Our findings demonstrated that the substrates screened were enzyme agnostic.

Because the structural integrity of monoclonal antibodies (mAbs) in ADCs can be compromised by payload conjugation, characterizing changes in protein conformation and dynamics as well as stability is crucial. HDX-MS determines protein conformational changes through changes in deuterium uptake rates in peptic peptides generated following time-dependent exposure to deuterated solvents. Localization of deuterium content to individual amino acids is desired for optimum structural resolution. To accomplish such localization, electron-based tandem MS activation techniques have been shown to allow fragmentation of deuterated peptides without deuterium scrambling. However, high charge state (greater than or equal to 2+) precursor ions are required, which is problematic with pepsin digestions. Supercharging reagents such as *m*-nitrobenzyl alcohol have been shown to increase the average peptic peptide charge state for smaller standard proteins, thus allowing for more efficient fragmentation. In Chapter 4, this supercharging approach is demonstrated for antibody pepsin digests where additional peptides were identified only upon supercharging. Overall, the improved MS-based approaches for characterization and screening presented in this dissertation have implications for enabling more efficient next generation drug design.

Chapter 1: Introduction

1.1 Directed Evolution for Biocatalysis

The ability of enzymes to catalyze complex biochemical reactions with extreme stereoselectivity and efficiency makes them appealing tools to researchers to access synthetically challenging transformations commonly found in natural products, which are valued in establishing new leads in drug design¹⁻⁴. However, wild-type (WT) enzymes are often limited in their ability to transform non-native substrates, restricting industrial application^{5,6}. In order to harness the biocatalytic potential of enzymes on non-native substrates, directed evolution workflows have been developed to generate and screen large libraries of enzyme variants with mutagenesis, screening, and gene amplification being the main steps (Figure 1-1).^{7,8}

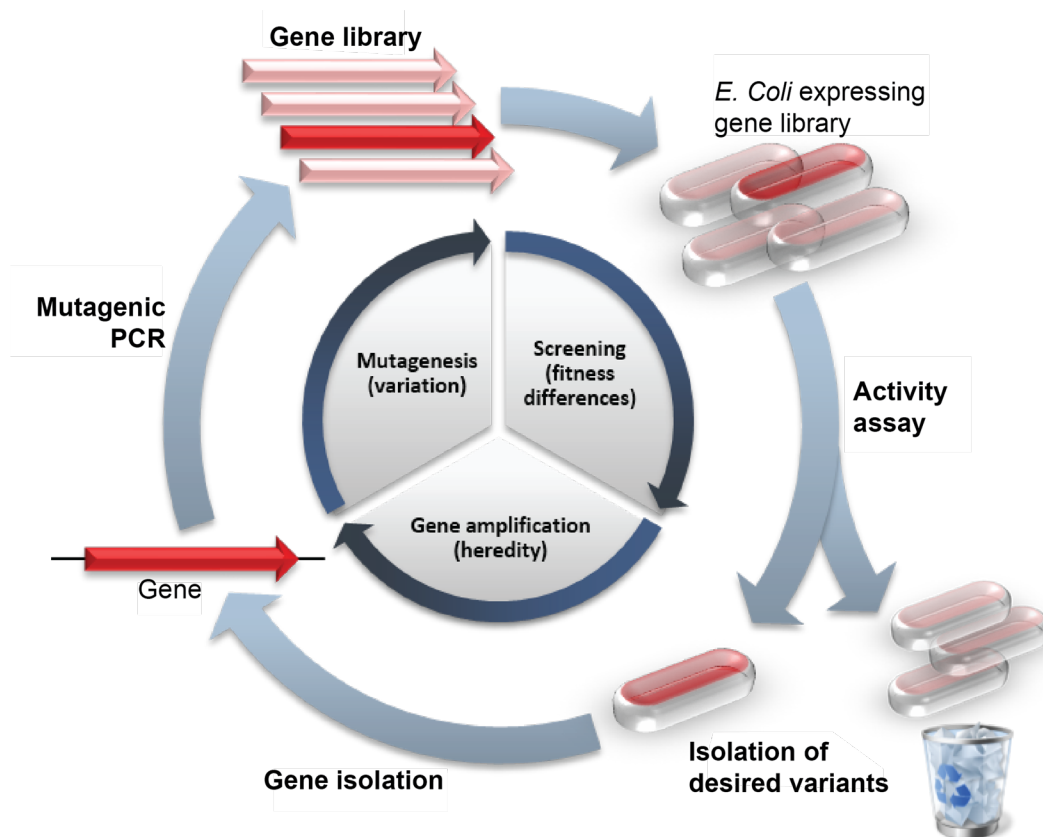


Figure 1-1 Molecular biology workflow for directed evolution. Beginning with a gene of interest, a mutant library is generated. Subsequently, the mutant genes are expressed to conduct an activity assay in which variants demonstrating desirable properties are isolated and undergo further rounds of directed evolution⁸.

While there is no shortage of methods to create large mutant libraries, the key to successful evolution relies on selecting a proper high-throughput screening (HTS) method.⁹ In contrast to nature's selection pressures to drive evolution, directed evolution does not require structural knowledge of the enzymes but instead relies on genetic diversity and effective screening strategies.¹⁰ Using error-prone polymerase chain reaction (PCR), large mutant libraries can be generated quickly while screening individual variants for desired properties can be labor-intensive.^{6,11} Current methods used for screening include liquid chromatography-mass spectrometry (LC-MS) while pH, fluorescence or absorbance measurements are more commonly

used for HTS.^{5,12} Multi-well plates (MWP) have been widely implemented to compartmentalize single transformants and can be quickly analyzed with a plate reader, but are often limited to optically based detection methods which limit the applicability or require chemical labeling.

To avoid using fluorescent tags, MS has been applied as a label-free and sensitive analytical method for enzyme activity screening. With the motivation to reduce sample consumption and increase throughput, microfluidic systems have been coupled to MS analysis specifically in the form of droplet-MS.¹³⁻¹⁷ Microfluidic droplets act as compartmentalized reaction vessels that are capable of sequential manipulations including reagent addition, splitting, and sorting. Laser-induced fluorescence is commonly utilized to analyze these sub-microliter volumes, but requires a direct correlation between fluorescence signal and analyte activity.¹⁸⁻²¹ Instead, droplets can be directly analyzed using nano-electrospray ionization (nESI) MS, which has the benefit of reducing ionization suppression caused by sample matrix.²² Several studies have even demonstrated integrating an nESI emitter directly into a chip allowing for online analysis.²³⁻²⁷ While these methods have improved the information content gained from microfluidic droplets, many biological assays are still performed in MWP and applying droplet-MS analysis can be challenging.

1.2 Antibody Drug-Conjugates (ADCs)

Antibody drug conjugates (ADCs) have become a rapidly growing class of therapeutics due to their high selectivity in delivering drugs to target cells or tissue²⁸. ADCs are composed of monoclonal antibodies (mAbs) typically conjugated to small molecule drugs (payloads) via a covalent linker (Figure 1-2).

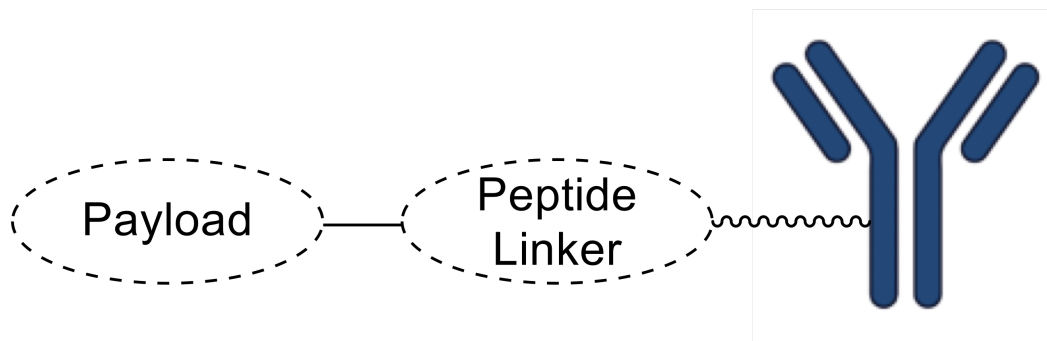


Figure 1-2 Schematic representation of an ADC.

ADCs initially showed success in cancer treatments, which had been hampered by the low therapeutic index, i.e., toxicity towards noncancerous cells, of conventional chemotherapeutic agents. Currently non-oncology ADC-based therapeutic solutions are also being explored, including conjugated steroids, antibiotics, and a variety of inhibitors as payloads²⁹.

The covalent linker is a key component in the function of ADCs, thus designing linkers that have the following characteristics is critical for success: 1) high stability in circulation, and 2) specific release of payload in the target tissue. Though linkers can vary from cleavable to non-cleavable, enzyme-specific cleavable linkers, relying on a variety of cleavage enzymes including cathepsins, glycosidases, phosphatases, and sulfatases, provide the advantage of selective intracellular cleavage and the bystander effect, in which surrounding cells that do not express antigen internalize the payload^{30,31}. By designing chemotherapeutic ADCs with cathepsin-sensitive peptide linkers, these therapeutics take advantage of lysosomal cathepsin B (CatB) overexpression in cancer cells. However, because cathepsins are expressed in all tissues this approach can potentially lead to adverse effects. Currently, there are four FDA-approved ADCs that rely on CatB cleavage of a peptide linker for release of cytotoxic warheads: Seagen's brentuximab vedotin (Adcentris®), Genentech's polatuzumab vedotin (Polivy®), Astellas Pharma

and Seagen's enfortumab vedotin (Padcev®), and Daiichi-Sankyo and AstraZeneca's trastuzumab deruxtecan (Enhertu®) (Figure 1-3)³².

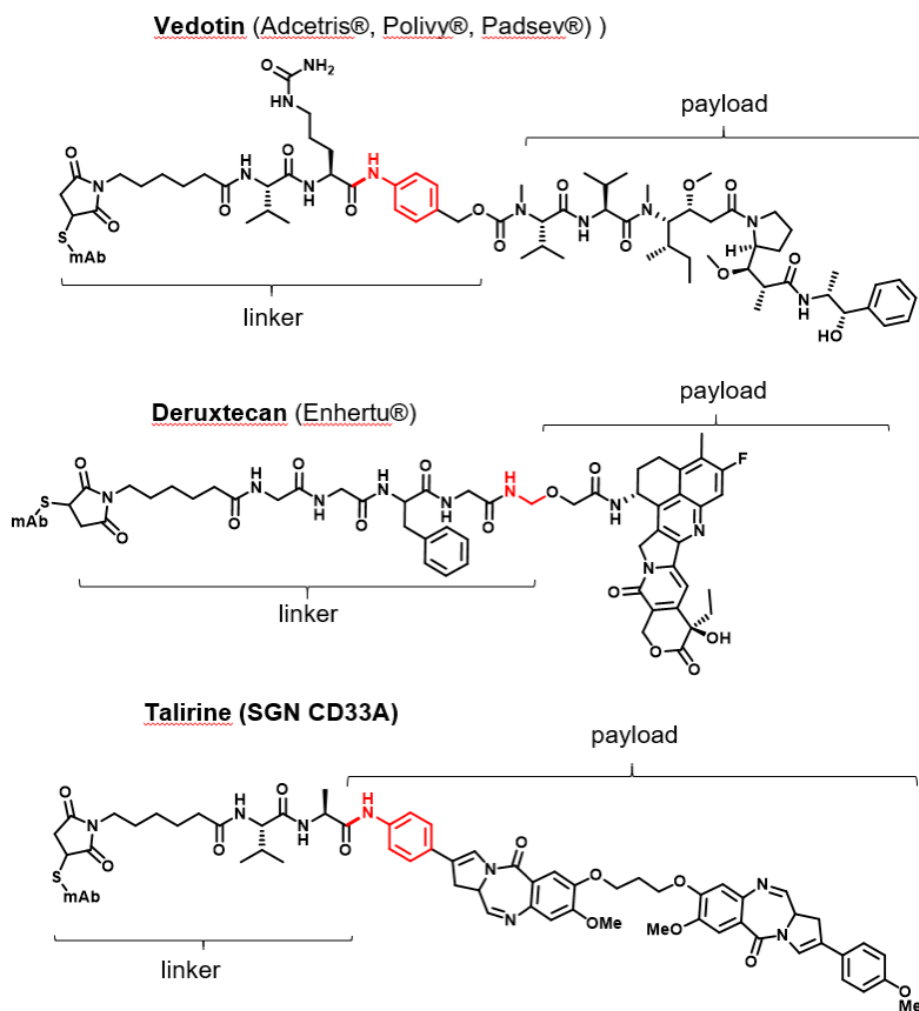


Figure 1-3 Selected examples of cathepsin cleavable linker payloads for FDA approved ADCs. Cleavage site highlighted in red.

Historically, ADC linker designs rely on spacers to aid drug release where the spacer reduces steric bulk from the drug, thus allowing CatB to access the cleavage site. The most widely used spacer is p-aminobenzyloxycarbonyl (PABC), based on the observation that anilide bonds

undergo rapid cleavage when subjected to peptidases³³. In this case, the drug molecule is modified with PABC through a carbamate connection, while the aniline amine of the PABC is connected to the cleavable peptide. Once the amide bond has been hydrolyzed, the PABC spacer undergoes a rapid 1,6-elimination to release the cytotoxic drug (Figure 1-4).

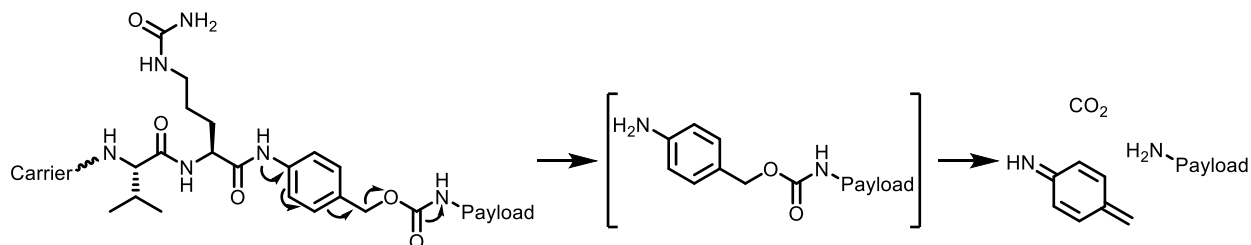


Figure 1-4 PABC elimination reaction mechanism for payload release.

The above-mentioned examples Adcentris®, Polivy®, and Padcev® all utilize a valine-citrulline (Val-Cit) dipeptide cleavable linker with a PABC spacer to release the cytotoxic drug monomethyl auristatin E (MMAE). Enhertu® uses a novel combination of glycine-glycine-phenylalanine-glycine (GGFG) tetrapeptide cleavable linker with a self-immolative amino methylene spacer for release of the sterically hindered exatecan derivative (DXd). The GGFG tetrapeptide linker was previously reported to be stable in serum circulation and selectively cleaved in the lysosomes of tumor cells via cathepsin enzymes³⁴. Some cytotoxic drug designs incorporate anilines, which could also be used for direct connection to the peptide. For example, Vadastuximab talirine (SGN-CD33A) is a highly potent ADC with synthetic DNA crosslinker pyrrolobenzodiazepine (PBD) dimers conjugated to engineered cysteine residues of an anti-CD33 mAb via a cleavable linker directly connected to the PBD molecule.

Despite growing popularity, ADCs suffer from off-target toxicity associated with non-specific payload release³⁵. Therefore, a focus of ADC development is optimizing selective drug

release in the tissue of interest³⁶. Due to the growing number of different payloads for use in ADCs, optimization of linkers takes a central part in this process³⁷. Thus, approaches focusing on the improving selectivity of peptide linkers toward specific cathepsins has gained interest in recent years. Research in this area has identified new peptide sequences such as Val-Gln and Leu-Gln that are stable in serum and cleaved by CatB at higher rates than the standard dipeptides Ala-Ala, Val-Ala, and Val-Cit. Peptidomimetic sequences have also been studied as promising ADC linkers with enhanced specificity for CatB cleavage. Specifically, a cyclobutene-1,1-dicarboxamide structure replacing the typical P2 amino acid resulted in improved recognition by the CatB active site and equivalent efficacy and stability to Val-Cit³⁸. Ultimately, the main challenge beyond optimizing the individual ADC components has been the limited number of acceptable payloads for application in ADC architecture, despite significant advances in payload potency^{39,40}. In addition to potency, the ideal payload would also exhibit high stability in storage and serum, reasonable aqueous solubility, and non-immunogenicity.^{41,42}

1.3 Mass Spectrometry Sample Introduction and Ionization

Mass spectrometry (MS) is used in a broad range of applications including pharmaceutical development and structural characterization of large biomolecules including antibodies. This wide breadth of applications is due to the powerful label-free analysis MS provides in determining mass-to-charge ratios (m/z) of molecules of interest⁴³. Advancements in technology including hardware, software, and sample preparation have enabled high sensitivity, high accuracy, and high throughput analysis of complex mixtures like biological samples^{44,45}. Coupling MS analysis to separation techniques like liquid chromatography further expands its capabilities by controlling when individual components of a mixture are introduced to the instrument.

1.3.1 Droplet-MS

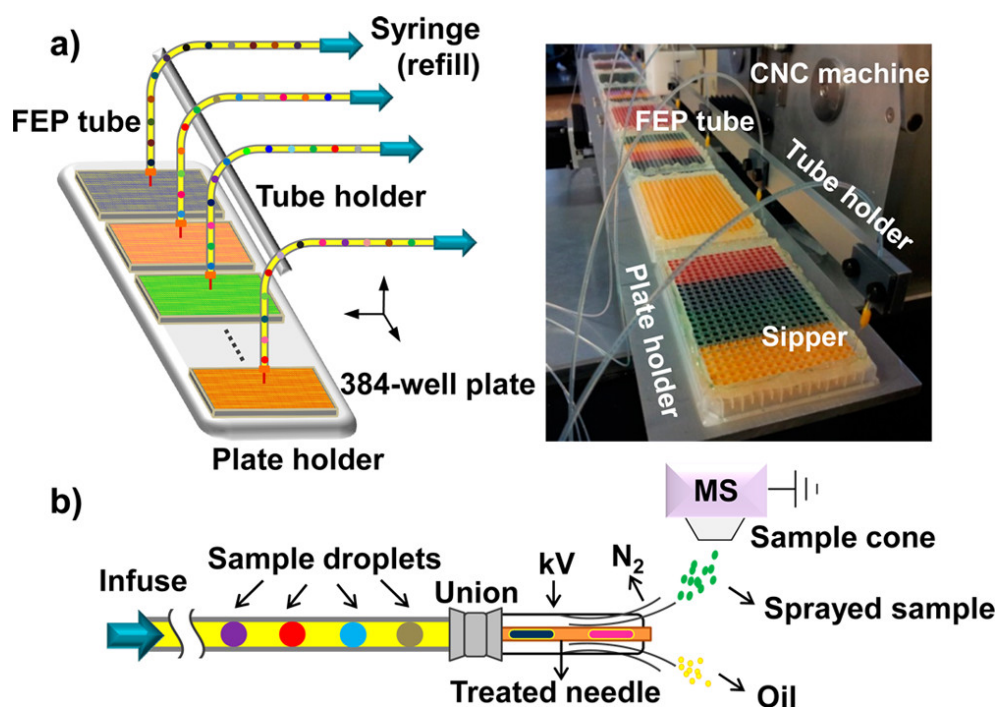


Figure 1-5 Schematic of parallel droplet generation (a) and direct infusion of segmented droplets (b)⁴⁶.

Microfluidic droplets provide the benefit of fast manipulation of low volumes (μL to pL) and the capability to be multiplexed or automated⁴⁷⁻⁴⁹. These technologies have been applied in HTS of chemical synthesis and biomedical diagnostics as well as many other areas. Discrete droplets containing aqueous sample are formed and segmented by an immiscible carrier oil and can be directly infused into the mass spectrometer. When the aqueous sample reaches the tip of the emitter, its contents will ionize and generate signal while the segmenting oil will not as it is not conductive⁵⁰. Throughputs up to 30 Hz and applications including enzyme evolution and inhibitor screening have been reported⁵¹⁻⁵³.

1.3.2 Electrospray Ionization

For MS analysis, analytes must be in the gas phase and charged which can be achieved using electrospray ionization (ESI). This soft ionization method was discovered by Fenn and coworkers along with Alexandrov and coworkers^{54,55}. In addition to generating multiply charged ions from solution, ESI is preferred for mass analyzers with limited m/z range and is readily coupled with LC⁵⁶⁻⁵⁸.

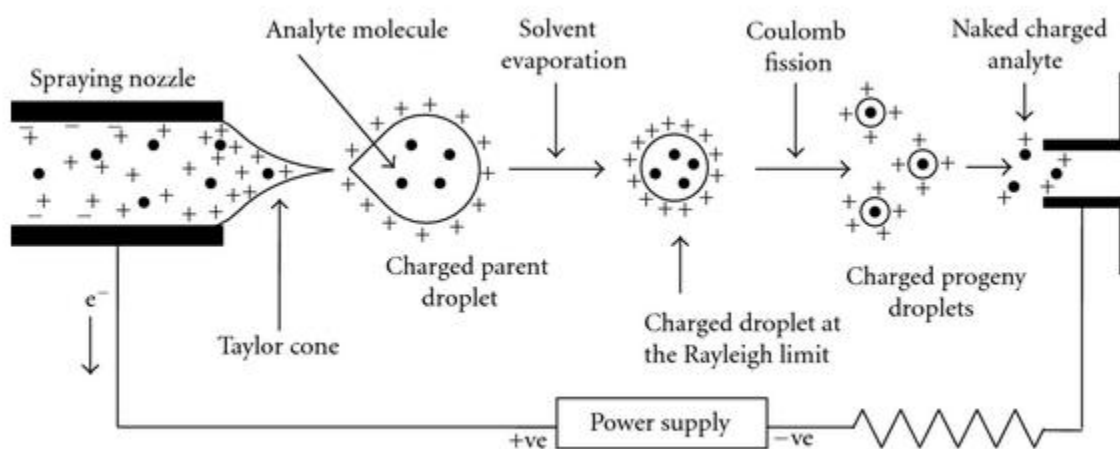


Figure 1-6 Schematic representation of ESI process in positive mode⁵⁸.

In ESI, analytes are ionized by flowing a liquid sample solution through a conductive emitter at which high voltage (2.5 – 6.0 kV) is applied. Due to the resulting electric field, charged species in solution accumulate at the emitter tip, forming a Taylor cone from the Coulomb repulsion of the accumulated like charges⁵⁸. At the tip of the Taylor cone, Coulomb destabilization disperses a fine spray of charged droplets. These droplets undergo solvent evaporation aided by nebulizing gas and elevated source temperature causing the droplets to shrink. As the droplets shrink, their charge density builds up until a balance of surface tension and Coulomb repulsion is achieved also known as the Rayleigh limit^{13,59}. When this limit is reached, droplet fission into

smaller droplets occurs generating higher charge to mass ratio compared to the original droplets (Figure 1-6). While the exact mechanism for ESI is still under debate, there are three models for ion formation: ion evaporation model (IEM), charge residue model (CRM), and chain ejection model (CEM) (Figure 1-7)⁶⁰. IEM is believed to be the mechanism for low molecular weight analytes, where relatively small ions are ejected from the Rayleigh-charged droplet surface. Large biomolecules including natively folded proteins undergo the CRM model where droplets shed solvent via evaporation. Denatured or unfolded proteins are proposed to follow the CEM model due to their extended conformation exposing hydrophobic residues that tend to drift towards the droplet surface.

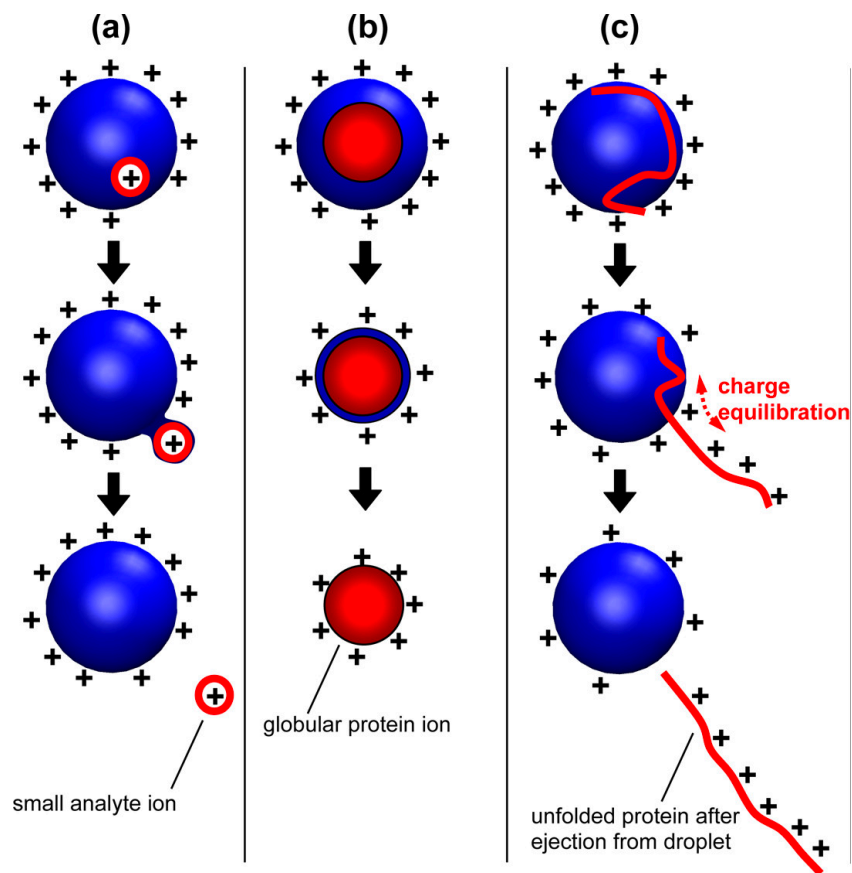


Figure 1-7 ESI process models: (a) ion evaporation model (IEM), (b) charged residue model (CRM), and (c) chain ejection model (CEM)⁶⁰.

1.3.3 Supercharging in Electrospray Ionization

Supercharging agents (SCA) like m-nitrobenzyl alcohol (m-NBA) and sulfolane, added to the ESI solvent in relatively small amounts, have been demonstrated to increase charging of small peptides^{61,62}. One proposed mechanism for protein supercharging compared to standard ESI is shown in Figure 1-8^{63,64}. When m-NBA is added, solvent segregation occurs to form an aqueous core where charge carriers Na^+ and H^+ accumulate at the interface of water and SCA. This charge sequestering reduces IEM ejection of charge carriers, trapping them on the protein after water evaporates, thus generating higher charge state analytes.

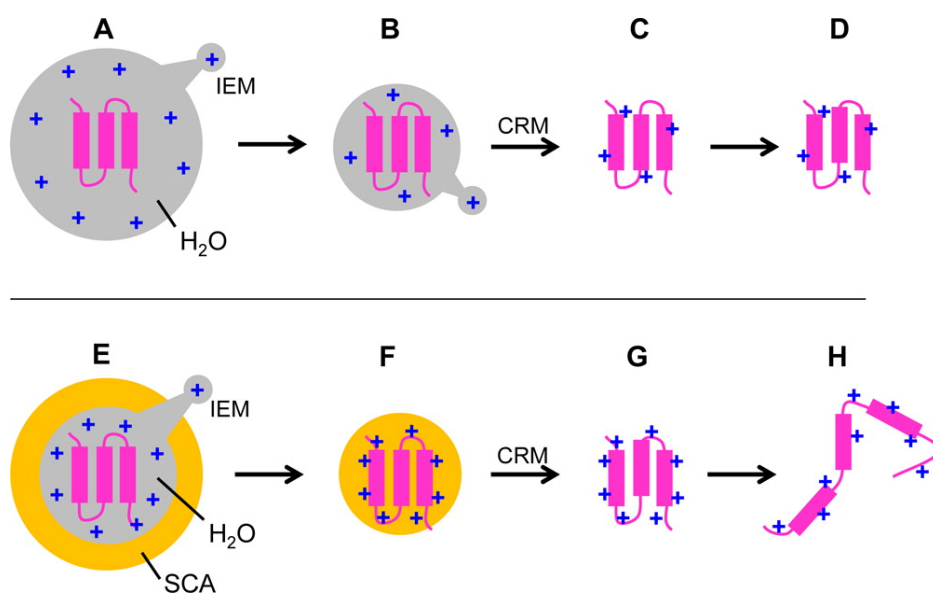


Figure 1-8 Cartoon representation of native protein ESI without (A-D) and with (E-H) supercharging⁶³.

Peptides have also been shown to undergo supercharging;^{65,66} however, because peptides do not follow the CRM, enhanced charging must have an alternative explanation. In the CEM, hydrophobic residues in proteins are exposed and hypothesized to migrate towards the droplet surface before being ejected (Figure 1-9 a, b)⁶⁴. The presence of SCA may allow the formation of

charge-dipole contacts of the exposed protein chain, suppressing reverse H⁺ migration to generate a supercharged analyte (Figure 1-9 c). This scenario may also apply to peptides which are generally unstructured in solution.

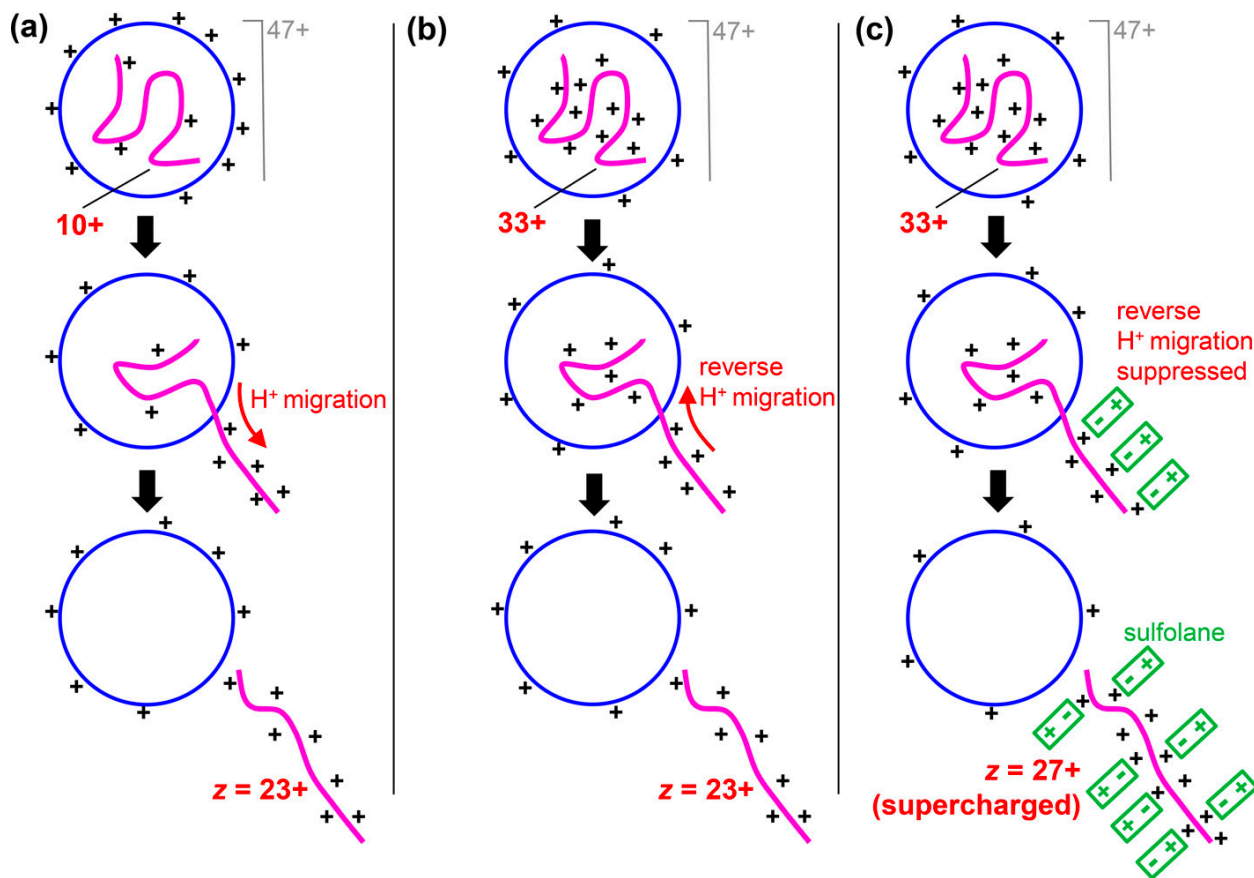


Figure 1-9 Three CEM scenarios of an unfolded protein from a 47+ droplet. Normal conditions of a 10+ protein lead to H⁺ migration from the droplet onto the protein chain until ejection at 23+ (a). Normal conditions of a 33+ protein undergoing reverse H⁺ migration before ejection at 23+ (b). Supercharged ESI conditions of a 33+ protein where reverse H⁺ migration is suppressed due to SCA forming charge-dipole contacts stabilizing H⁺ on ejecting protein generating a supercharged 27+ protein⁶⁴.

1.4 Mass Spectrometry Instrumentation

1.4.1 Triple-Quadrupole Mass Spectrometry

First reported in 1978 by Yost and Enke, the triple quadrupole mass spectrometer (QqQ) has remained a staple for quantitative applications requiring both sensitivity and selectivity^{67,68}. Each quadrupole consists of four parallel rods where specific DC and RF voltages are applied that allow for transmission of selected m/z values. The three quadrupoles arranged in series enable single and multiple reaction monitoring (SRM/MRM) which can be used for quantification of complex mixtures when using the second quadrupole (or higher order multipole) as a collision cell (Figure 1-10). SRM analysis, i.e., detection of a single fragment ion from known precursor ion m/z values, on an Agilent 6410 QqQ was used for the work discussed in Chapter 2 in place of liquid chromatography prior to MS analysis. Even though the resolution achieved on a QqQ is not the highest possible, these instruments are robust, relatively inexpensive, and offer high sensitivity, and unprecedented dynamic range⁶⁹.

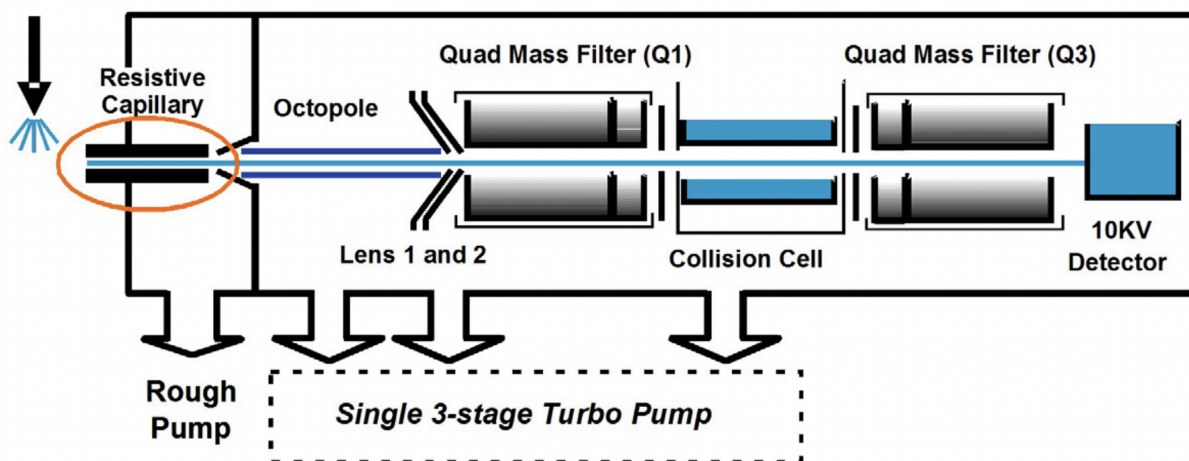


Figure 1-10 Instrument schematic of Agilent 6410 triple quadrupole mass spectrometer (Agilent Technologies).

1.4.2 Quadrupole-Time-of-Flight Mass Spectrometry

Replacing the third quadrupole in a QqQ with a time-of-flight mass analyzer (qTOF) generates a hybrid mass spectrometer that can achieve high resolution mass measurements (Figure 1-11). Additional benefits of a TOF compared to a QqQ are the significantly higher mass accuracy and faster acquisition speed. This higher mass accuracy enables higher confidence analysis, i.e., the need for fragmentation and subsequent time for method optimization were eliminated for the work covered in Chapter 3.

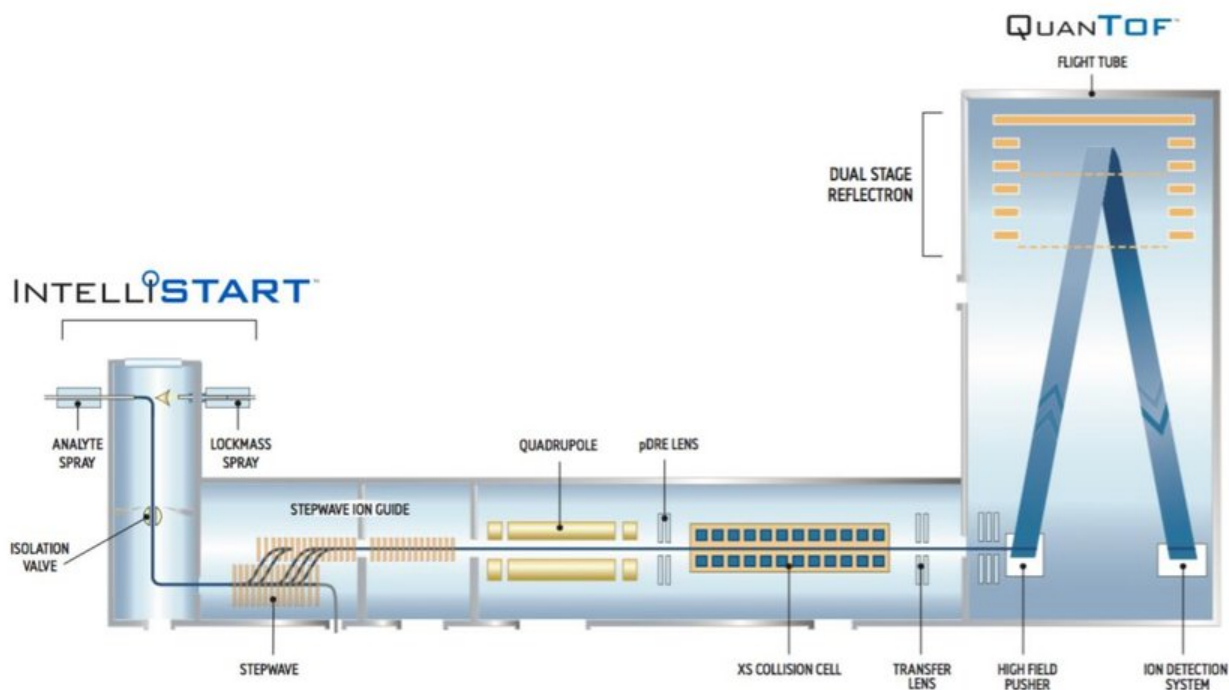


Figure 1-11 Instrument schematic of Xevo G2-XS QTOF mass spectrometer (Waters Corporation).

1.4.3 Fourier Transform Ion Cyclotron Resonance Mass Spectrometry

In 1974, Comisarow and Marshall published the first paper describing Fourier transform ion cyclotron resonance (FT-ICR) mass spectrometry⁷⁰. The key advantage compared to other

mass analyzers is its high resolution and accuracy which have established its extensive use in life science and petrochemicals applications^{71,72}. The components of an FT-ICR instrument include a superconducting magnet, ultrahigh vacuum, and an analyzer cell. The resolution is dependent on magnetic field strength with advantages at higher field strengths including improved mass resolving power, longer ion trapping duration, more trapped ions, and improved upper mass limit⁷³. The ICR cell is a critical component where ions are trapped and detected with the cell design being composed of two excitation plates, two detection plates, and two trapping plates (Figure 1-12)⁷⁴. The ions trapped within the cell undergo cyclotron motion (Figure 1-13), magnetron motion, and trapping motion due to the applied magnetic and electric fields⁷⁵.

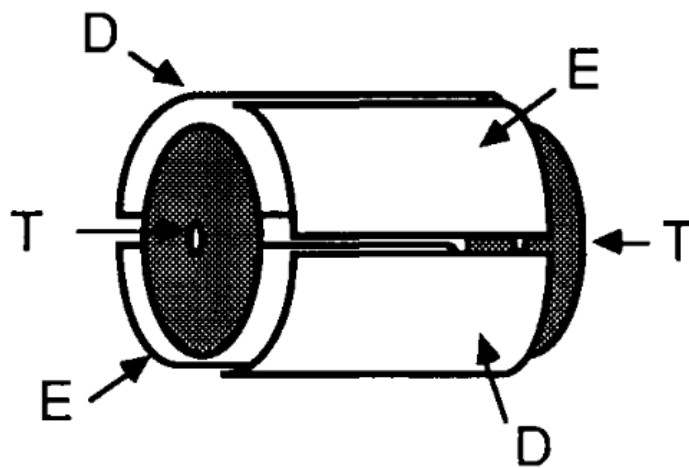


Figure 1-12 Cylindrical closed static electromagnetic ion trap highlighting detection, excitation, trapping electrodes designated D, E, and T respectively⁷⁶.

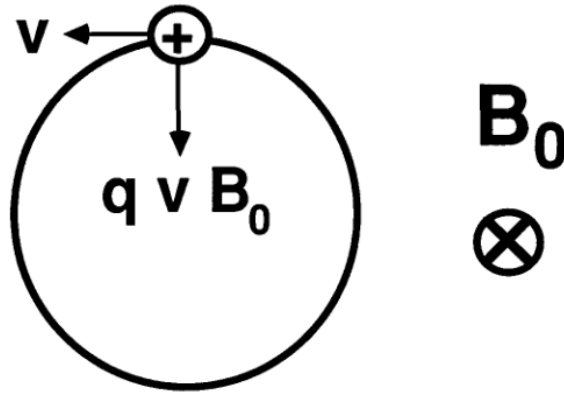


Figure 1-13 Schematic of positively charged ion cyclotron motion. Due to Lorenz force, ions are bent into a circular orbit perpendicular to the magnet field axis⁷⁶.

The equation for angular cyclotron motion (ω) is as follows:

Equation 1-1

$$\omega = \frac{q}{m} B_0$$

where q is the analyte charge, B_0 is the magnetic field strength, and m is the analyte mass. Since the radius of this cyclotron motion depends on the ion's kinetic energy whereas its frequency does not, high resolution is achieved⁷⁷.

Ions additionally undergo axial oscillation due to the trapping electric field (Figure 1-12) leading to the combination of electric and magnetic fields generating ion magnetron motion. This motion defines the reduced cyclotron frequency which can be detected by applying a rapid frequency sweep so that ions with matching cyclotron frequencies pass the detection plates inducing a sinusoidal image current. Using a Fourier transformation, the time domain transient is converted to the frequency domain ultimately generating a mass spectrum.

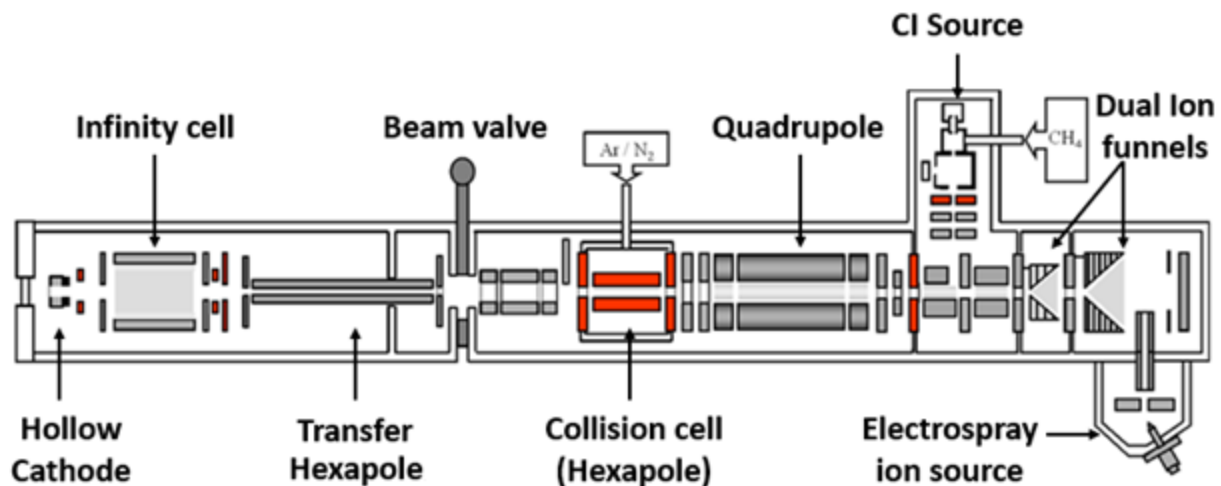


Figure 1-14 Instrument schematic of a 7T Solarix quadrupole FT-ICR mass spectrometer (Bruker Daltonics).

1.4.4 Orbitrap Fourier Transform Mass Spectrometry

Another FT-based high resolution mass analyzer is the Orbitrap which was developed by Makarov in the 1990s and released as a commercial instrument in 2005⁷⁸⁻⁸⁰. Similar to FT-ICR MS, image current detection and ion trapping are used with ion packets pulsed into the Orbitrap through a C-trap which removes ion packets with wide axial distributions (Figure 1-15)⁸¹. In contrast to the ion motion within an ICR cell, ions inside an Orbitrap undergo rotational motion, radial motion, and axial oscillation. The frequency of axial oscillation, ω , is described as:

Equation 1-2

$$\omega = \sqrt{\frac{q}{(m/z)}} k$$

where q is the elementary charge (1.602×10^{-19} C), and k is the field curvature which depends on the shape and geometry of the Orbitrap electrodes⁸².

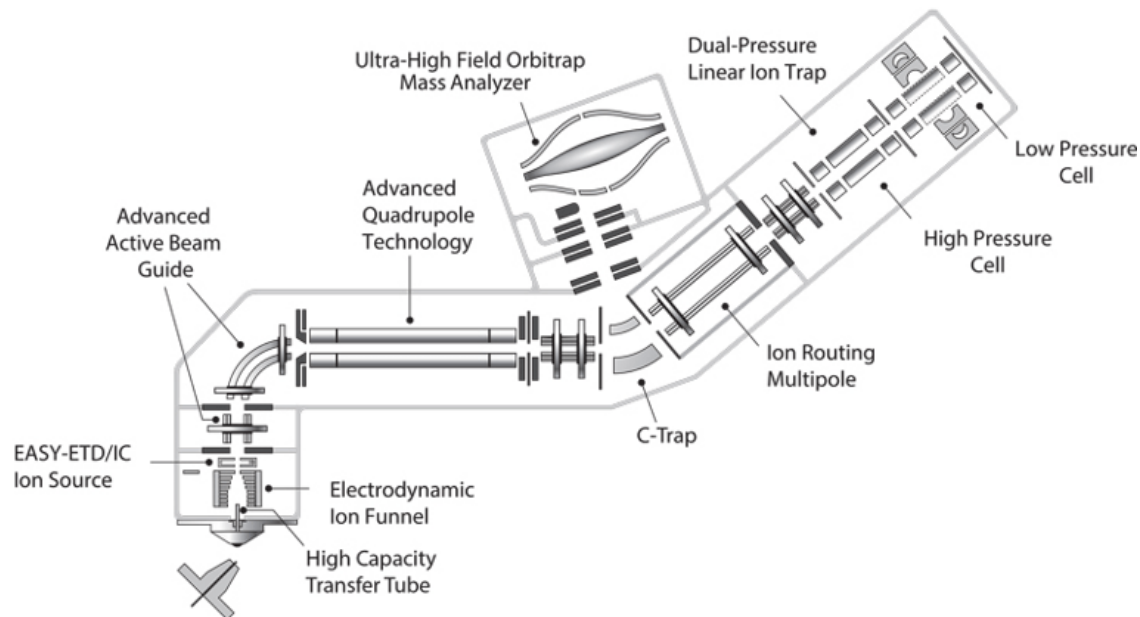


Figure 1-15 Instrument schematic of an Orbitrap Fusion Lumos mass spectrometer (Thermo Scientific).

1.5 Tandem Mass Spectrometry (MS/MS)

To obtain additional structural information from MS analysis, gas-phase bond cleavages can be performed to generate structurally informative fragment ions. First, a precursor ion is selected, e.g., by the first quadrupole on a QqQ, then energy is applied to activate the precursor ion to induce fragmentation. In the case of proteins and peptides, Biemann nomenclature is used for backbone fragmentation, specifically *a*, *b*, and *c* are used to designate fragments from the N-terminus while *x*, *y*, and *z* are used for C-terminus containing fragments (Figure 1-16)⁸³.

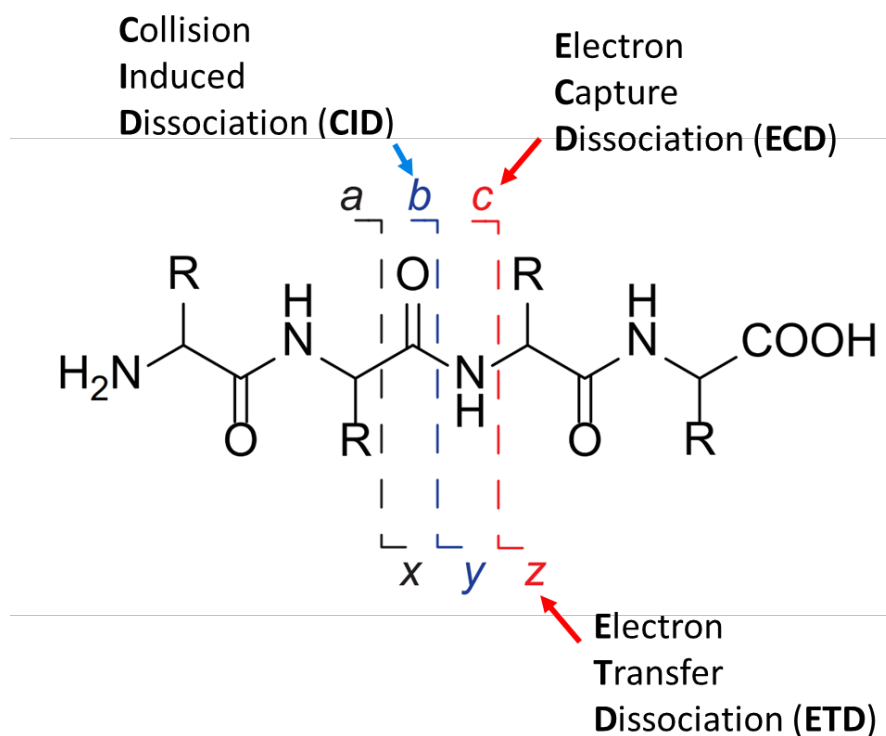


Figure 1-16 Nomenclature of peptide fragment ions in MS/MS and corresponding tandem technique.

1.5.1 Collision Induced Dissociation (CID)

The most common fragmentation method is collision induced dissociation (CID) in which selected precursor ions collide with neutral gas molecules, e.g., nitrogen or argon, to increase their internal energy leading to fragmentation⁸⁴. The amount of translational energy transferred to the precursor ion can be described using the following equation:

Equation 1-3

$$E_{com} = \left(\frac{N}{m_p + N} \right) E_{lab}$$

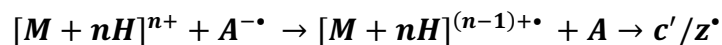
E_{lab} is the ion's kinetic energy, E_{com} is the internal energy increase, N is the neutral gas mass, and m_p is the precursor ion mass. CID is considered a "slow heating" method due to fragmentation

occurring on the microsecond to millisecond timescale⁸⁵. One variant of CID is beam type-CID, also referred to by the tradename higher energy collision dissociation (HCD), on Orbitrap type instruments as used in Chapter 4. CID cleaves the backbone amide bond within peptides, generating *b*- and *y*-type ions.

1.5.2 Electron Transfer Dissociation (ETD)

Introduced by Syka and coworkers in 2004, electron transfer dissociation (ETD) utilizes radical anions, e.g., fluoranthene, to transfer electrons to multiply charged positive ions in an ion trap type mass spectrometer⁸⁶:

Equation 1-4



The ' in equation 1-3 denotes hydrogen atom transfer and \bullet indicates a radical site. Fragmentation efficiency is dependent on precursor ion *m/z*, with poor fragmentation efficiency observed for low charge state precursor ions⁸⁷⁻⁹⁰. Less energy is available for fragmentation of doubly protonated precursor ions (the minimum charge state compatible with ETD) compared with triply and higher charge state precursor ions^{89,91-93}. In addition, doubly charged precursor ions may have more compact gas-phase structures containing intramolecular hydrogen bonds or salt bridges, which can prevent complementary product ions from separating and being detected. In contrast to CID from which *b*- and *y*-type ions are generated upon fragmentation, ETD and its predecessor electron capture dissociation (ECD, which uses free electrons rather than a radical anion reagent) generate *c*- and *z*-type ions (Figure 1-16)⁹⁴.

1.6 Hydrogen/Deuterium Exchange (HDX)

Hydrogen exchange as a probe for protein dynamics in solution was pioneered in the 1950s by Linderstrøm-Lang and coworkers⁹⁵. Since then, exchange measurement has evolved from liquid scintillation counting of tritium to mass spectrometry of deuterium incorporation^{96,97}. Compared to other protein structural characterization techniques, including nuclear magnetic resonance (NMR) spectroscopy and X-ray crystallography, hydrogen deuterium exchange mass spectrometry (HDX-MS) provides distinct advantages in that lower sample amounts of larger sized proteins can be investigated in solution with less stringent purity requirements, albeit at lower structural resolution⁹⁸⁻¹⁰⁰. The general workflow for a bottom-up HDX-experiment is outlined in Figure 1-17. The digestion step typically utilizes pepsin as the proteolytic enzyme as it must occur at low pH to avoid deuterium back exchange.

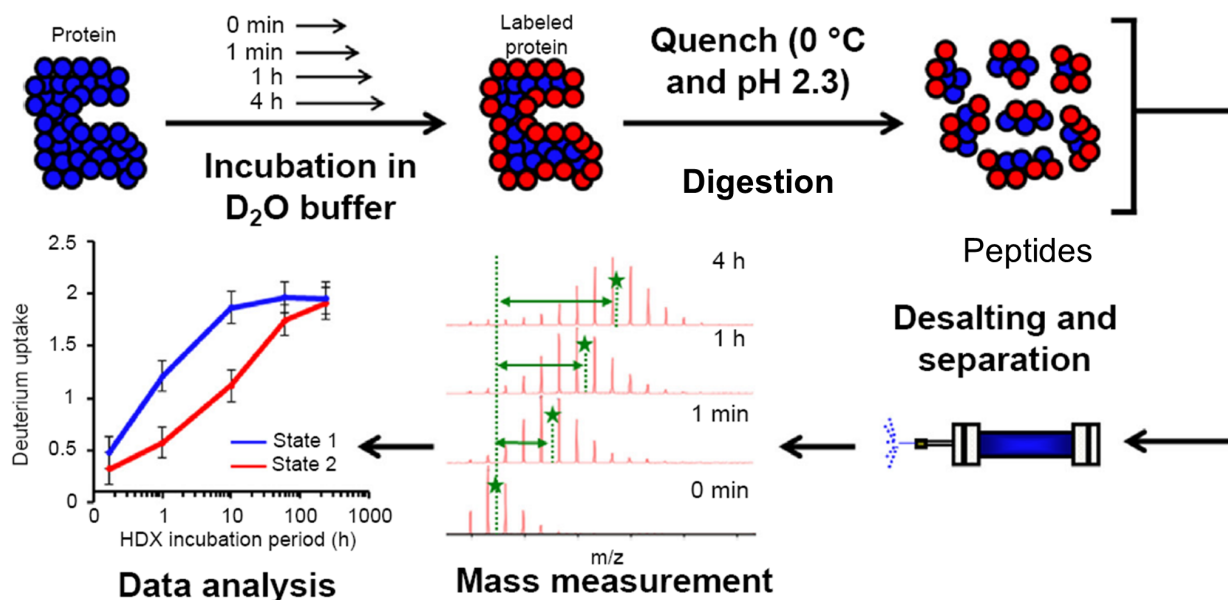


Figure 1-17 General workflow for bottom-up HDX-MS. A protein is incubated in D₂O for varying amounts of time before the labeling is quenched by reducing temperature and pH. The labeled protein is then proteolyzed with the resulting peptides desalted during a rapid separation. Each deuterium incorporated into the peptide results in a 1 Da mass shift to the

right in the MS spectra. Comparing the plots of deuterium uptake for different conditions can provide conformational dynamics information¹⁰¹.

While peptide-level deuterium incorporation under different conditions provides valuable information on protein conformational changes, it is desirable to increase structural resolution by monitoring deuterium incorporation at the single amino acid level^{102,103}. To accomplish such resolution, MS/MS techniques are required, specifically electron-based fragmentation methods to avoid scrambling and preserve localized deuterium information upon peptide backbone cleavage^{104,105}. When scrambling occurs, the reversible exchange of amide hydrogens for deuterium is randomized across the peptide and structural resolution is lost (Figure 1-18). Extensive scrambling occurs in the slow heating activation method CID whereas both ETD and ECD have been shown to proceed without scrambling^{102,106-108}. However, the high charge state requirement of the latter techniques is problematic for peptic peptides that tend to be shorter with lower charge.

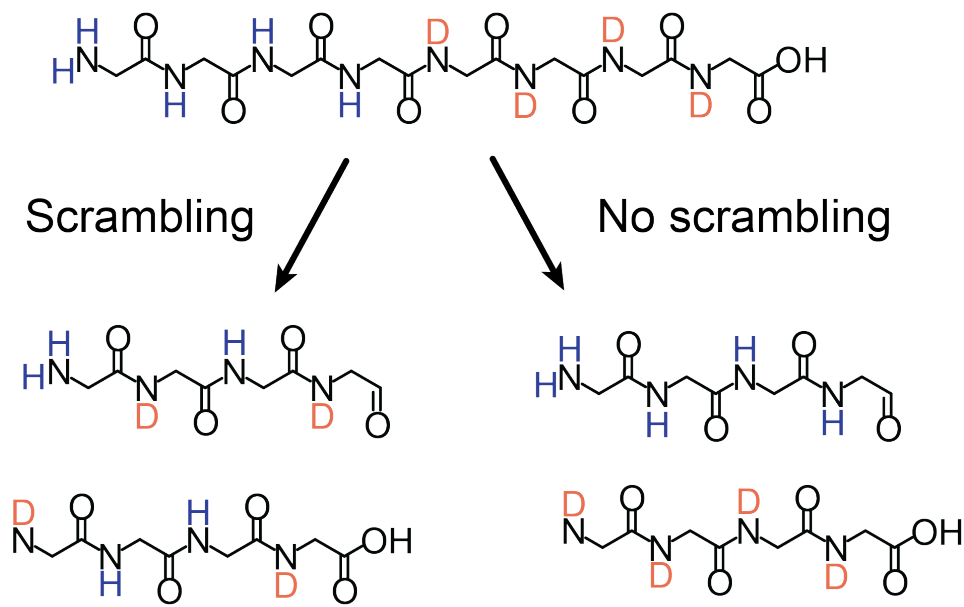


Figure 1-18 Principle of selectively labeled model peptide gas phase H/D scrambling as a result of fragmentation. When scrambling occurs, localized deuterium content is lost.

1.7 Dissertation Overview

This dissertation focuses on developing MS workflows for improved screening and characterization in drug development. These workflows span from small molecules/potential payload and cleavage linkers to peptides resulting from an antibody digest using both targeted and untargeted approaches.

In Chapter 2, whole cell droplet-MS is applied to improve screening throughput in a directed evolution campaign for the saxitoxin biosynthetic enzyme SxtA, capable of transforming α -amino acid substrates to α -amino ketones in a single step, towards accepting the non-native substrate tryptophan. This workflow development involved sample preparation optimization and in-spray dilution via a triple tube coaxial sheath flow sprayer with greatly increased throughput enabled by eliminating the need for chromatography prior to MS analysis.

Chapter 3 covers a structure-activity relationship (SAR) study of cathepsin-mediated release of amine substrates conjugated to peptide linkers. While there has been significant development in optimizing peptide linkers, to date, no systematic investigation of spacer/payload dependent release rates has been reported. Aliphatic, aromatic, and benzylic amines were studied, linked to a small variety of peptide sequences without a self-immolative spacer.

In Chapter 4, peptic digests of antibodies were supercharged post separation to increase CID-based peptide identification as well as improve ETD efficiency by generating higher charge state precursor ions for HDX workflows. A summary of all results and future directions is covered in Chapter 5. Chapters 2 through 4 are written in multiple manuscript format.

Chapter 2: Droplet Microfluidics-Mass Spectrometry for Whole Cell High Throughput Screening of Saxitoxin Biosynthetic Enzyme Directed Evolution Towards Non-Native Substrates in Chemoenzymatic Synthesis

2.1 Introduction

As an alternative to labor-intensive total synthesis, efforts to leverage nature's approach to the biosynthesis of complex molecules such as natural products in chemoenzymatic synthesis strategies that exploit the ability of enzymes to catalyze synthetically challenging transformations with great specificity and efficiency are gaining traction¹⁰⁹⁻¹¹². Recent insights into the chemistry of the polyketide-like synthase, saxitoxin biosynthetic module A (SxtA) from the cyanobacterium *Cylindrospermopsis raciborskii* T3, identified four domains within this megasynthase that generate a linear biosynthetic precursor to the potent shellfish neurotoxin saxitoxin (STX)¹¹³. Of these four domains, the terminal 8-amino-7-oxononanoate synthase (AONS) domain has potential as a biocatalyst converting α -amino acids to α -aminoketones in a single step involving acyl carrier protein (ACP) domain-bound ketone substrate¹¹⁴ (Figure 2-1). By contrast, synthetically converting the SxtA native substrate arginine to its ketone product requires six steps and protecting groups¹¹⁵. Initial characterization of the *C. raciborskii* T3 ACP-AONS didomain substrate scope as well as those of other cyanobacterial homologues, showed likely activity with seven non-native amino acids, including tryptophan¹¹⁶. The catalytic efficiency and synthetic scope can be potentially further increased through directed evolution of the enzyme¹¹⁷⁻¹²⁰.

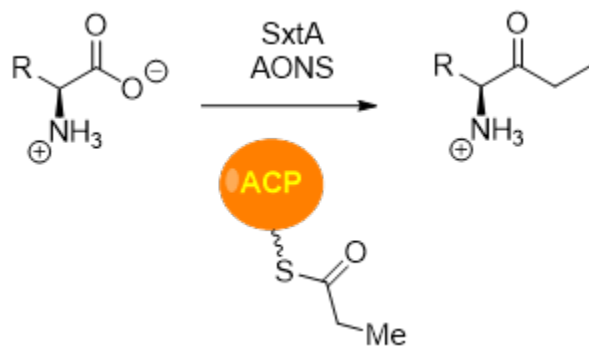


Figure 2-1 General reaction scheme of SxtA AONS domain converting an α -amino acid to an α -aminoketone using ACP domain-bound ketone substrate.

Directed evolution techniques generate numerous enzyme sequence variants to be screened for the desired activity. Liquid chromatography/mass spectrometry (LC/MS) methods allow simultaneous detection of substrate and product from cell lysates without need for labeling; however, the time-scale of such experiments is not compatible with high throughput screening. Kennedy and co-workers have previously demonstrated label free high throughput screening of enzyme activity (inhibition) via direct infusion electrospray ionization (ESI)-MS of droplets containing purified enzyme and substrate^{46,121}. In addition, Kennedy and co-workers in collaboration with Merck scientists applied similar technology towards the screening of the yield of a known reaction for 84 transaminase variants, generated by directed evolution, directly from clarified lysate⁵². Here, we demonstrate such whole cell droplet microfluidics-ESI-MS screening of SxtA ACP-AONS didomain variant activity for direct generation of the ethylketone from the non-native substrate tryptophan (Figure 2-2).

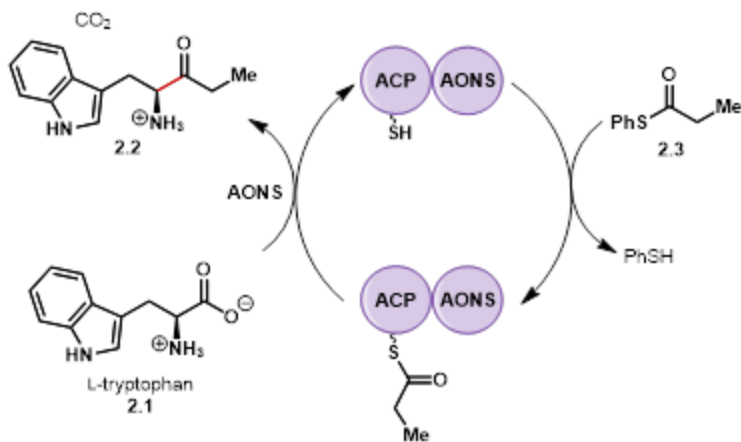


Figure 2-2 Biocatalytic platform for synthesis of tryptophan ethyl ketone 2.2. The AONS domain catalyzes decarboxylative condensation of the amino acid 2.1 with ACP domain-bound ethyl ketone loaded from thiophenyl (PhS)-ethyl ketone substrate 2.3.

2.2 Experimental Methods

2.2.1 Chemicals and Reagents

All reagents and solvents were purchased from Sigma-Aldrich (St. Louis, MO) unless stated otherwise.

2.2.2 Whole-cell library reactions with *M. wollei* ACP-AONS-didomain variants

Directed evolution and preparation of purified substrate and product standards was performed by Stephanie Chun in collaboration with the Narayan Lab. Cell pellets in 96-well plates were resuspended in reaction solution containing 1 mM thiophenyl ethyl ketone **2.3**, 8 mM tryptophan **2.1**, 50 mM HEPES pH 7.0 and 150 mM NaCl (final volume 250 μ L per well). Plates were covered and incubated at 30 $^{\circ}$ C, 250 rpm for 18 h. Reactions were quenched by diluting 2-fold with MeOH containing 0.5% v/v formic acid. Precipitate from quenched reactions was

pelleted at 2,000 x g for 10 min. From each well 200 μ L of supernatant was sterile filtered through a 0.2 μ m 96-well plate filter prior to droplet generation.

2.2.3 Droplet Generation from Multi-well Plate (MWP)

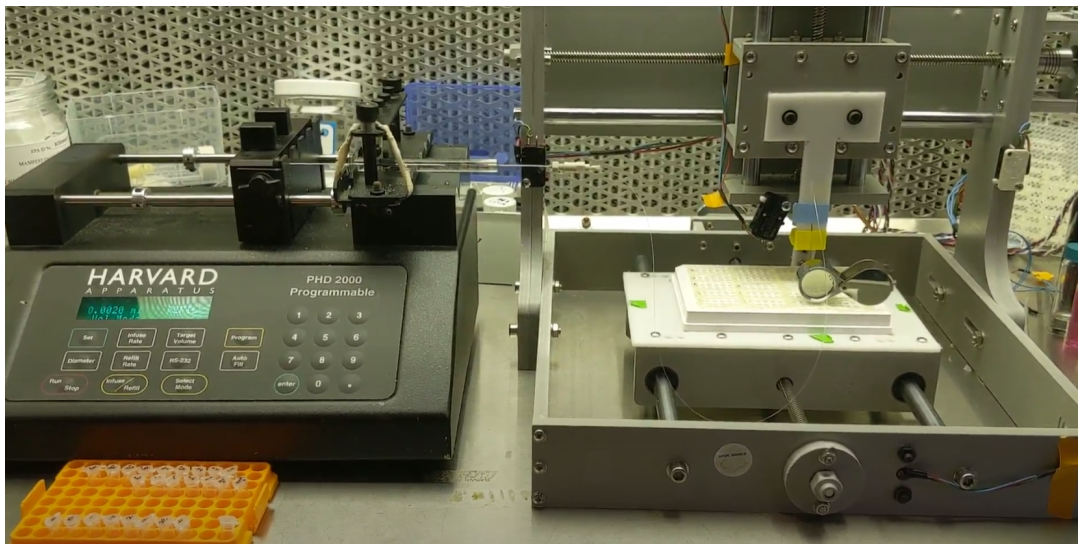


Figure 2-3 Image of droplet generation from MWP setup. Syringe pump shown on left and XYZ-positioner with epoxied MWP shown on right.

The edges of the droplet making MWP were built-up to 3 mm height using epoxy to allow oil to be overlaid onto the samples (Figure 2-3, right). Samples were pulled into a 150 μ m i.d., 360 μ m o.d. Teflon tube (IDEX Health and Science, Oak Harbor, WA) connected to a Hamilton 25 μ L gastight syringe (Reno, NV), mounted on a PHD 2000 programmable syringe pump (Harvard Apparatus, Holliston, TX; Figure 2-3, left). Both the syringe and Teflon tube were prefilled with degassed perfluorodecalin (PFD; 95% purity, Acros Organics, NJ) prior to droplet generation. A computer-controlled XYZ-positioner (built in-house from XSlide assemblies, Velmex Inc., Bloomfield, NY; Figure 2-3, right) was used to move the inlet of the Teflon tube from sample to sample while the syringe was withdrawing at 1.2 μ L/min. Quenched reaction droplets with 45 nL volume were segmented by 50 nL oil to generate a droplet train with each reaction mixture

analyzed in triplicate. Each train began with five calibration droplets containing simulated 1 % conversion samples (see section 2.2.4) in cell lysate followed by five blank reaction buffer droplets before sample droplets. Droplet volume was determined visually using a micro ruler with known increments to measure length (Figure 2-4). This value was then used as a in the following equation where a is capsule height and r is the radius:

Equation 2-1

$$V = \pi r^2 \left(\frac{4}{3} r + a \right)$$

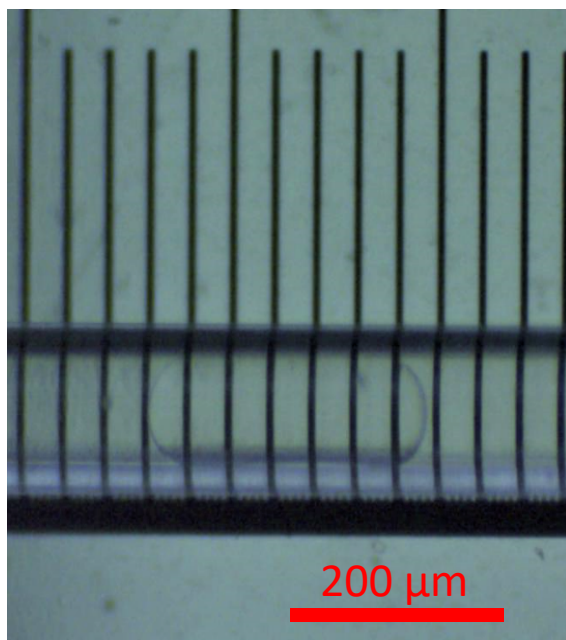


Figure 2-4 Microscope image of generated droplet with micro ruler in background to determine droplet volume.

2.2.4 Simulated Conversion Standards

To quantify the amount of product formed from each enzyme variant, simulated conversion samples were added to each droplet train. These simulated conversion samples were prepared by spiking in tryptophan and ethylketone product into cell lysate stock to match actual reaction samples most closely. The limiting substrate for the reaction was the thiophenyl ethyl ketone **2.3**,

i.e., for 10% conversion of 1 mM **2.3**, there would be 0.9 mM **2.3**, 7.1 mM tryptophan, and 0.1 mM product in the cell lysate. These solutions were prepared in 50:50 MeOH/water with 0.5% FA. Prior to running actual reaction mixtures, a range of simulated conversion standards were prepared and analyzed to determine the dynamic range of our assay.

2.2.5 MS Analysis

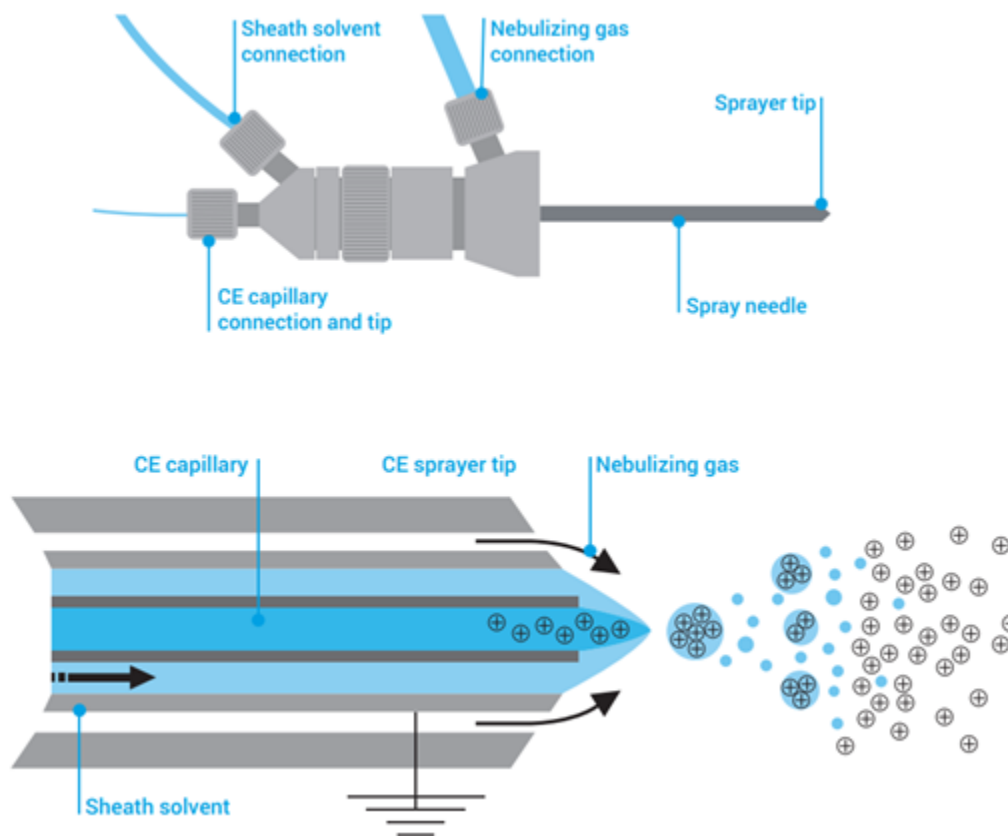


Figure 2-5 Triple-tube coaxial sheath flow sprayer used for droplet-MS.

Teflon tubing containing droplets was threaded through a capillary electrophoresis (CE)-ESI Source equipped with coaxial sheath-flow (Agilent Technologies, Santa Clara, CA) (Figure 2-5). Sheath and droplet flows were generated by Fusion 400 syringe pumps (Chemyx, Stafford, TX) at 25 $\mu\text{L}/\text{min}$ and 5 $\mu\text{L}/\text{min}$, respectively. Sheath buffer contained 50:50 MeOH/water with

0.5% FA. ESI-MS analysis was performed on an Agilent 6410 triple quadrupole mass spectrometer (Agilent Technologies, Santa Clara, CA) operated in single reaction monitoring (SRM) mode using the parameters in Table 2-1. ESI potential was set to 2500 V, nebulizer gas to 12 psi, and drying gas to 10 L/min at 275 °C.

Table 2-1 SRM Parameters for whole-cell reaction monitoring by droplet-MS

Analyte	m/z transition	Dwell time (ms)	Fragmentor (V)	Collision energy (v)
Tryptophan (2.1)	205 → 146	150	135	15
Ketone Product (2.2)	217 → 130	150	120	15

2.3 Results and Discussion

2.3.1 Droplet Generation and Assay Optimization

Initial method development used purified standards in a reaction buffer containing 50 mM HEPES, 150 mM NaCl, 100 μM pyridoxal phosphate (PLP). When screening simulated reaction samples containing cell lysate, as expected, a significant decrease in signal intensity was observed due to a strong matrix effect. Comparing the same concentrations of analyte present in reaction buffer with and without cell lysate indicate a 40% reduction in signal in the presence of cell lysate (Figure 2-6).

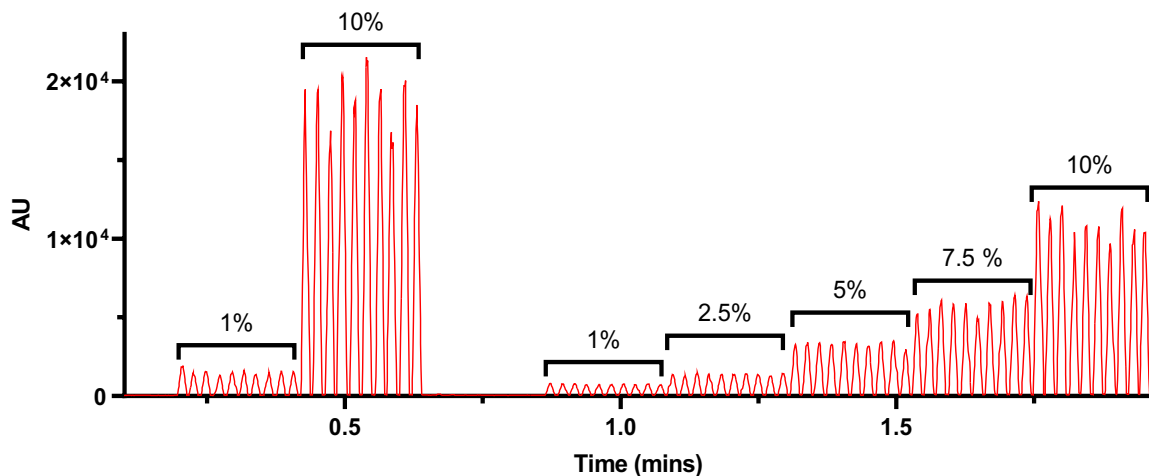


Figure 2-6 Droplet trace of tryptophan ethyl ketone product standard with simulated 1% and 10% substrate conversion in reaction buffer (left) and simulated 1%, 2.5%, 5%, 7.5%, and 10% substrate conversion spiked into cell lysate (right).

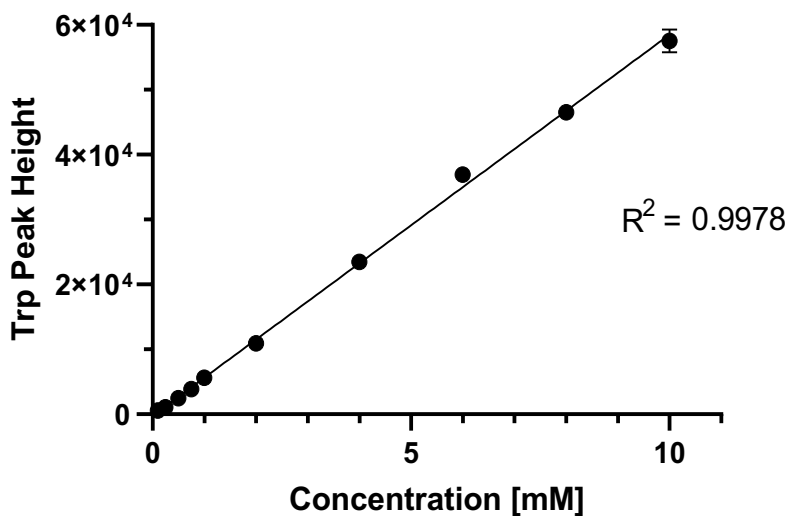


Figure 2-7 Calibration curve of Trp in reaction buffer containing cell lysate. Each data point is an average of five replicates. Error bars are not visible as they are smaller than the data points.

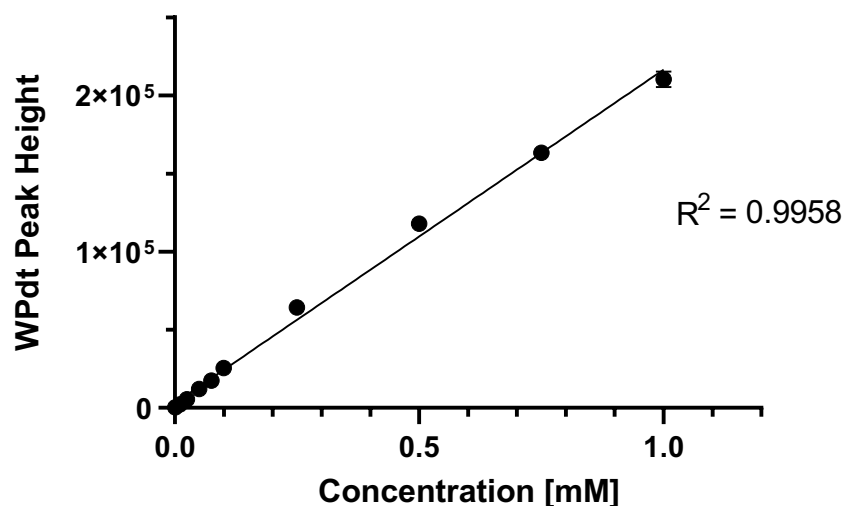


Figure 2-8 Calibration curve of tryptophan ethyl ketone product in reaction buffer containing cell lysate. Each data point is an average of five replicates. Error bars are not visible as they are smaller than the data points.

The matrix effect did not impact linearity when generating calibration curves for Trp and its ethyl ketone product using droplet-MS. For Trp, a calibration curve spanning from 0 to 10 mM (maximum amount present during reactions is 8 mM) had an R^2 of 0.9978 (Figure 2-7) while the ethyl ketone product in the range from 0 to 1 mM (the latter corresponding to 100% conversion) had an R^2 of 0.9958 (Figure 2-8). Data were collected in replicates of five and peak height was used rather than peak area as peak widths were not consistent due to droplet merging.

The manufacturer of the sheath flow sprayer recommended a total flow rate greater than 25 $\mu\text{L}/\text{min}$ for stable electrospray. Using this as a guideline for droplet work, droplets were infused at 5 $\mu\text{L}/\text{min}$ and the sheath flow was set to 25 $\mu\text{L}/\text{min}$ allowing for in spray dilution, which in principle reduces ionization suppression from matrix effects. The lack of carryover detected in blank buffer droplets following analyte droplets is thought to be due to the relatively higher rate of the sheath flow compared to the droplet flow rate. Using a droplet volume of 45 nL followed

by 50 nL of oil generated uniform peaks resulting in no observable carryover while allowing for sufficient sampling across the peaks. Utilizing these parameters allowed for reliable detection and quantification of the analytes of interest in droplets. RSD for the Trp ethyl ketone peak height at 1% simulated conversion was determined to be 7% while RSD for 10% conversion was calculated to be 4% (Figure 2-9).

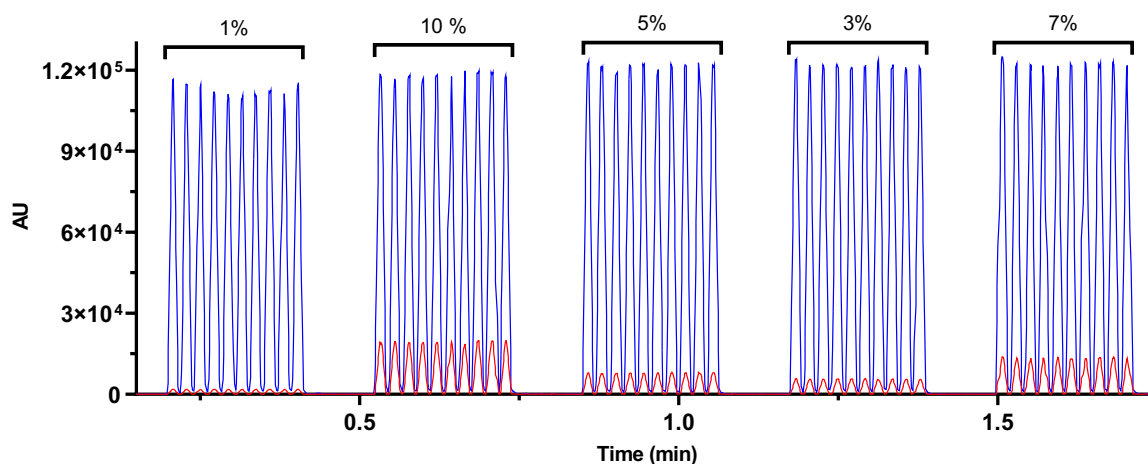


Figure 2-9 Droplet traces of Trp ethyl ketone product for 1, 10, 5, 3, and 7% simulated conversion (in red) and Trp substrate (in blue). Sample droplet packets are separated by five blank droplets containing only reaction buffer.

Prior to implementing droplet-MS, cells were lysed via sonication (3 s on, 3s off, 3 min total) and kept in aqueous buffers for LC-MS analysis. Conversely, aqueous samples were diluted with an organic solvent to improve desolvation for droplet-MS. Since MeOH is known to lyse cells and facilitate access to intracellular components, sonication was replaced by diluting samples 2x with MeOH thereby allowing direct droplet generation of these samples^{122,123}.

2.3.2 MS Optimization

Identification of optimum tandem mass spectrometry (MS/MS) precursor to product ion transitions to reliably and rapidly monitor product formation at high sensitivity is key to using droplet-MS, especially for the targeted complex matrix containing cellular components as well as various salts. The full MS1 scans of the tryptophan substrate and ethyl ketone product are shown in **Error! Reference source not found.** (top) Figure 2-11 (top), respectively.

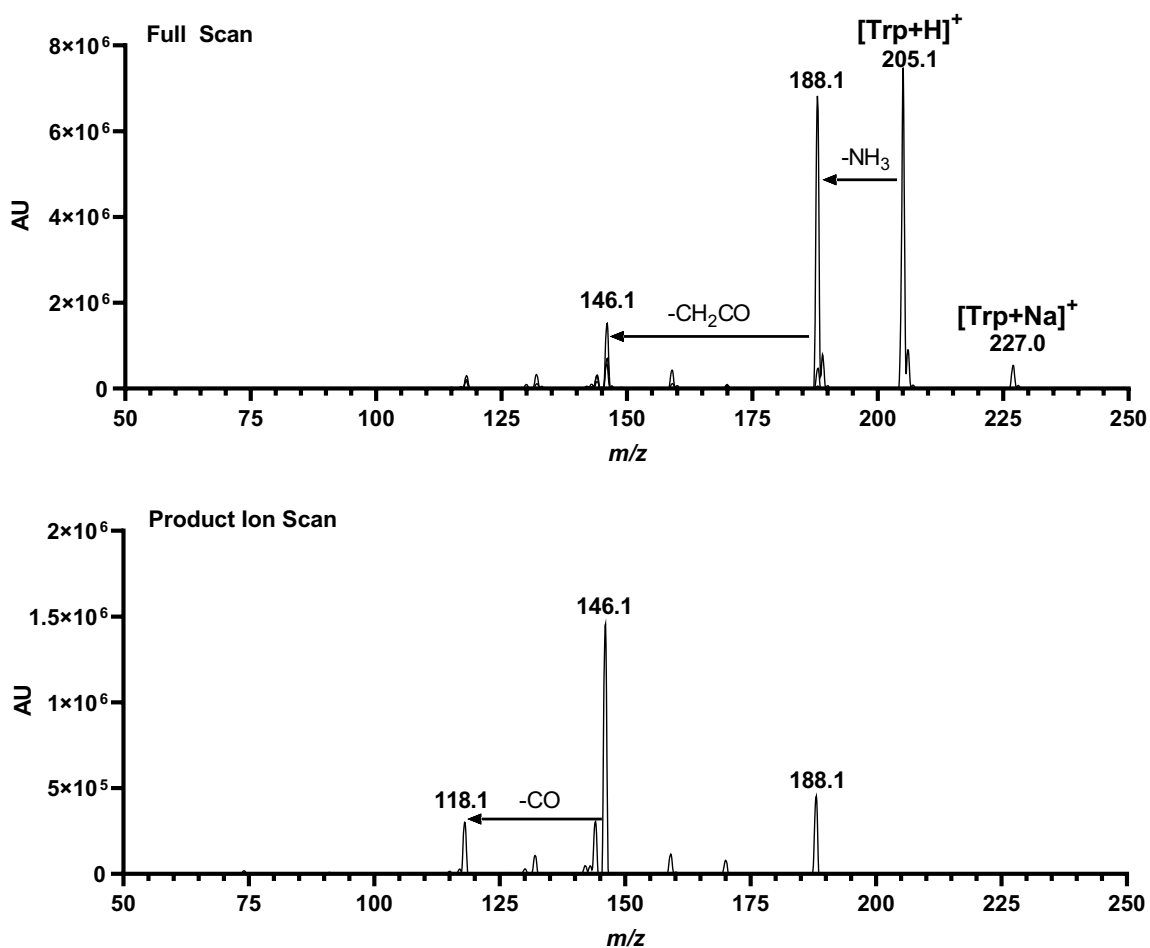


Figure 2-10 Figure 2 10 MS (top) and MS/MS (bottom) spectra of protonated tryptophan.

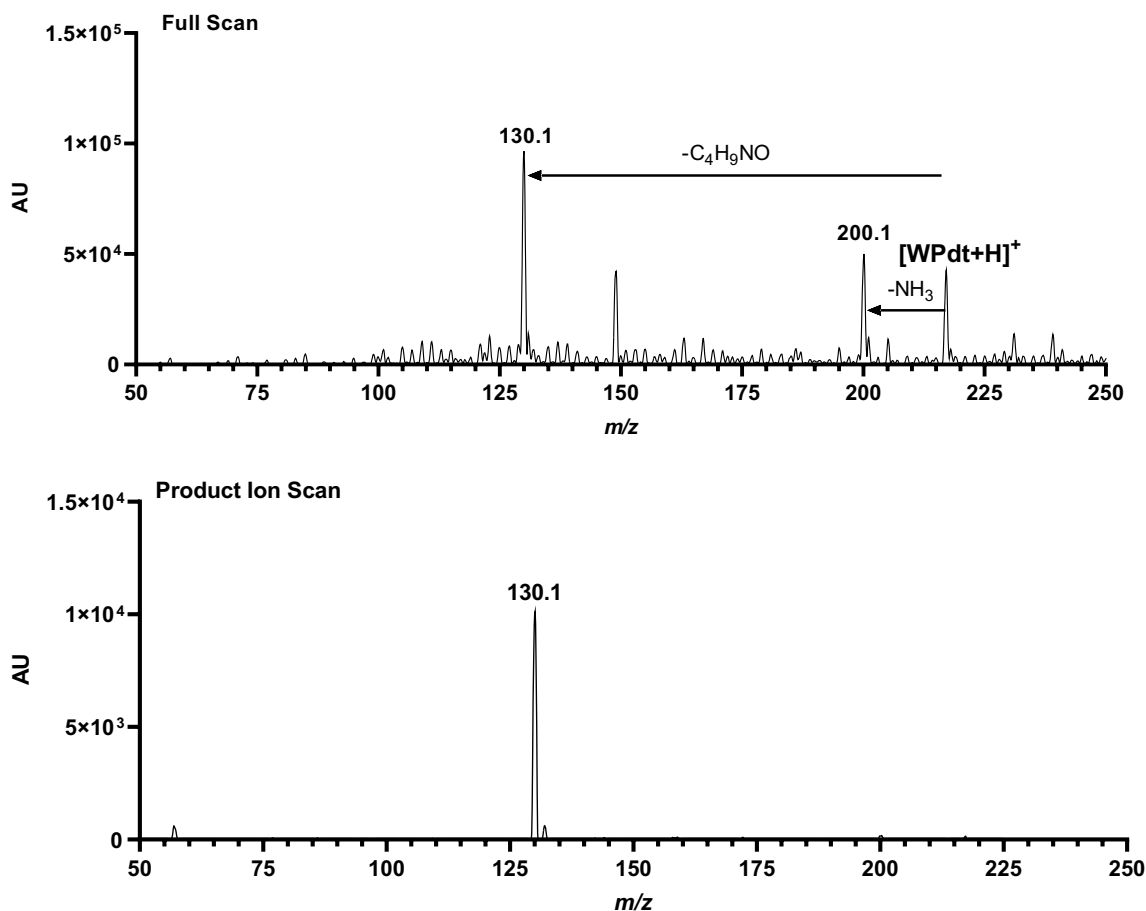


Figure 2-11 MS (top) and MS/MS (bottom) spectra of protonated tryptophan ethyl ketone product (WPdt).

For Trp, the most abundant ion observed is the protonated intact species with an accompanying relatively low abundance sodium-adducted species. Significant in-source fragmentation is also observed, including deamination and formation of a product ion at m/z 146, previously proposed to form via the dissociation pathway shown in Figure 2-12 (top). The ethyl ketone product was even more susceptible to in-source fragmentation with a product ion at m/z 130, corresponding to the tryptophan side-chain (Figure 2-12 (bottom)), being the most abundant species. Upon CID MS/MS, the aforementioned product ion at m/z 146 was most abundant for the tryptophan substrate and thus selected as the SRM target ion (Table 2-1). For the ethyl ketone product, only the charged tryptophan side chain fragment at m/z 130 was observed upon CID, thus

being chosen as the SRM target ion. While this fragment may be formed from the tryptophan substrate as well¹²⁴, we did not observe it under our MS/MS conditions and, further, this possibility is not a concern for quantitation as the precursor ion mass is different.

Once the precursor and fragment masses were selected, several parameters were optimized, including: fragmentor voltage, collision energy voltage, and dwell time. Conditions listed in Table 2-1 generated the highest S/N ratio for the monitored fragment ions and were thus selected for screening. Due to the lack of basic sites within the thiophenyl substrate **2.3**, its ionization efficiency was poor, and no signal was observed. However, we elected to determine enzyme activity solely based on the increase of ethyl ketone product signal rather than decreases in the substrates **2.1** and **2.3**.

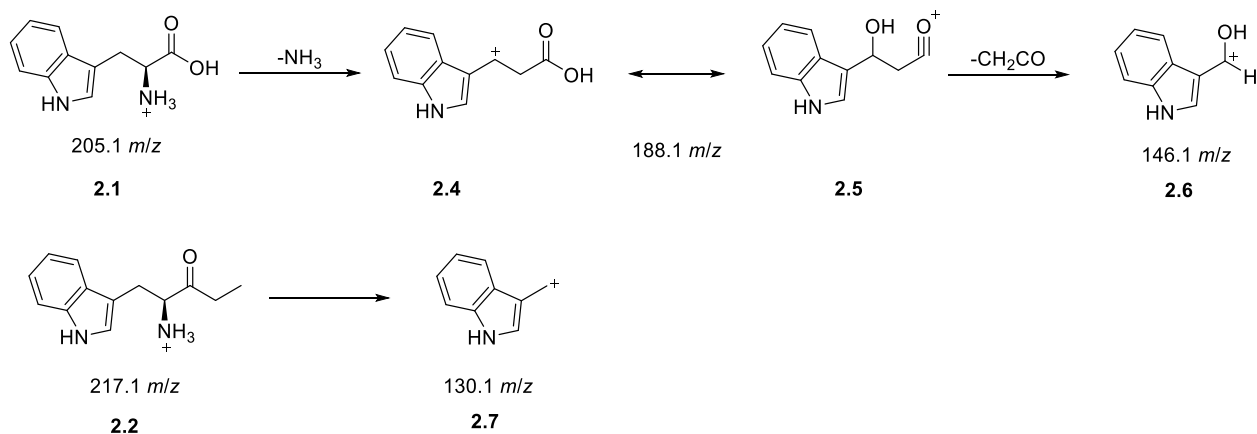


Figure 2-12 Fragmentation pathways for tryptophan (top) and its ethyl ketone product (bottom)^{124,125}.

2.3.3 Screening results

Typically, in directed evolution campaigns, the first couple rounds of evolution only yield enzyme variants with moderate to low activity towards non-native substrates. When screening actual reaction samples, simulated 1% conversion in cell lysate droplets were generated at the end

of each droplet train to serve as a one-point calibration for quantifying the turnover in subsequent samples. Monitoring both tryptophan substrate and ethyl ketone product signals in actual reaction samples, as expected, showed very low turnover for the desired product (Figure 2-13). However, three wells (Figure 2-14) with potentially increased product formation activity, ranging from 0.25 – 0.5 % conversion still indicate an improvement over the wildtype enzyme which was validated using LC-MS/MS; however, the results of this validation should be revalidated using an optimized MS method due to insufficient sampling across the product peak. Sanger sequencing of these hits showed mutations at seemingly random locations in the AONS domain far from the active site (F979L and I1076T using whole module numbering). Nevertheless, the developed droplet-MS high throughput screening method was able to screen 784 enzyme variants in triplicate in under seven hours and allowed direct detection of substrate and product from whole cell samples with minimum sample preparation. These preliminary results show promise for rapid screening of additional rounds of evolution and additional non-native substrates.

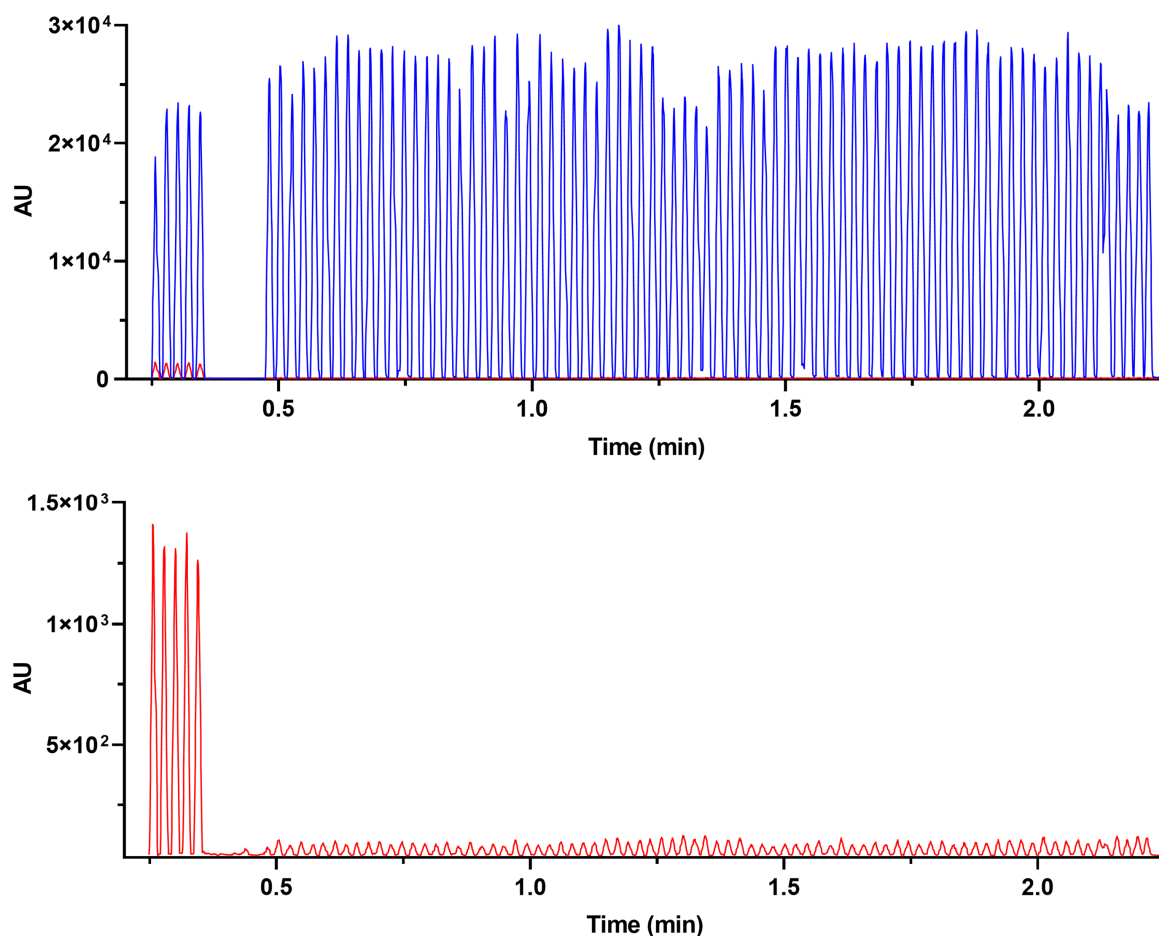


Figure 2-13 Droplet trace of tryptophan (blue) and tryptophan ethyl ketone product (red) with simulated 1% conversion sample on the left followed by sample droplets from row E of plate 1. Samples analyzed in replicates of five.

2.4 Conclusions

A droplet-MS workflow to screen whole-cell reactions for SxtA ACP-AONS didomain directed evolution towards tryptophan as a non-native substrate was developed, which increased screening throughput from 4 samples/h to 362 samples/h. Throughput could be further improved by reducing droplet volume, thus reducing droplet generation time which was the rate limiting step. The developed method eliminated the need for liquid chromatography prior to MS analysis,

in addition to consolidating reaction workup steps to reduce sample preparation and reagent consumption. Further work to apply nanoflow ESI may improve sensitivity, thus allowing for detection of lower quantities of product. Another direction for future work would be the introduction of a system for continuous droplet generation and infusion. By simultaneously infusing and generating droplets screening efficiency can be improved by allowing for longer durations of autonomous operation.

Chapter 3: Structure-Activity Relationships for Cathepsin-Mediated Release of Model Amine-Containing Payloads from Cleavable Linker Conjugates

3.1 Introduction

Proteolytic enzymes perform fundamental biological roles due to their capabilities to hydrolyze amide bonds in proteins and peptides¹²⁶⁻¹²⁸. Of the hundreds of human proteases, cysteine cathepsins are a family of lysosomal endopeptidases (cathepsin F, K, L, S, V, B, H) and exopeptidases (cathepsins B, X, H, C) that are often upregulated in multiple cancer types¹²⁷. Within this family, cathepsin B (CatB) is the most studied due to its overexpression in various cancers and its contributions to oncogenesis and metastasis^{129,130}. Tissue-specific expression patterns and distinct reactive-site properties have rendered the incorporation of cathepsin cleavable linkers in antibody drug conjugates (ADCs) of interest in preclinical and clinical studies. Cathepsins share a papain-like structure comprised of two domains intersecting at a V-shaped cleft¹³¹. Using Schechter and Berger nomenclature to designate residues in relation to the scissile peptide bond, substrate amino acid residues are denoted as P or P' with corresponding enzyme substrate binding pockets denoted as S or S' (Figure 3-1).

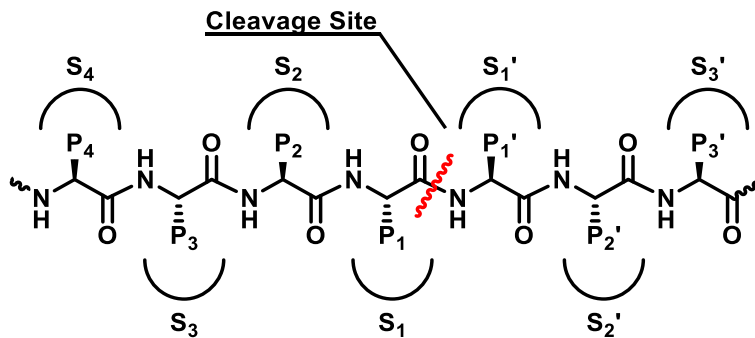


Figure 3-1 Schechter and Berger nomenclature. P designates the substrate residues while S denotes the enzyme's active site¹³².

The core of the active site cleft features a crucial cysteine-histidine ion pair, which acts as the nucleophile for amide bond hydrolysis (Figure 3-2). Cathepsin and protease specificity in general, rely on enzyme recognition of certain amino acid residues within the active site. While the cathepsin active site is known to accommodate up to ten amino acids¹²⁷, experimental evidence points to a maximum of four residues on each side of the scissile peptide bond¹³³.

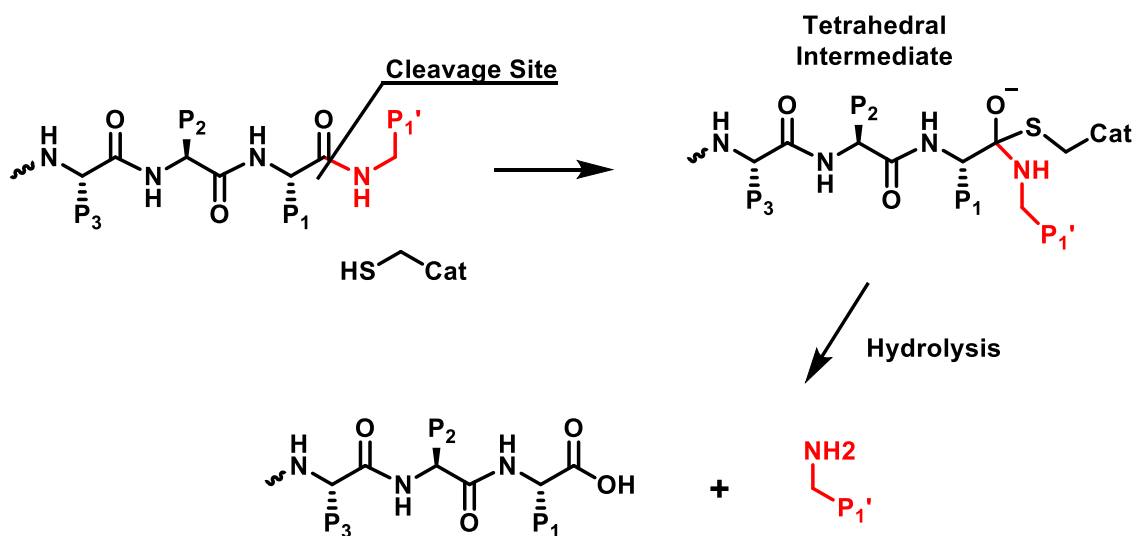


Figure 3-2 Reaction mechanism for (CatB)-mediated cleavage of linker substrates. Cathepsin B cleaves the amide bond between the linker and payload (red).

Optimization of the drug molecule toward enzyme-specific release is one approach to improve ADC selectivity. However, this approach is challenged by the limited understanding of the structure-activity relationship (SAR) of the cathepsin-mediated cleavage of different payload amines. Indeed, while there have been multiple in-depth reports on linker optimization of the P1 and P2 amino acids for payload release, to the best of the author's knowledge such studies on the released substrate have not been previously reported¹³⁴. Herein, we report a systematic investigation into the release rates of a variety of model amine-containing payloads from peptide linkers using a CatB assay and high-resolution liquid chromatography-mass spectrometry (LC-MS) analysis with a quadrupole-time-of-flight (Q-TOF) instrument. In addition, the use of mass spectrometry allowed for direct quantification of released payload. This SAR study is first investigation on how chemical motifs on the payload impact release rates from peptide linkers for a variety of future applications in ADC and other therapeutic designs.

3.2 Experimental Methods

3.2.1 Chemicals and Reagents

All chemicals and reagents were purchased from Sigma-Aldrich (St. Louis, MO) unless stated otherwise. Cathepsins B and L (CatL) were sourced from human liver, while cathepsin S (CatS) was recombinant and expressed in *E. Coli*. Optima UHPLC-MS grade mobile phases [0.1% formic acid in water] and [0.1% formic acid in acetonitrile (ACN)] were purchased from Fisher Scientific (Fair Lawn, NJ). Sterile 1 M sodium citrate pH 5.0 was purchased from Teknova Inc. (Hollister, CA). Rat liver tritosomes were acquired from SEKISUI XenoTech, LLC (Kansas City, KS) and used without further purification. Assay plates and seals were sourced from Analytical Sales and Services Inc. (Flanders, NJ).

3.2.2 Enzyme Assay

A procedure for cathepsin B assay previously described using fluorescence-based detection¹³⁵ was modified to allow for mass spectrometry-based measurements to screen non-fluorescent payloads. To screen linker-payload compounds at a concentration of 10 μM , stock solutions were prepared at 10 mM in DMSO of which 500 nL was dispensed to each well in a 96-well collection plate in triplicate using an HP D300e digital dispenser. 50 μL of a reaction buffer consisting of 50 mM sodium citrate, 1 mM ethylenediaminetetraacetic acid (EDTA), 3 mM dithiothreitol (DTT), and 0.4 μM internal standard mixture (imipramine, labetalol, and diclofenac), pH 5.0, in water was freshly prepared and prewarmed to 37 $^{\circ}\text{C}$. 84 μg of cathepsin B from human liver was diluted with 50 mL of prewarmed reaction buffer to a final concentration of 3.33 $\mu\text{g}/\text{mL}$ and 500 μL of the enzyme solution was immediately added to each well. The plate was then sealed and briefly vortexed on a shaker before being placed in an incubator set to 37 $^{\circ}\text{C}$. Timepoints were collected at 0, 0.5, 1, 2, 4, and 24 hours by removing a 50 μL aliquot and quenching with 150 μL ice cold neat ACN. The quenched reaction samples were centrifuged (5 min at 10,000 rpm), the supernatants diluted 1:1 with 0.1% formic acid in water, and analyzed by LC-MS. Cathepsin L from human liver and cathepsin S, human recombinant were prepared using the same protocol as for cathepsin B. Tritosomes, hepatic lysosomes from rat liver loaded with Tyloxapol, were prepared in a reaction buffer containing 25 mM sodium citrate, 1 mM EDTA, and 0.4 μM internal standard mixture, pH 5.0, in water prewarmed to 37 $^{\circ}\text{C}$ at a concentration of 50 $\mu\text{g}/\text{mL}$. Negative control samples were prepared by collecting time points for 0 and 24 hours of linker-payload and released payload using reaction buffer with no enzyme added. These samples also served to determine 24-hour stability values.

3.2.3 LC-MS Analysis

Quantitation of linker-payload and released payload using mass spectrometry has been described elsewhere¹³⁶. Mass spectrometric measurements were performed on a Waters XevoG2-XS Q-TOF (Waters Corporation, Milford, MA) coupled to an Acquity UPLC I-Class system (Waters). The system was equipped with an Acquity UPLC HSS T3 column (2.1 x 100 mm, 1.8 μ m) (Waters) set at 40 °C. A gradient of solvent A [0.1 % formic acid in water] and solvent B [0.1% formic acid in ACN] was used to separate substrate precursor from released amine product (5-95% B over 9 min, flowrate 200 μ L/min, 10 μ L injection). The chromatographic system was coupled to the mass spectrometer via Z-spray-positive ion mode electrospray ionization (alternating lock mass infusion: LeuEnk, 556 m/z) with MS1 spectra obtained in sensitivity mode (50 – 1000 m/z) using 0.5 s scans. Source parameters were set to 150 °C, 20 °C desolvation, 3 kV capillary, 30 sampling cone, and 80 source offset. Gas flows were set to 100 L/h and 800 L/h for cone and desolvation, respectively. Mass calibration was performed at the beginning of each day using freshly prepared 50 mM sodium formate in 90:10 isopropanol:water.

Data were analyzed using Skyline¹³⁷ (version 21.2.0.369) for high-resolution precursor ion quantitation. After correcting to the internal standard signal to account for evaporation, MS1 peak areas of the substrate and released amine were used to determine absolute concentration using the buffer control samples as 10 μ M standards. Final absolute concentration values were plotted, and a non-linear regression was fitted (one phase decay, constrained plateau to 0) to determine half-life values for the substrates using GraphPad Prism (version 9.3.1). When plotting substrate and released amine concentrations over time, the combined total at any given timepoint was also plotted as an indicator of stability. Stability percentages were calculated by dividing the MS1 peak area of the 24 h sample by the 0 h and multiplying by 100 after internal standard correction.

Relative substrate cleavage scores with different peptidases were calculated by normalizing the substrates' half-life to the fastest substrate within each set. The substrate with the fastest activity was assigned a value of 100.

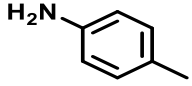
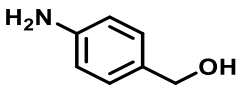
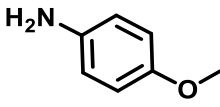
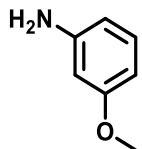
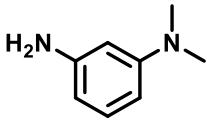
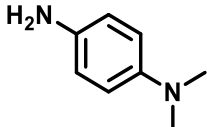
3.3 Results and Discussion

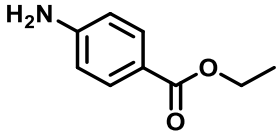
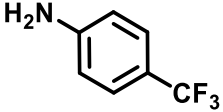
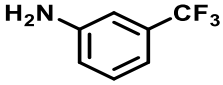
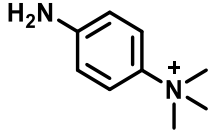
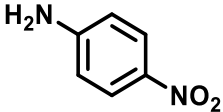
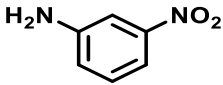
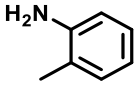
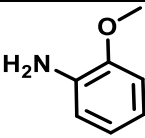
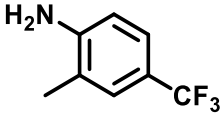
3.3.1 Cleavage of Gly-Gly-Phe-Gly Aniline Substrates

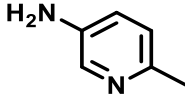
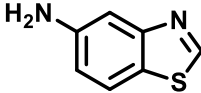
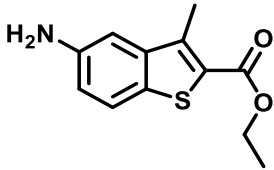
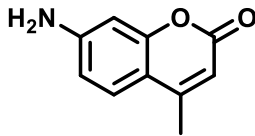
Aromatic amide designs are often used for effective release of desired drugs from peptide linkers. Therefore, initial efforts were focused on understanding SAR of cleaving aromatic amides. We designed the substrate library by conjugating a series of anilines with variable electronic and steric components to the C-terminus of the tetrapeptide GGFG. This tetrapeptide was chosen based on previous reports indicating improved serum stability compared to Val-Cit^{30,138}. Each individual peptide-anilide was incubated with activated CatB under acidic conditions (pH 5.0) at 37 °C for a maximum of 24 h. Aliquots at specific timepoints were drawn, quenched by precipitation in organic solvent, and analyzed using LC-MS. The rate of proteolytic cleavage (substrate $t_{1/2}$) was measured as a signal intensity decrease for the m/z value corresponding to the intact substrate. In addition, the appearance of signal corresponding to the released amine was monitored, to ensure that CatB preferentially cleaved the glycine-aniline bond under our assay conditions. Despite literature reports that tetrapeptides GGFG also could be cleaved by cathepsin between Phe at P2 and Gly at P1^{139,140}, we found that the released aniline was the only detectable product, and no formation of glycine adducts were observed. The results from the GGFG-anilide reactivity assay are summarized in Table 3-1. In general, the majority of tested anilides displayed relatively short $t_{1/2}$ (<1 h) under our experimental conditions and the fastest cleavage (6 min) was observed for the thiophene-2-carboxylate derivative (**substrate 18**). We were pleased to find that the GGFG-4-

methylcoumarin (GGFG-AMC) conjugate (**substrate 19**) also displayed a relatively fast release rate ($t_{1/2} = 17$ min). This observation further validated our assay since peptide-coumarin conjugates are widely used as fluorescent probes for detection of cathepsin enzymatic activity.

Table 3-1 CatB-mediated cleavage of GGFG-Anilides.

Substrate	Released Amine		$t_{1/2}$ (h) ^{a,b}	95% CI of $t_{1/2}$
1		1a	0.7	[0.6-0.8]
2		2a	1.1	[0.9-1.3]
3		3a	0.8	[0.7-0.8]
4		4a	1.1	[0.9-1.2]
5		5a	0.5	[0.4-0.6]
6		6a	0.4	[0.3-0.5]

7		7a	1.0	[0.7-1.2]
8		8a	0.3	[0.3-0.4]
9		9a	0.3	[0.2-0.3]
10		10a	2.2	[1.6-3.7]
11		11a	1.8	[1.5-2.2]
12		12a	0.8	[0.6-1.0]
13		13a	12.9	[11.1-14.8]
14		14a	2.5	[2.1-3.0]
15		15a	11.7	[7.7-13.1]

16		16a	2.0	[1.6-2.5]
17		17a	0.7	[0.6-0.8]
18		18a	0.2 0.1	[0.2-0.25] [0.08-0.1] ^c
19		19a	0.3 0.1	[0.2-0.3] [0.1-0.2] ^c

^aAll reported substrates were stable and showed cleavage only in the presence of CatB. The 24-hour stability of substrates and amine payloads were assessed by incubation under assay conditions with and without cathepsin enzyme present. ^bMeasured by HR-LCMS against an internal standard. The reported values are an average of three runs. ^cDifferent batch of enzyme was used.

No significant electronic effect on the release rate of the aniline-based payload could be established, as some anilides with neutral (**1**), electron-rich (**5**, **6**), and electron-poor (**8**, **9**) anilines showed similar release rates. We noticed that some aniline substituents such as *p*-Me₃N⁺(**10**), *p*-NO₂ (**11**), and 3-pyridyl (**16**) resulted in somewhat slower cleavage rates. This result hints at potential additional payload interactions within the P1' site residue with CatB. One consideration was the well accepted view that the S₁' side of the active site is surrounded by hydrophobic residues, which might lead to unfavorable ligand pose for these charged/polar substrates and thus explain the decreased $t_{1/2}$ ^{135,141,142}. However, the observed reasonable cleavage rates for the *p*-Me₂N-aniline **6** and thiophene-2-carboxylate derivatives **17** and **18** contradicts this hypothesis.

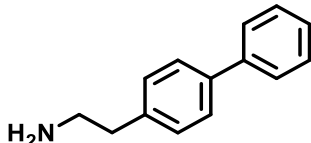
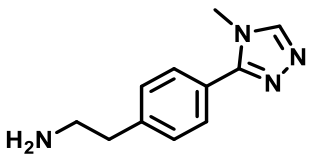
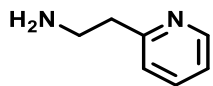
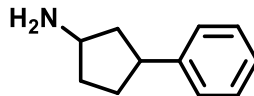
The CatB-catalyzed anilide hydrolysis, however, was strongly dependent on steric effects with ortho substituted anilides showing extremely long $t_{1/2}$ (>10 h, substrates **13** and **15**). This result can be explained by distortion of the planarity of the aniline amide bond, which strongly disfavors the nucleophilic attack by the catalytic cysteine residue to form the tetrahedral intermediate—the key step necessary for amide bond cleavage.

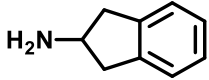
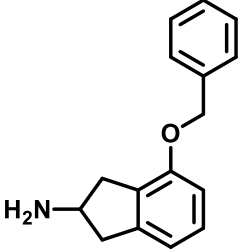
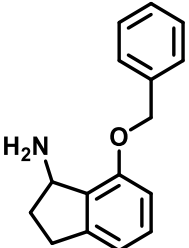
3.3.2 Cleavage of Gly-Gly-Phe-Gly-Aliphatic and Benzylic Amine Substrates

Primary or secondary alkyl amines are the most frequently used chemical groups to connect a drug molecule to an ADC via a cleavable linker. To ensure efficient drug release, self-immolative spacers, such as p-aminobenzyloxycarbonyl (PABC), are frequently incorporated between the primary amine and the cleavable peptide sequence. While PABC incorporation allows fast payload release, it also leads to increased hydrophobicity of the linker-payload, which can result in ADC aggregation, especially at high drug-to-antibody ratios (DAR)¹⁴³. To understand the feasibility of cleaving alkyl amines in the absence of self-immolative linkers, we screened the hydrolysis of alkyl amide substrates under the same CatB conditions as the aniline-based substrates. Similar to the aniline assay, the alkyl amide library was designed to connect a primary amine directly to the GGFG C-terminus. The selection of alkyl amines was limited to detectable compounds stable under the assay conditions with a narrow scope of alkyl amide substrates being susceptible to CatB-mediated cleavage. Representative data are summarized in Table 3-2 with all screened substrates and their respective curves available in the appendix. In general, all alkyl amine substrates exhibited longer $t_{1/2}$ compared to those of anilide analogues. Faster release rates were observed with alkyl amines attached to highly hydrophobic cores, but the rate significantly

decreased with cores containing heterocycles. For example, the cleavage rate of **21**, containing 1,2,4-triazole, was almost ten times slower than the biaryl analogue **20**.

Table 3-2 CatB mediated cleavage of GGFG-alkylamines

Substrate	Released Amine	$t_{1/2}$ (h) ^{a,b}	95% CI of $t_{1/2}$
20		1.2	[0.7-2.0]
		0.7	[0.7-0.8] ^c
21		7.2	[5.1-10.2]
22		5.1	[3.7-7.4]
23		2.3	[1.9-2.7]

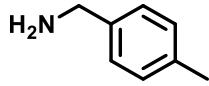
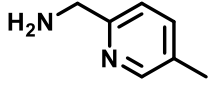
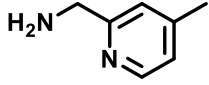
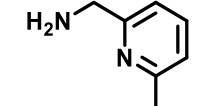
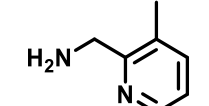
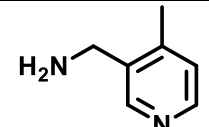
24		24a	1.1	[1.0-1.4]
25		25a	0.6 0.7	[0.6-0.7] [0.5-0.8] ^c
26		26a	3.4	[2.4-5.4]

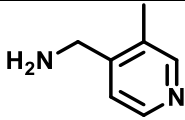
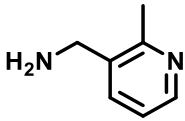
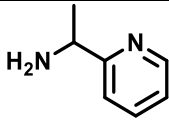
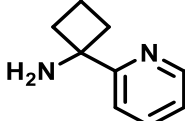
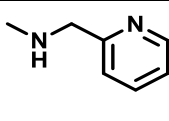
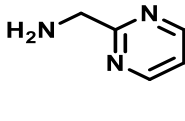
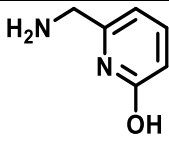
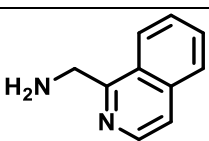
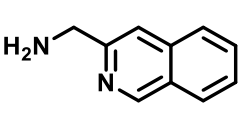
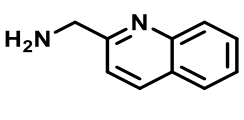
^aAll reported substrates were stable and showed cleavage only in the presence of CatB. The 24-hour stability of substrates and amine payloads were assessed by incubation under assay conditions with and without cathepsin enzyme present. ^bMeasured by HR-LCMS against an internal standard. The reported values are an average of three runs. ^c Different batch of enzyme was used.

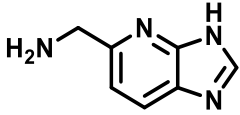
A broader scope SAR study was feasible with a range of benzylic amines due to compound availability. The data from representative examples are summarized in Table 3-3 with all screened substrates and their respective curves available in the appendix. *p*-Me-benzylamine GGFG conjugate **27** reacted under assay conditions with a $t_{1/2} = 6$ h. This cleavage rate is significantly slower compared to the *p*-toluidine derivative **1**. Switching from aryl (**27**) to the 2-pyridyl (**28**) substituent slightly accelerated substrate cleavage, the exact reason not yet determined. Furthermore, a simple methyl group walk on the pyridyl core (**28-31**) further shortened substrate cleavage rates. Thus, the $t_{1/2}$ of substrate **30**, was as short as 20 min, comparable to the observed

$t_{1/2}$ for the most active GGFG-anilines in Table 3-1. Further SAR analysis showed that the position of the nitrogen in the pyridyl influences the rate of hydrolysis with the 3-pyridyl analogues **32** and **34** undergoing much slower hydrolysis and the 4-pyridyl substrate **33** not cleaving at all. Like the anilides, cathepsin-mediated cleavage for benzyl amines was sensitive to steric effects. Slower cleavage was observed for substrates with substitution at the benzylic position. For example, cyclobutyl derivative **36** cleaved with a $t_{1/2} = 9$ h and secondary (2-methylaminomethyl)pyridine substrate **37** did not show any detectable cleavage after 24 hours.

Table 3-3 CatB mediated cleavage of GGFG-benzylamines

Substrate	Released Amine		$t_{1/2}$ (h) ^{a,b}	95% CI of $t_{1/2}$
27		27a	6.5	[4.5-8.4]
28		28a	4.5	[3.4-7.6]
			3.1 ^d	[2.5-3.4] ^d
29		29a	1.4	[1.2-1.7]
30		30a	0.4	[0.3-0.4]
31		31a	1.3	[1.0-1.7]
32		32a	14.6	[10.3-20.4]

33		33a	No cleavage	-
34		34a	15.9	[9.8-26.5]
35		35a	3.6	[2.3-4.8]
36		36a	7.6	[5.0-11.3]
37		37a	No cleavage	-
38		38a	1.7	[1.5-2.1]
39		39a	5.8	[4.3-8.2]
40		40a	0.7 0.5 ^d	[0.5-0.8] [0.48-0.55] ^d
41		41a	20.0	[12.8-34.8]
42		42a	2.4	[2.2-2.7]

43		43a	9.8 10.8 ^d	[6.1-15.0] [8.5-13.7] ^d
----	---	-----	--------------------------	---------------------------------------

^aAll reported substrates were stable and showed cleavage only in the presence of CatB. The 24-hour stability of substrates and amine payloads were assessed by incubation under assay conditions with and without cathepsin enzyme present. ^bMeasured by HR-LCMS against an internal standard. The reported values are an average of three runs. ^c Different batch of enzyme was used.

3.3.3 Cleavage of peptide conjugates other than GGFG

Intrigued by the reactivity of GGFG conjugates with polysubstituted ortho-pyridyl methyl amines in the presence of CatB, we sought to understand if this reactivity could also be observed with other peptide sequences. We chose **40a** as a model amine for these studies, as the $t_{1/2}$ of the GGFG-**40a** conjugate was below one hour, and it was stable under assay conditions. We chose Val-Cit, Val-Gly, Ala-Ala, Phe-Lys-Gly, and Gly-Gly-Gly peptide linkers as these dipeptide and tripeptide sequences are commonly used in preparation of clinical grade ADCs¹⁴⁴. It has been shown that longer peptide sequences have higher affinity to the cathepsin pocket (maximum of four residues) and thus tetrapeptide-based linkers might be better suited for efficient payload release compared with dipeptides. Indeed, the Val-Cit-**40a** substrate **44** cleaved significantly slower in our assay. On the other hand, dipeptide Val-Cit is a well-validated linker used in the FDA approved ADCs Adcentris®, Polivy®, and Padsev®. However, the N-terminus of this peptide is modified with an additional extension that connects the linker payload to the antibody. One could postulate that this extension can also improve the binding of the linker in the protease pocket. Moreover, commercially available CatB substrates are benzyl formate (Cbz) protected dipeptide derivatives (e.g., Cbz-Arg-Arg-coumarin). When the N-terminus of **44** was protected with tert-butyloxycarbonyl (Boc) (**45**) or Cbz (**46**) (Figure 3-2 and Table 3-4), significant (>10X)

acceleration of substrate cleavage was observed. However, functionalization with longer linkers (47 and 53) did not yield further improvements in cleavage rates. Among other peptide sequences tested, Phe-Lys-Gly (55) showed the most efficient cleavage with $t_{1/2}$ for Cbz-Phe-Lys-Gly-40a being only 4 min. The substrate 57 with the L-Ala-L-Ala peptide cleaved slower and no cleavage was observed with tri-Gly 56, nor the D-peptide derivative 58.

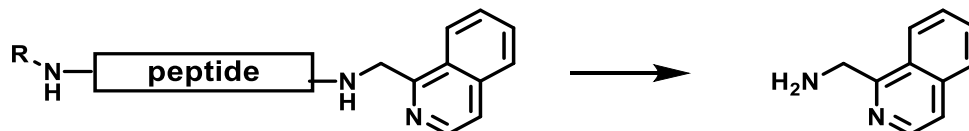
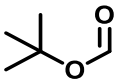
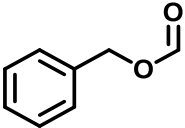
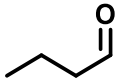
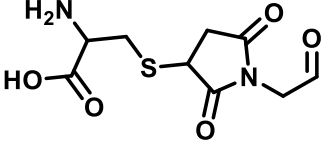
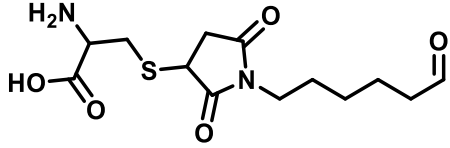
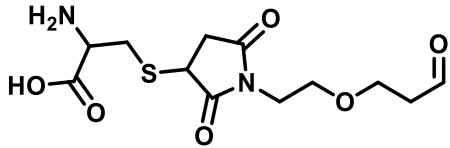
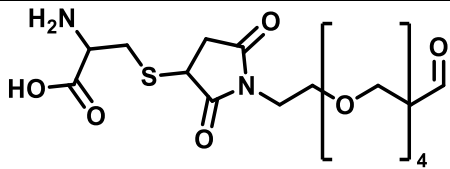
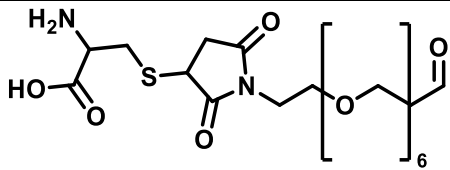
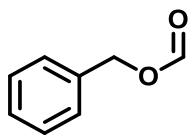


Figure 3-3 Scheme for substrates 44 through 58.

Table 3-4 CatB mediated cleavage of peptide conjugates with 40a

Substrate	R Group	Peptide	$t_{1/2}$ (h) ^{a,b}	95% CI $t_{1/2}$
44	H	Val-Cit	4.2	[3.3-5.5]
45	Boc 	Val-Cit	0.4	[0.4-0.5]
46	Cbz 	Val-Cit	0.2 0.3 ^c	[0.2-0.3] [0.2-0.5] ^c
47		Val-Cit	0.3	[0.28-0.31]
48	Gly	Val-Cit	0.5	[0.5-0.6]

49		Val-Cit	1.0	[0.9-1.3]
50		Val-Cit	0.3	[0.1-0.5]
51		Val-Cit	0.9	[0.6-1.6]
52		Val-Cit	0.6	[0.5-0.7]
53		Val-Cit	0.5	[0.5-0.7]
54	<p style="text-align: center;">Cbz</p> 	Val-Gly	1.0	[0.9-1.1]
55		Phe-Lys-Gly	0.07	[NA-0.1]
56		Gly-Gly-Gly	No cleavage	-
57		L-Ala-L-Ala	3.1 4.2 ^c	[2.5-3.9] [3.1-6.4] ^c
58		D-Ala-D-Ala	No cleavage	-

^aAll reported substrates were stable and showed cleavage only in the presence of CatB. The 24-hour stability of substrates and amine payloads were assessed by incubation under assay conditions with and without cathepsin enzyme present. ^bMeasured by HR-LCMS against an internal standard. The reported values are an average of three runs. ^c Different batch of enzyme was used.

3.3.4 Cleavage of Gly-Gly-Phe-Gly conjugates with other peptidases

A subset of GGFG substrates were also assayed with cathepsin S (CatS), cathepsin L (CatL), and an endolysosomal mixture from rat liver tritosomes^{139,145-147}. CatS peptidase was reported to be expressed in endosomal compartments of antigen presenting cells, including macrophages, B cells, dendritic cells, and some epithelial cells¹⁴⁸. This enzyme plays an important role in antigen presentation, facilitating antigen loading onto MHCII. CatL is known to be overexpressed in cancer cells and is considered the most potent among human cysteine proteases. Rat liver tritosomes are hepatic subcellular fractions of liver tissues containing high levels of different peptidases^{149,150}. Tritosomes are frequently used to assess cleavage and drug release from a variety of protein constructs, including ADCs. The experimental design of the study is summarized in Figure 3-4. We selected 10 representative GGFG peptide conjugates with aniline or alkyl amines to be additionally cleaved by CatL, CatS, or tritosomes. To assess substrate performance across peptidases, we used a scoring system based on relative rates. Values were normalized to the substrate with the highest activity in each peptidase group which was assigned a value of 100. The selected GGFG conjugates showed fast cleavage in the presence of CatB, with GGFG anilides being among the most active substrates in the group (substrates **18**, **19**, and **5**). In general, this rank order translated onto other protease groups, except for Cbz-Val-Cit-**40a** (**46**) which was the most active compound in CatL and CatS-mediated cleavage. Facile substrate cleavage was observed using rat liver tritosomes across multiple substrates pointing to the involvement of multiple proteases in substrate decomposition.

It should be noted that some substrates were assayed multiple times with CatB and some variation in $t_{1/2}$ was observed due to using different batch of enzyme and slight differences in how it was activated prior to incubation (substrates **18-20**, **25**, **28**, **40**, **43**, **46**, and **57**). A bridging

experiment was performed to evaluate all CatB batches used and it was determined that despite different “specific activity” values provided by the manufacturer performance across all enzymes were deemed comparable with little variation.

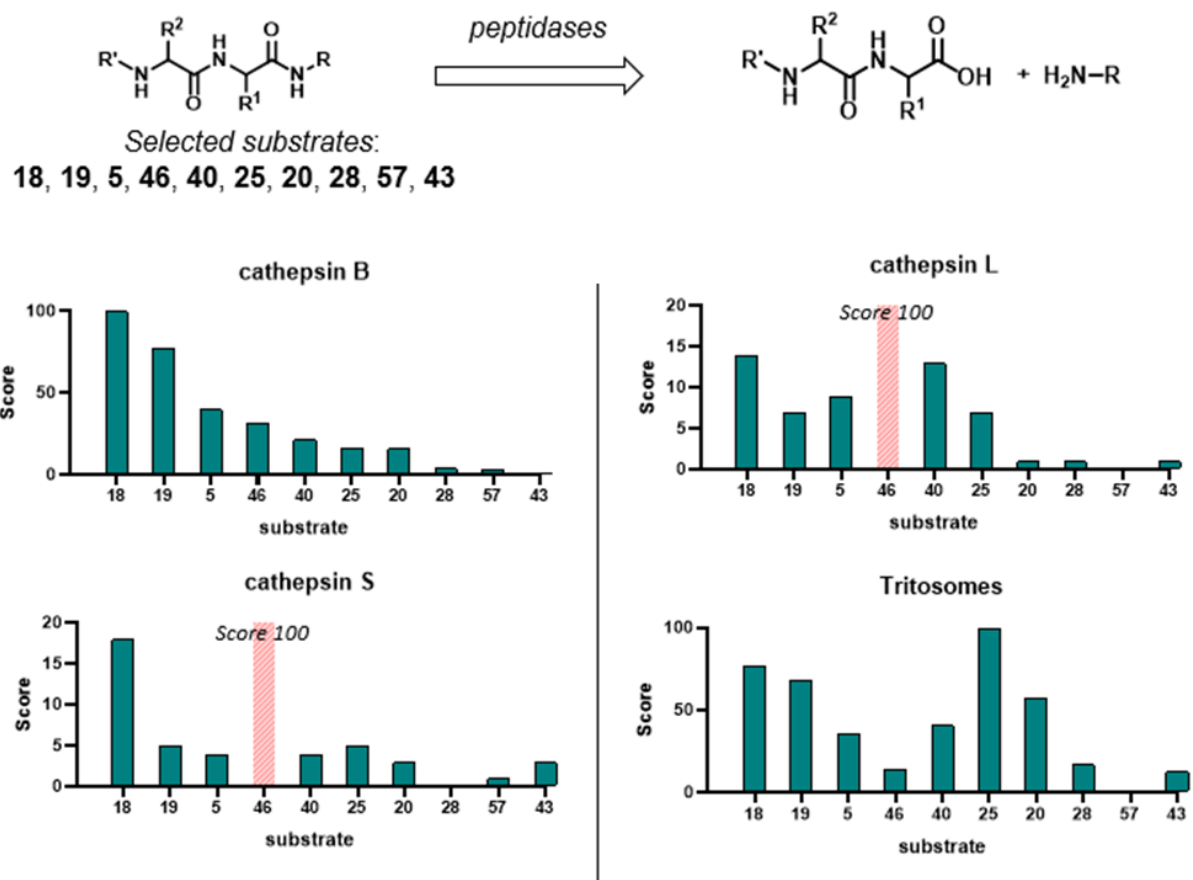


Figure 3-4 Relative substrate cleavage scores with different peptidases. All data reported as an average of 3 runs.

3.4 Conclusions

Our studies indicated that, in the presence of CatB, aryl amines underwent the fastest cleavage from the tetrapeptide GGFG. The cleavage rate was primarily driven by sterics, thus substrates containing ortho-substituted anilines showed extremely long $t_{1/2}$. In addition to aryl amines, comparable rates could be achieved using substituted ortho-pyridyl methyl amines. This

reactivity was not only specific to GGFG conjugates but also enhanced observed cleavage rates for FKG tripeptide derivatives. We found that alkylamines were generally the slowest among the different amine classes, with the fastest rates observed for polyaromatic amines and slowest with heterocyclic substrates among the alkylamines screened. These results are consistent with literature reports that the S1' pocket of CatB has a general preference for accepting hydrophobic substrates¹⁵¹.

Overall, our screening efforts have shed some additional light on the release rates of aromatic and aliphatic amines from cathepsin cleavable linkers. To this day, anilines have been the only class of amines that can be efficiently released from peptide linkers. This reactivity found its application in the development of self-immolative spacers such as PABC, fluorescent coumarin-based peptide probes, as well as cytotoxic payload designs. The work described herein examining the release rates of aromatic, aliphatic, and benzylic amines identified additional scaffolds based on 2-pyridyl methyl amines that can be efficiently released from peptide conjugates in the presence of cathepsins and other endolysosomal peptidases. We believe these new findings can find applications in the construction of next generation therapeutics and ADCs.

Chapter 4: Supercharging in Hydrogen/Deuterium Exchange-Mass Spectrometry Workflows for Increased Antibody Sequence Coverage and Electron-Transfer Dissociation Efficiency

4.1 Introduction

Recombinant immunoglobulin gamma (IgG) monoclonal antibodies constitute the largest contributor in current biotherapeutic development. The function of these IgGs is strongly related to their structure which can be moderately elucidated using bottom-up hydrogen/deuterium exchange mass spectrometry (HDX-MS)^{152–154}. While only moderate structural resolution can be achieved via HDX-MS, requirements for protein purity and amounts are less stringent compared with other structural analytical techniques. Tandem mass spectrometry (MS/MS) and high redundancy in peptide mapping may allow for amino acid residue level resolution of deuterium incorporation beyond simple whole-peptide quantification of deuterium uptake^{155,156}. In a typical bottom-up workflow in which the labeled protein is subsequently digested with pepsin due to high activity at low pH, shorter, overlapping low charge state peptic peptides are typically generated. While it can be advantageous to have a high degree of peptide overlap, allowing for improved structural resolution, low charge state peptides exhibit low fragmentation efficiency, particularly with electron-based fragmentation methods^{92,157}. Increasing the average charge state is desired for improved identification through MS/MS¹⁵⁸.

While collision-induced dissociation (CID) is the most commonly available MS/MS activation technique available in commercially available mass spectrometers, the accompanying slow heating causes extensive gas-phase hydrogen scrambling, thus randomizing the backbone

deuterium uptake from solution^{102,155}. By contrast, alternative activation methods such as electron capture/transfer dissociation (ECD/ETD) have been shown to proceed without hydrogen scrambling. However, such methods require relatively high charge state ($\geq 2+$) for efficient fragmentation. Supercharging agents have been shown to allow for an increase in peptic peptide average charge state for smaller model proteins¹⁵⁹.

Here, we apply the supercharging agent (SCA) m-nitrobenzyl alcohol (m-NBA) to peptic peptides generated from antibodies. Supercharging agent is introduced via a post-column tee in a bottom-up HDX workflow with the goals to increase both the total peptide spectrum matches (PSMs) from CID MS/MS of non-deuterated peptides, and to improve electron-based fragmentation efficiency.

4.2 Experimental Methods

4.2.1 Chemicals and Reagents

All chemicals and reagents were purchased from Sigma-Aldrich (St. Louis, MO) unless stated otherwise. Pepsin was from porcine gastric mucosa and the IgG1 was SiLuTMLite SigmaMAb universal antibody standard, human. Herceptin® and Remicade® were generously provided by Professor Anna Schwendeman and buffer exchanged into water to remove any excipients prior to digestion and analysis.

4.2.2 Offline pepsin digestion

To prevent over digesting the antibodies to favor generation of many short and low charge state peptides, a potent pepsin inhibitor effective at picomolar concentrations, pepstatin^{160,161}, was added to the sample prior to MS analysis. We had previously observed that offline digested

samples prepared at the same time would show different levels of digestion depending on when the same was injected. Samples injected soon after digestion would result in detection of longer peptides with a higher number of identifications whereas samples that sat in the autosampler, albeit chilled, after 30 minutes showed shorter peptides and less sequence coverage. It is possible that digestion continued during the trap column washing step.

Antibody stock solutions were used at a concentration of 1 mg/mL in water. Pepsin was prepared at a concentration of 1.5 mg/mL in water, pH 3. Pepstatin was prepared at a concentration of 0.1 mg/mL in MeOH with 1% formic acid (v/v) and used at a 1:1 molar ratio with pepsin. Quench buffer (200 mM sodium phosphate, 3 M guanidine hydrochloride, 500 mM tris(2-carboxyethyl)-phosphine hydrochloride, pH 2.4 in water) was added to the antibody stock and allowed to react for 3 min at room temperature (RT). Subsequently, pepsin was added in a ratio of 1:1.5 antibody:pepsin and the digestion proceeded for 3 min at RT before pepstatin was added.

4.2.3 Mixing Tee

While adding SCA directly to the mobile phase is convenient and easy to implement, doing so results in retention time peak shifting inversely related to SCA concentration^{65,66,159}. As a workaround to avoid exposing the column to *m*-NBA, a static mixing tee (IDEX Health and Science, Oak Harbor, WA) was implemented to incorporate SCA after separation. Eluent flow from the LC column was 200 μ L/min while 2% *m*-NBA was infused at 10 μ L/min, allowing for a final concentration of 0.1%, see **Error! Reference source not found.**

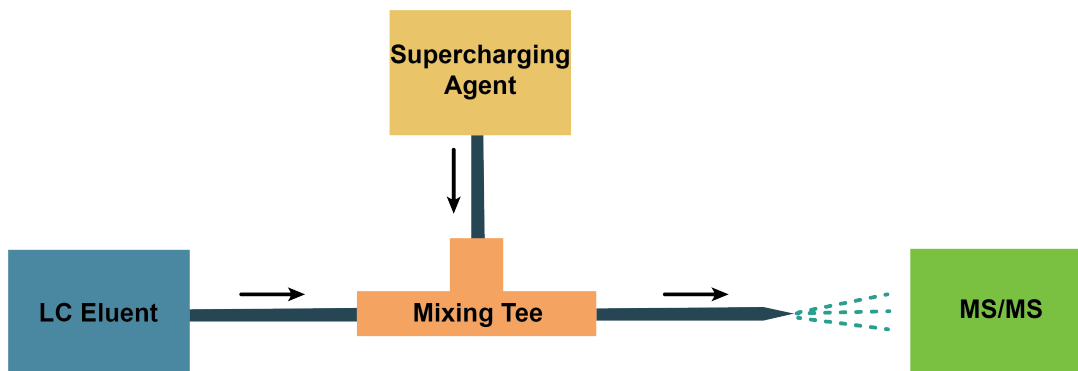


Figure 4-1 Schematic representation of mixing tee used for SCA addition without impacting separation. Arrows indicate flow directionality. LC eluent was set to 200 $\mu\text{L}/\text{min}$ while *m*-NBA was infused at 10 $\mu\text{L}/\text{min}$. All tubing was 130 μm i.d.

Originally, the setup included a syringe pump to deliver the SCA to the tee, however, the syringe pump paddle was not able to maintain a constant backpressure and, thus, over time the syringe would fill with LC eluent. An Agilent 1290 Infinity II binary pump used for LC separations was therefore implemented to introduce the SCA into the mixing tee. During LC/MS runs, the binary pump delivering the SCA showed a backpressure of 4–5 bar while the pump used for generating the separation gradient was between 40 and 80 bar.

4.2.4 LC-MS Parameters

Initial MS1 experiments were performed in positive ion mode on a 7T Solarix quadrupole Fourier transform ion cyclotron resonance (FT-ICR) mass spectrometer (Bruker Daltonics, Billerica, MA) equipped with an Apollo II ESI source. The capillary voltage, capillary exit voltage, funnel 1 voltage, drying gas flow rate and temperature were set to 4500 V, 280 V, 120 V, 4.0 L/min and 130 $^{\circ}\text{C}$, respectively. Data were collected from m/z 200 to 2000 with 0.25 s accumulation time, corresponding to 512k transients. The digests were injected onto a C18 column (Phenomenex Kinetex 5 μm EVO 50 x 2.1 mm) and the LC gradient was 0% B for 1 min then

ramping from 5 to 75% B in 10 min at 200 $\mu\text{L}/\text{min}$ (A: water:formic acid 99.9:0.1 (pH=2.5); B: acetonitrile:formic acid 99.9:0.1 (pH=2.5)).

HCD and ETD MS/MS experiments were performed in positive ion mode on an Orbitrap Fusion Lumos mass spectrometer (Thermo Fisher Scientific, San Jose, CA) equipped with a heated ESI probe (HESI). Source conditions were set at 4000 V, 35, 10, 0, 300 $^{\circ}\text{C}$, and 275 $^{\circ}\text{C}$ for spray voltage, sheath gas, auxiliary gas, sweep gas, ion transfer tube temperature, and vaporizer temperature, respectively. For HCD experiments, cycle time was set to 3 s and MS1 parameters included 240k resolution with an m/z range between 200 – 2000 m/z and the RF lens set at 45% RF. Dynamic exclusion was enabled to exclude precursor ions after 1 scan for 30 s. For data dependent HCD, the intensity threshold was set to 5.0×10^3 . HCD experiments used a quadrupole isolation window of 1.6 m/z with stepped collision energies at 25, 30, and 35%. For ETD experiments, MS1 and dynamic exclusion settings remained the same as for HCD experiments. However; a higher intensity threshold of 1.0×10^5 was applied due to the lower ETD fragmentation efficiency. Precursor selection range varied depending on the precursor charge state, i.e., 3+ precursors selection range was set to 200 – 650 m/z, 4+ precursors selection range was set to 200 – 900 m/z, 5+ precursors selection range was set to 200 – 950 m/z. For data dependent ETD, the quadrupole isolation window was set to 2 m/z and calibrated charge-dependent ETD parameters were applied. The offline digested samples were injected onto a C8 trap column (ZORBAX StableBond, 2.1 x 12.5 mm, 5 μm , 80 \AA) for desalting and separated by a C18 column (ZORBAX RRHD 300SB-C18 2.1 x 50 mm) before MS analysis. The LC gradient was 0 % B for 5 min for desalting, then 15 to 45 % B for 12 min at 200 $\mu\text{L}/\text{min}$ followed by 95% B for 6 min to wash the column prior to the next sample (A: water:FA 99.9:0.1 (pH=2.5); B: ACN:FA 99.9:0.1 (pH=2.5)).

4.2.5 Database search parameters

Data analysis for initial MS1 experiments was performed manually using Bruker Data Analysis 5.0. Theoretical peptide ion masses were determined by the MS digest function in Protein Prospector (<https://prospector.ucsf.edu/prospector/cgi-bin/msform.cgi?form=msdigest>) and the experimental data were manually annotated using a comparative in-house Excel macro. Variable modifications were set to methionine oxidation and pyroglutamic acid with up to 10 missed cleavages with pepsin. Peptides were only assigned if the mass error was ≤ 15 ppm.

Subsequent database searches were conducted using Thermo Proteome Discoverer 2.2.0.388¹⁶². Sequence information for each antibody was downloaded from Uniprot.org and imported. For HCD experiments, precursor and fragment ions mass tolerance was set to 0.1 Da and 0.6 Da, respectively. For ETD experiments, precursor mass tolerance was set to 10 ppm for precursor and fragment ions. PSM data were exported, and average charge state calculated using an in-house R script.

4.3 Results and Discussion

4.3.1 Increased Average Charge State MS1

The effect of SCA on antibody peptic peptide average charge state (q_{avg}) was calculated using Equation 4-1.

Equation 4-1

$$q_{avg} = \frac{\sum_i^N q_i W_i}{\sum_i^N W_i}$$

in which N denotes the number of observed peptide charge states and q_i is the charge of the i th charge state. W_i is the abundance of the i th charge state normalized to charge as signal abundance in the image current detection performed in the Orbitrap is proportional to charge.

Changes in IgG1 peptic peptide charge-state distributions were observed upon addition of *m*-NBA; overall from 33% to 29% 1+ ions, 47% to 33% 2+ ions, 16% to 20% 3+ ions, and 4% to 19% $\geq 4+$ ions (Figure 4-2). The average peptic peptide charge state also increased from +1.5 to +1.9 for IgG1. This change is significant because electron-based MS/MS techniques are incompatible with 1+ ions and ETD in particular shows poor fragmentation yield for 2+ ions. Higher charge state precursor ions provide more abundant fragment ions and thus improve localization of deuterium. Example mass spectra for the peptic peptide VLQSDLYTLSSSVTVPSSPRPSETVTCNVAHPASSTKVDKKI with and without *m*-NBA are shown in Figure 4-3. For this peptide, complete depletion of 2+ ions to 3+ and 4+ ions was observed.

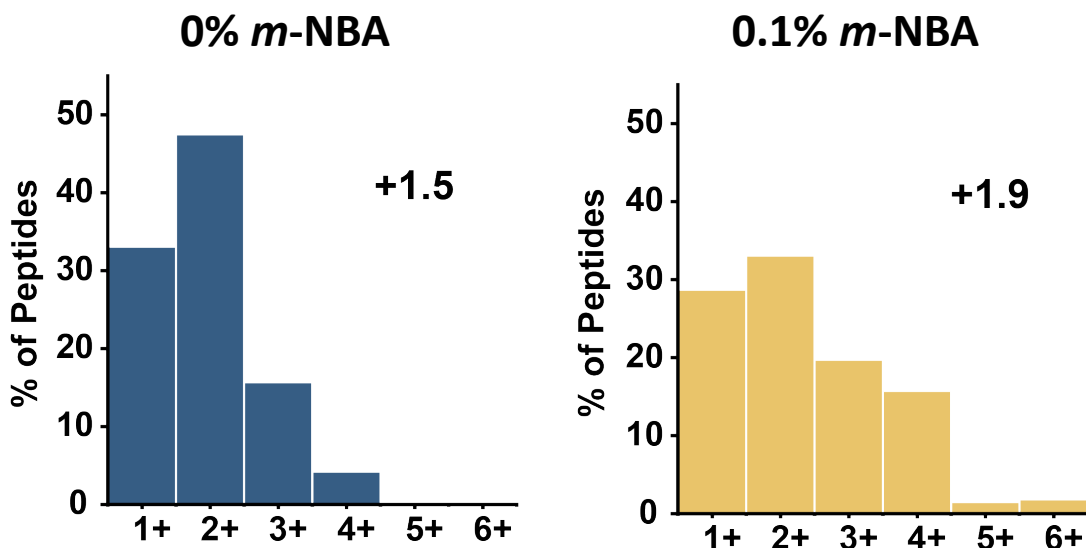


Figure 4-2 Bar graphs representing charge state distributions for IgG1 peptic peptides without (left) and with (right) 0.1% *m*-NBA. Calculated average charge states for each are shown in the upper right of each bar graph.

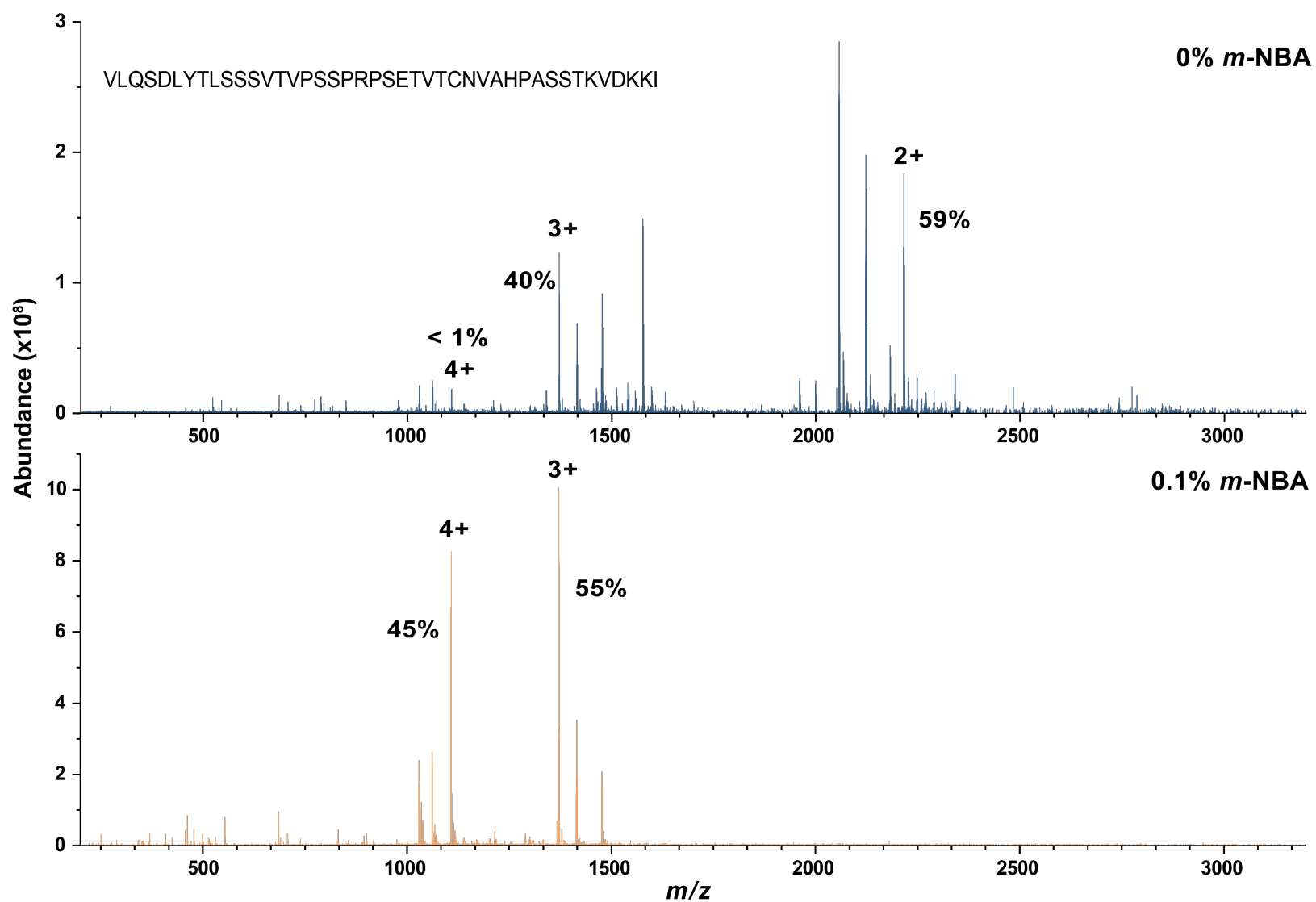


Figure 4-3 MS1 spectra of peptide from pepsin digest of IgG1 with and without 0.1% *m*-NBA collected on a 7T Solarix Q-FT-ICR mass spectrometer.

4.3.2 Improved Sequence Coverage and PSM count

Peptic peptide LC-HCD MS/MS experiments for IgG1 revealed improved sequence coverage upon supercharging shown in Table 4-1. Due to the utilized offline digestion workflow, digestion can continue during desalting, resulting in peptide loss. This potential problem prompted the addition of pepstatin, a potent pepsin inhibitor. This inhibitor also aided in generating longer peptides capable of carrying more charge. A total of four sample preparation replicates were used for IgG1 analysis, whereas Herceptin and Remicade have two sample preparation replicates tested

For Herceptin and Remicade, the observed average peptic peptide charge state was slightly lower upon supercharging (Table 4-2 and Table 4-3). This apparent paradox is attributed to the greater number of 2+ ions identified with supercharging: even in HCD, 1+ ions typically fragment poorly and are thus excluded from MS/MS, i.e., the 1+ precursor ions did not contribute to the MS/MS-based average charge state calculations. By contrast, if the same peptide appears as a 2+ ion following supercharging, it will be selected for MS/MS and thus contribute to the charge state analysis. An additional advantage of higher charge state precursor ions is the potential to generate a larger variety of fragment ions as, e.g., both complementary fragments from a 2+ ion can carry charge following HCD.



IgG1

Figure 4-4 IgG1 structure consisting of four units, two heavy chains and two light chains connected via disulfide bonds. Heavy chains shown in dark blue while light chains shown in yellow.

Table 4-1 LC HCD MS/MS outcome for IgG1 pepsin digests with and without SCA.

		% Coverage	Unique Peptides	PSM	% PSM >2+	Avg. Charge State
0% <i>m</i> -NBA	IgG1 Heavy	75 ± 6 %	29 ± 5	39 ± 9	51 %	2.3
	IgG1 Light	76 ± 9 %	11 ± 5	21 ± 4		
0.1% <i>m</i> -NBA	IgG1 Heavy	85 ± 5 %	53 ± 5	70 ± 7	61 %	2.7
	IgG1 Light	96 ± 5 %	21 ± 2	39 ± 4		

Table 4-2 LC HCD MS/MS outcome for Herceptin pepsin digest with and without SCA.

		Unique Peptides	PSM	Avg. Charge State
0% <i>m</i> -NBA	Herceptin Heavy	233	367	3.0
	Herceptin Light	132	189	
0.1% <i>m</i> -NBA	Herceptin Heavy	617	867	2.9
	Herceptin Light	301	429	

Table 4-3 LC HCD MS/MS outcome for Remicade pepsin digest with and without SCA.

		Unique Peptides	PSM	Avg. Charge State
0% <i>m</i> -NBA	Remicade Heavy	389	625	3.0
	Remicade Light	218	293	
0.1% <i>m</i> -NBA	Remicade Heavy	587	783	2.8
	Remicade Light	305	377	

4.3.3 Supercharging Effects in ETD MS/MS of Antibody Peptic Peptides

Comparing LC-ETD MS/MS runs of IgG1 pepsin digests with and without SCA resulted in similar sequence coverage and total PSMs. However, further inspection of assigned PSMs yielded several peptides identified only with supercharging that were not observed when supercharging was not applied. In particular, Figure 4-5 through **Error! Reference source not found.** highlight some of these peptides and their respective scoring¹⁶³. Cross correlation (XCorr) scores are based on how many experimental fragments match with the database, and scores > 2 are considered favorable. Detection of these additional peptides upon supercharging may be due to increased precursor ion abundance resulting in higher quality ETD spectra, or supercharging may have yielded higher charge states showing improved ETD efficiency. It is also possible that some combination of these effects resulted in these unique matches.

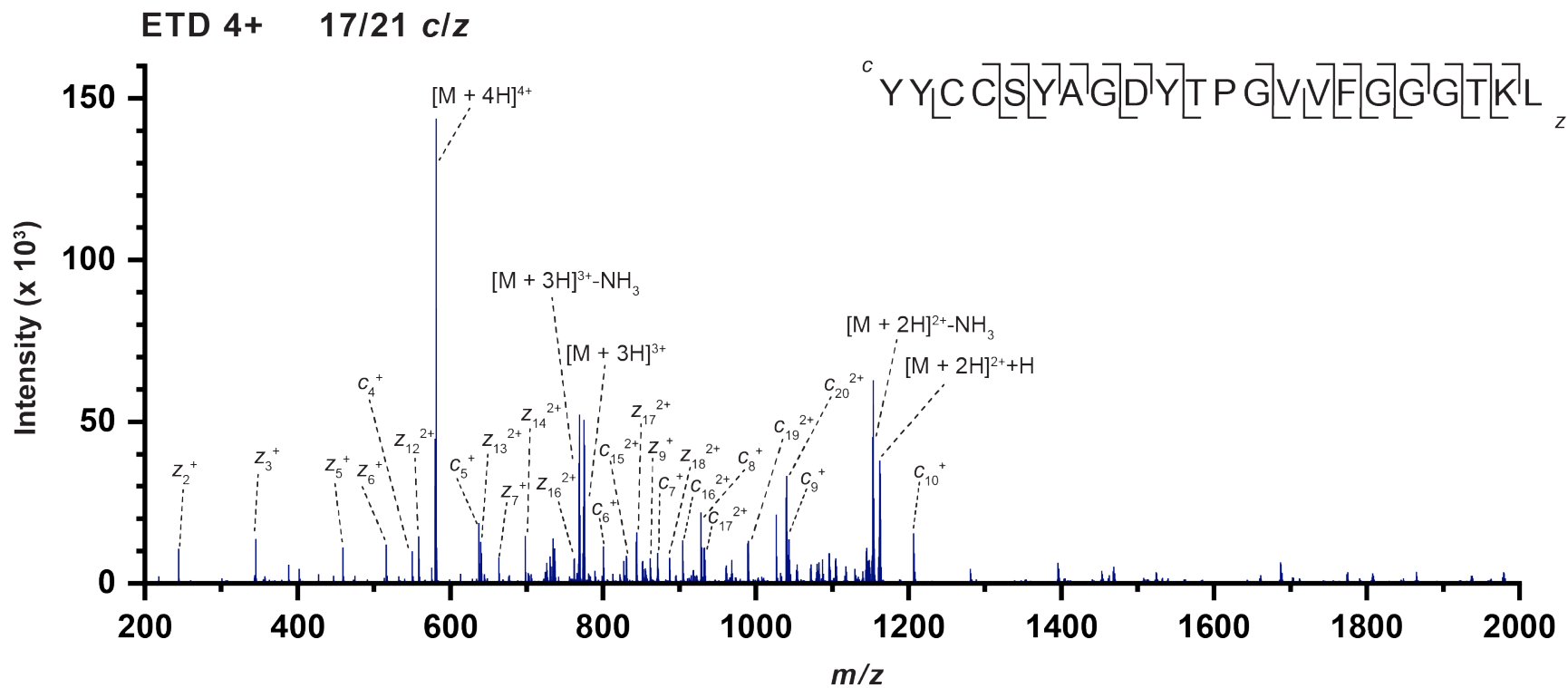


Figure 4-5 ETD MS/MS spectrum of the quadruply protonated peptic peptide YYCCSYAGDYTPGVVFFGGGTKL from IgG1 only identified following supercharging with an XCorr score of 7.85

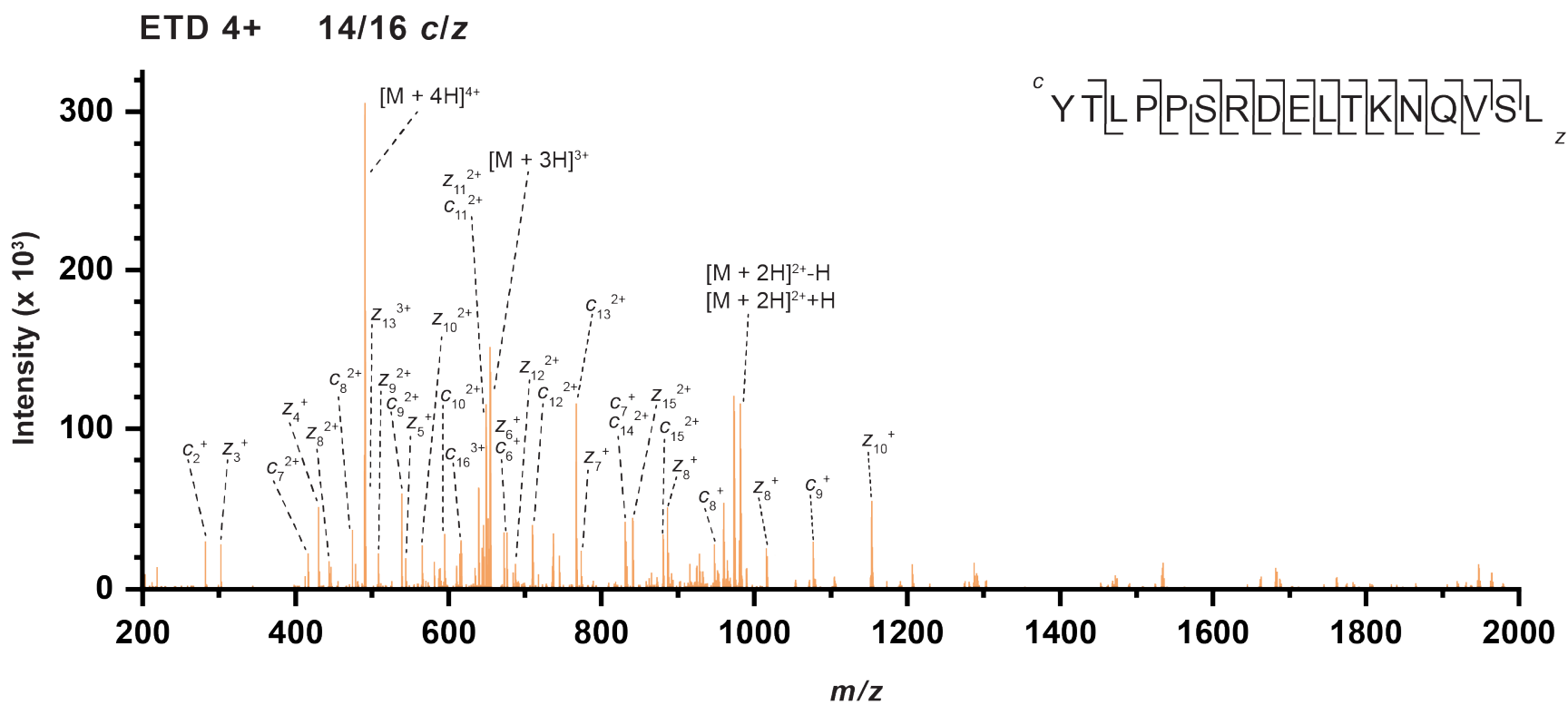


Figure 4-6 ETD MS/MS spectrum of the quadruply protonated peptic peptide YTLPPSRDELTKNQVSL from IgG1 with an XCorr score of 6.75.

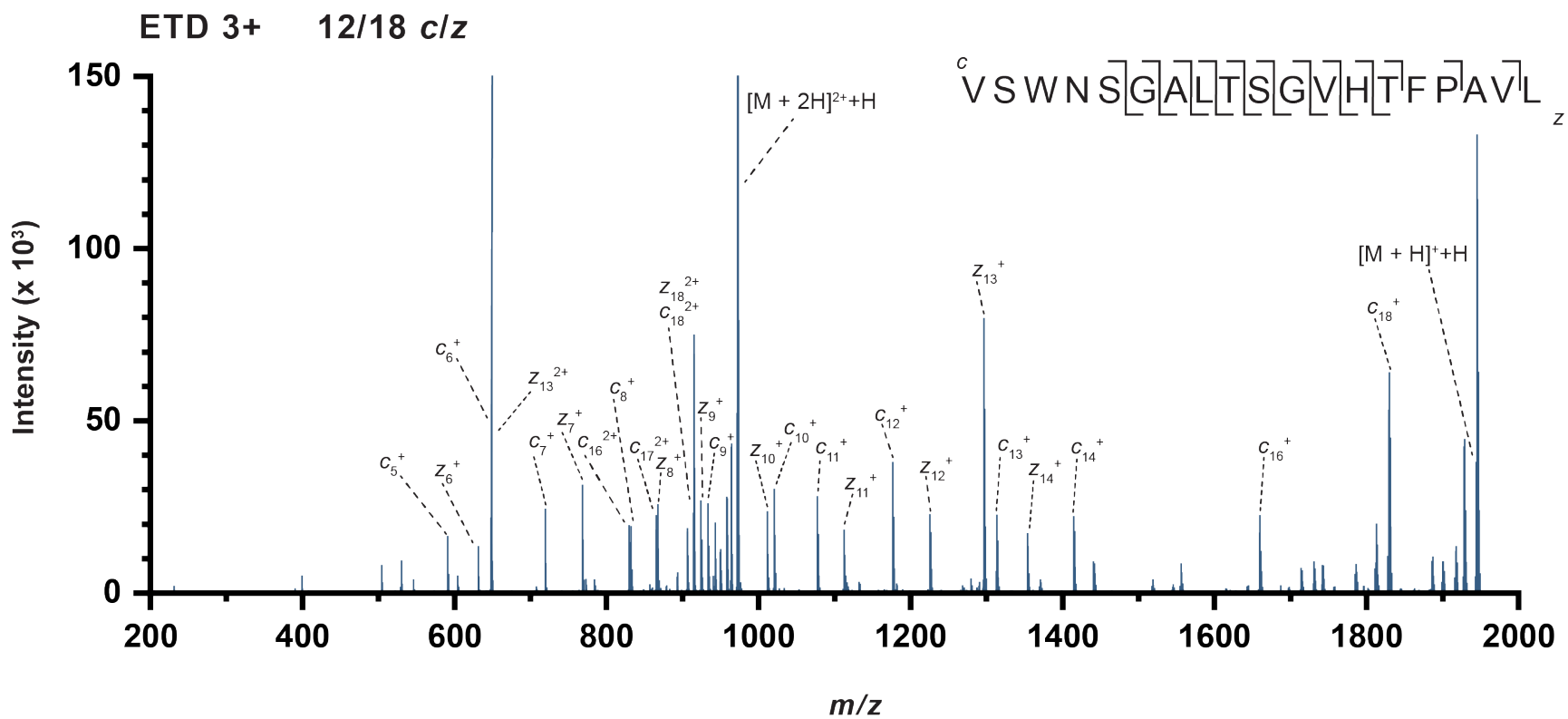


Figure 4-7 ETD MS/MS spectrum of the triply protonated peptic peptide VSWNSGALTS[GVHT]FP[AVL]L from IgG1 with an XCorr score of 6.08.

4.4 Conclusions

In this chapter, the benefit of supercharging antibody peptic digests in an HDX workflow is demonstrated. The therapeutics Herceptin and Remicade along with human IgG1 were offline digested with pepsin in the presence of a pepsin inhibitor prior to chromatographic separation with *m*-NBA added post-column. Upon supercharging with *m*-NBA, both the number of PSMs and the number of unique peptides observed in LC-HCD MS/MS doubled for Herceptin and IgG1 compared to the absence of SCA. In addition, three PSMs were identified in LC-ETD MS/MS following supercharging of IgG1 peptic digests that were not found in the absence of *m*-NBA. Further work incorporating deuterium labeling as well as studies to determine scrambling are needed to fully maximize the utility of this technique.

Chapter 5: Conclusions and Future Directions

5.1 Dissertation Summary

In this dissertation, we presented mass spectrometry-based workflows aimed at improving drug development applications. These applications spanned from targeted and untargeted high throughput to structural characterization using HDX and demonstrated the wide utility of MS analysis for drug design.

Chapter 2 covers a droplet-MS workflow developed to increase screening throughput for a directed evolution campaign. Saxitoxin, as well as other natural products of therapeutic interest, are synthesized in nature using enzymes capable of synthetically challenging transformations. Using directed evolution, wildtype enzymes can be modified to accept non-native substrates with desirable activity which can aid in drug design of novel payloads. While extremely large (10^9) mutant libraries can be generated by taking advantage of genetic variation and error prone PCR, screening these libraries remains a bottleneck¹⁶⁴. Using droplet-MS as an alternative to LC-MS/MS and optimizing MRM parameters to detect low amounts of turnover in crude cell lysate, screening throughput was increased to allow for 768 variants to be screened in triplicate under 7 hrs. Additionally, the existing workflow to quench the reaction was modified to eliminate the need for sonication-based cell lysis and additional sample preparation prior to MS analysis.

A structure-activity relationship of cathepsin-mediated release of model amine-containing payloads from cleavage linker conjugates is described in Chapter 3. The tetrapeptide Gly-Gly-Phe-Gly was coupled with aromatic, aliphatic, and benzylic amines to determine cleavage rates using cathepsin B. Historically, anilines were shown to be the only class of amines that could be

efficiently released from peptide linkers. It was discovered that scaffolds based on substituted 2-pyridyl methyl amines can be released in the presence of endolysosomal peptidases. These findings could be utilized to construct a new generation of ADC therapeutics.

Increased peptide spectrum matches (PSMs) and improved ETD efficiency were achieved by applying the supercharging reagent *m*-NBA to peptic digests as discussed in Chapter 4. To localize deuterium uptake, gas-phase fragmentation conditions, ETD/ECD, that do not cause scrambling are needed. The caveat of electron-based fragmentation is the need for higher charge state precursors for efficient fragmentation. *m*-NBA was added post chromatographic separation to boost the average charge state to meet this requirement and demonstrated the added benefit of increasing the amount of PSMs and unique peptides identified using HCD.

5.2 Future Directions

5.2.1 Continuous Droplet Generation

While the time to complete droplet-MS is drastically lower compared to conventional LC-MS/MS methods, there is a rate limiting step of disconnecting the syringe once it is full of droplets and reconnecting it for infusion into the mass spectrometer. A potential solution would be to incorporate a system that allows for continuous and simultaneous droplet generation and infusion (Figure 5-1). This could be achieved by having two syringes, one for droplet generation and one for infusion, connected via valves. More specifically, while one syringe system is generating droplets, the other can be infusing droplets for analysis. While this is possible to achieve using one eight-port switch valve, there is a concern for droplet stability as it passes through the rotor. Non-surfactant stabilized droplets can split into smaller droplets when flowed over different materials (i.e., PEEK, Valcon H, stainless steel). Split droplets are problematic since they will not generate

good peak shapes as sample infusion is disrupted. To preserve droplet stability, a whole Teflon valve can be made that does not induce any pressure changes upon switching¹⁶⁵ (**Error! Reference source not found.**). Applying these two designs would enable fully automated droplet-MS screening from up to eight 384-well plates before human intervention to swap out plates⁴⁶.

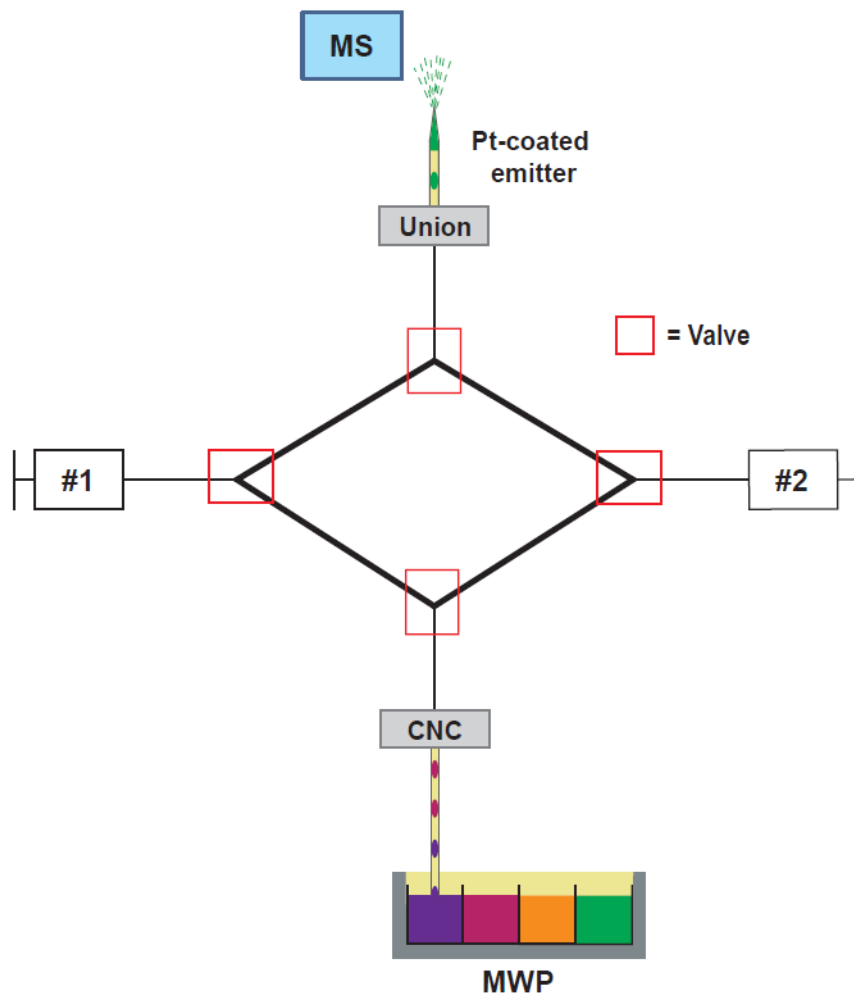


Figure 5-1 Schematic representation of continuous and simultaneous droplet generation and infusion using valves. Valves would be programmed to switch so that syringe #1 infuses droplets to the MS while syringe #2 generates droplets. Once syringe #1 empty and syringe #2 full, valves would switch.

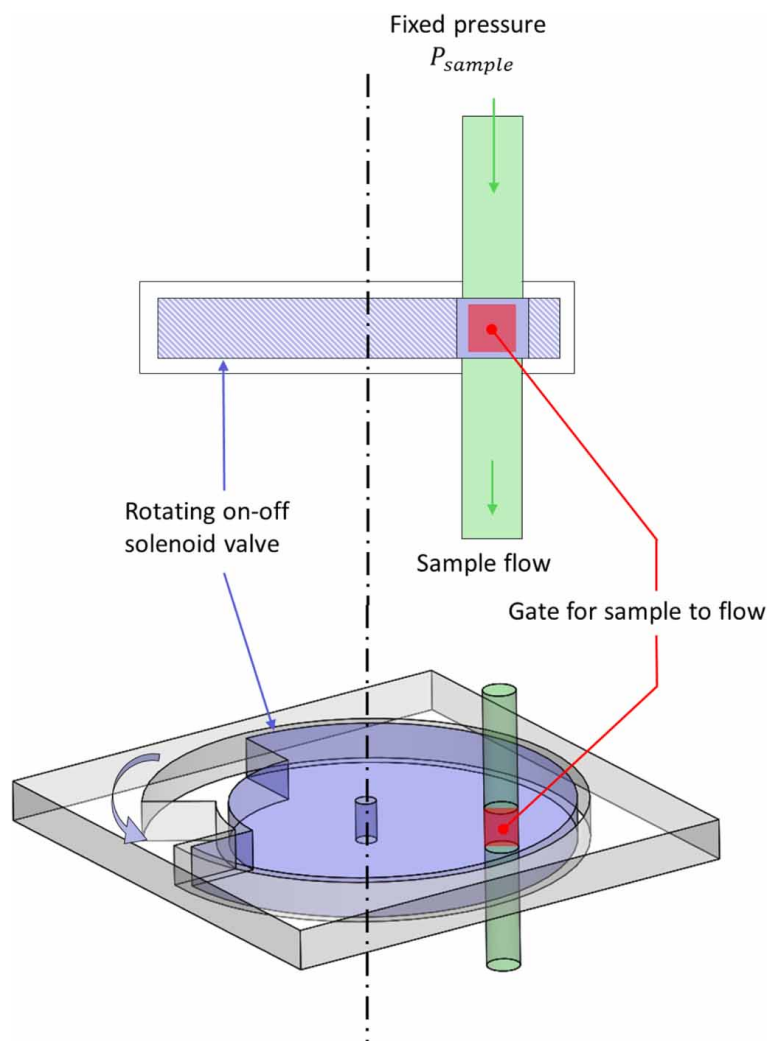


Figure 5-2 Design of valve for handling droplets without disrupting droplet stability or inducing carryover^{165,166}. Dashed line indicates axis of rotation of the lavender piece.

5.2.2 Determining Efficient Cathepsin-Mediated Release *in vivo*

In the study described in Chapter 3, purified cathepsins were used to cleave linker-payload compounds rather than observing cleavage of conjugated linker-payload after cellular-uptake. While the outcome of this study indicate that a wider variety of amine substrates can be used as payloads, ultimately these results are only preliminary and cannot be directly translated to how cleavage will occur *in vivo*. Due to the relatively large size of the antibody (~150 kDa) compared

to the linker-payload (< 1kDa), the rate at which either will enter a tumor cell will differ thus impacting cleavage efficiency^{45,139}.

While multiple cathepsins were used as well as rat liver tritosomes, ultimately there are hundreds of other proteases present in the lysosomal environment that can contribute to breakdown of the ADC^{149,167}. Though no adducts (Gly-payload, Phe-Gly-payload, etc.), were observed in our study it is known that cathepsin B can generate these adducts^{139,140}. It is possible that these adducts could be more easily identified using a targeted screening method like a SRM rather than the untargeted profile approach used to ensure detected adducts are not caused by in-source fragmentation.

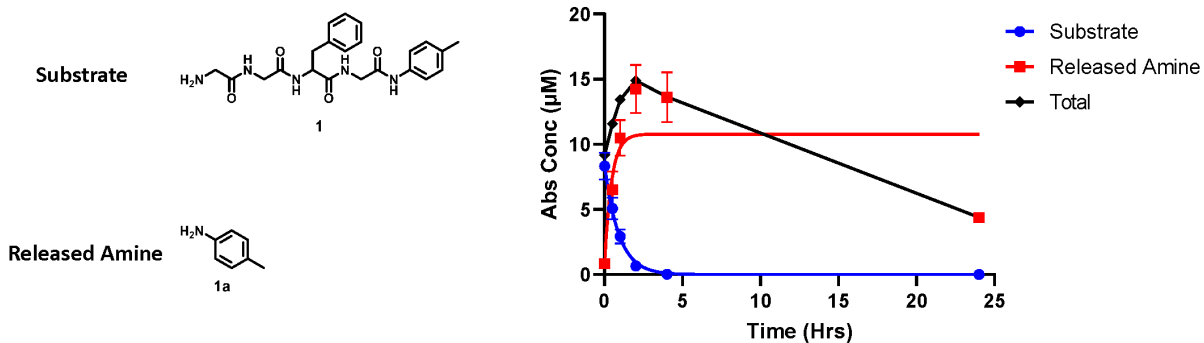
5.2.3 Supercharging Automated HDX for Ion Mobility-MS

In Chapter 4, *m*-NBA was applied to peptic digests of antibodies to improve electron-based fragmentation efficiency as well as increase total PSMs. The setup used did not incorporate temperature control necessary for minimizing back exchange nor online pepsin digestion. Using a fully automated HDX platform, LEAP HDX PAL coupled to an Agilent IM-ECD-QTOF would allow for reproducible timing and precise temperature control. Additionally, applying ion mobility could add an additional dimension of separation to better resolve co-eluting peptides. The Agilent 6560 is equipped with an e-MSion ExD cell that allows for ECD in a non-FT-ICR instrument allowing for tandem MS without scrambling.

Appendix

Supporting data for LC-MS curves and stability data in Chapter 3

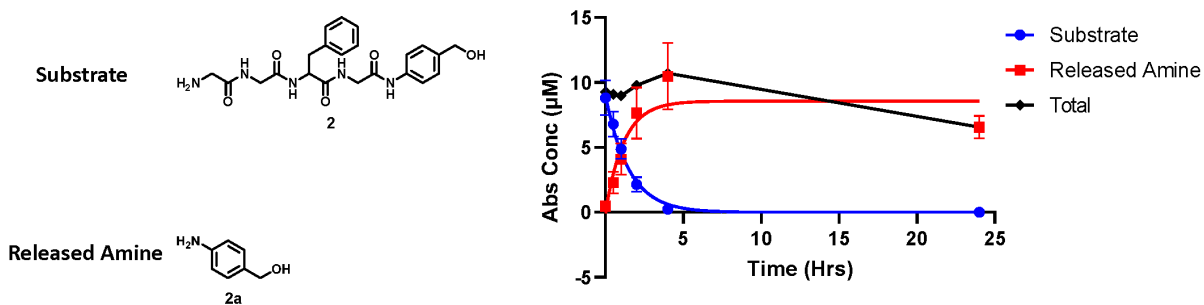
Below are the compiled curves for each substrate screened for half-life determination in addition to buffer stability data for substrate and released amine. Each data point collected in triplicate. Compounds courtesy of Angela Fan and Dr. Natalia Chernyak.



Cathepsin B Kinetics	T $\frac{1}{2}$ (hrs)	95% CI of t $\frac{1}{2}$ (hrs)
	0.640 hrs	[0.547 – 0.752]

Analyte	Condition	24 hrs Stability (%)
1	pH 5.0 Buffer Control	92
1a	pH 5.0 Buffer Control	35

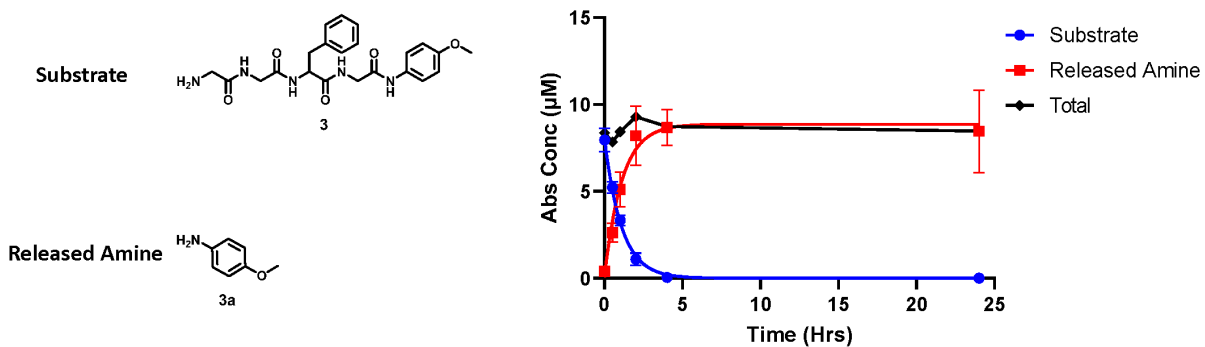
1



Cathepsin B Kinetics	T $\frac{1}{2}$ (hrs)	95% CI of t $\frac{1}{2}$ (hrs)
	1.04 hrs	[0.854 – 1.27]

Analyte	Condition	24 hrs Stability (%)
2	pH 5.0 Buffer Control	84
2a	pH 5.0 Buffer Control	35

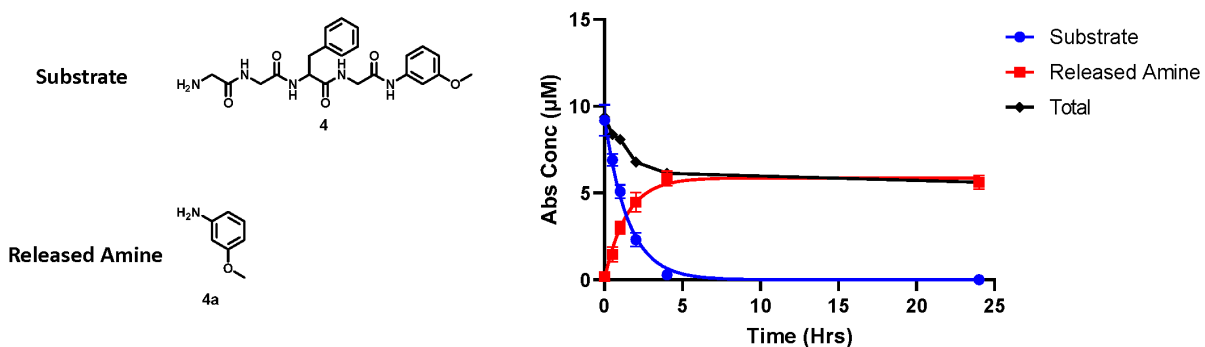
2



Cathepsin B Kinetics	T $\frac{1}{2}$ (hrs)	95% CI of t $\frac{1}{2}$ (hrs)
	0.758 hrs	[0.682 – 0.846]

Analyte	Condition	24 hrs Stability (%)
3	pH 5.0 Buffer Control	101
3a	pH 5.0 Buffer Control	100

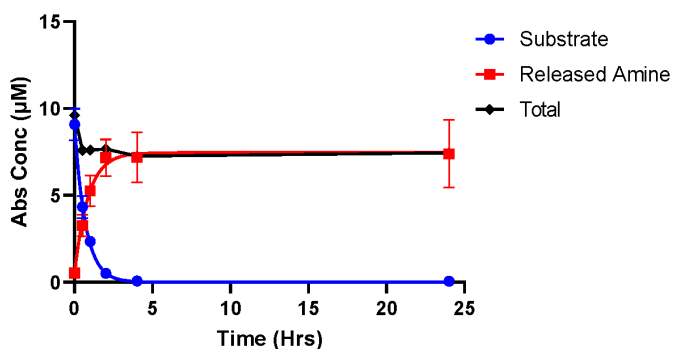
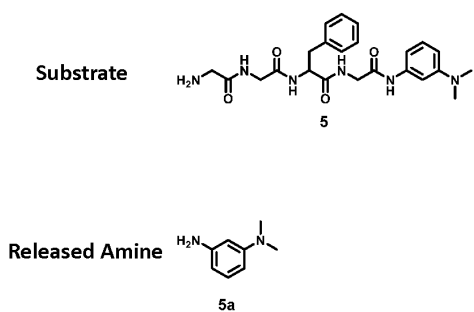
3



Cathepsin B Kinetics	T $\frac{1}{2}$ (hrs)	95% CI of t $\frac{1}{2}$ (hrs)
	1.04 hrs	[0.923 – 1.18]

Analyte	Condition	24 hrs Stability (%)
4	pH 5.0 Buffer Control	96
4a	pH 5.0 Buffer Control	90

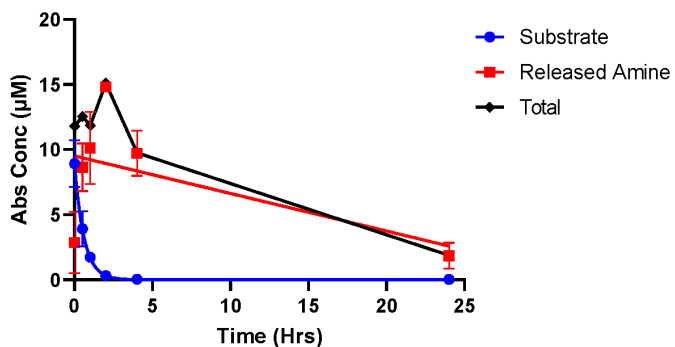
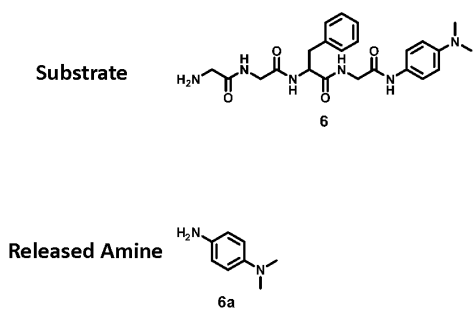
4



Cathepsin B Kinetics	T ½ (hrs)	95% CI of t ½ (hrs)
	0.491 hrs	[0.434 – 0.556]

Analyte	Condition	24 hrs Stability (%)
5	pH 5.0 Buffer Control	97
5a	pH 5.0 Buffer Control	95

5

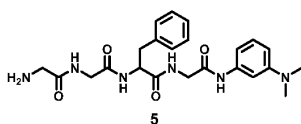


Cathepsin B Kinetics	T ½ (hrs)	95% CI of t ½ (hrs)
	0.420 hrs	[0.329 – 0.535]

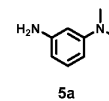
Analyte	Condition	24 hrs Stability (%)
6	pH 5.0 Buffer Control	92
6a	pH 5.0 Buffer Control	5

6

Substrate

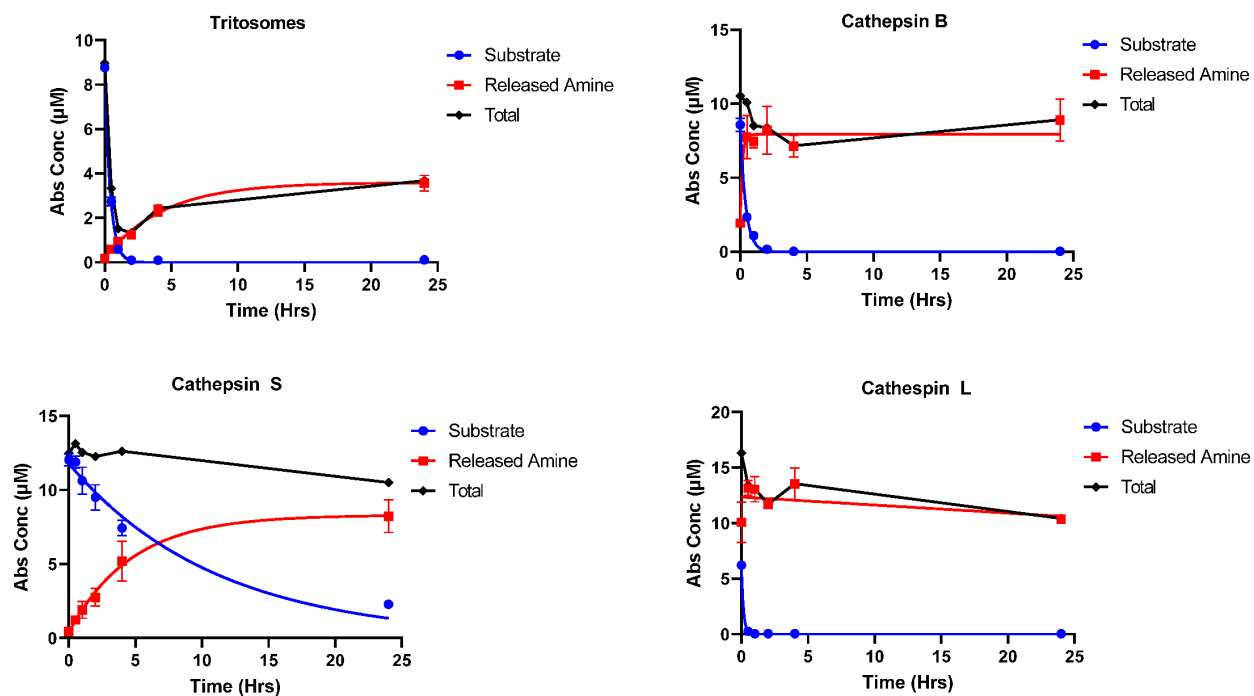


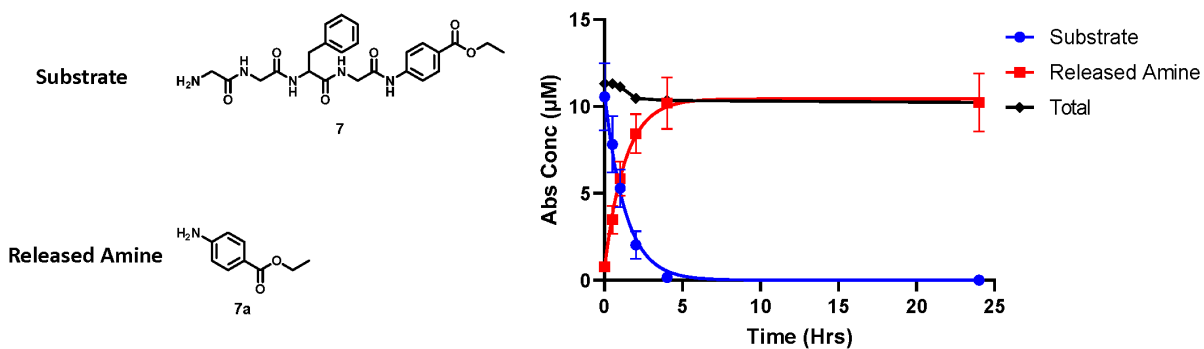
Released Amine



Cathepsin B Kinetics	T $\frac{1}{2}$ (hrs)	95% CI of t $\frac{1}{2}$ (hrs)
	0.286 hrs	[0.261 – 0.313]
Cathepsin L Kinetics	T $\frac{1}{2}$ (hrs)	95% CI of t $\frac{1}{2}$ (hrs)
	0.110 hrs	[0.100 – 0.120]
Cathepsin S Kinetics	T $\frac{1}{2}$ (hrs)	95% CI of t $\frac{1}{2}$ (hrs)
	4.37 hrs	[3.65 – N/A]
Tritosome Kinetics	T $\frac{1}{2}$ (hrs)	95% CI of t $\frac{1}{2}$ (hrs)
	0.286 hrs	[0.272 – 0.302]
Analyte	Condition	24 hrs Stability (%)
5	pH 5.0 Buffer Control	97
5a	pH 5.0 Buffer Control	95

Multi enzyme 5



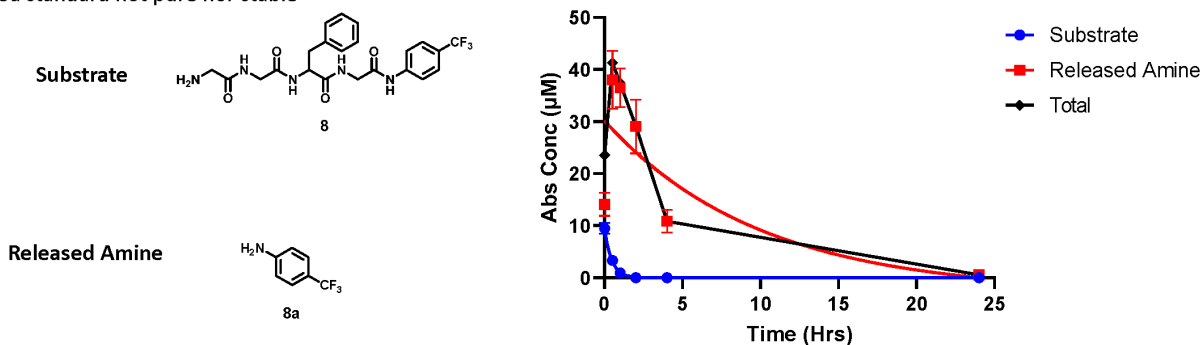


Cathepsin B Kinetics	T ½ (hrs)	95% CI of t ½ (hrs)
	0.919 hrs	[0.726 – 1.18]

Analyte	Condition	24 hrs Stability (%)
7	pH 5.0 Buffer Control	98
7a	pH 5.0 Buffer Control	97

7

*8a standard not pure nor stable

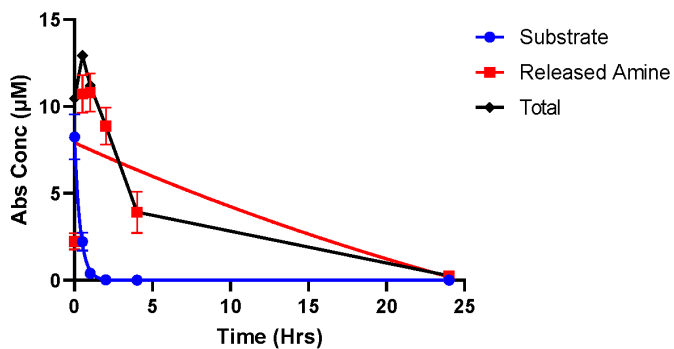
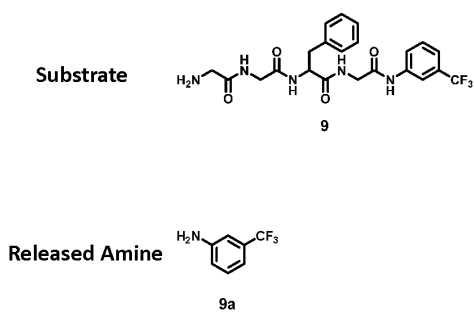


Cathepsin B Kinetics	T ½ (hrs)	95% CI of t ½ (hrs)
	0.316 hrs	[0.274 – 0.363]

Analyte	Condition	24 hrs Stability (%)
8	pH 5.0 Buffer Control	93
8a	pH 5.0 Buffer Control	1

8

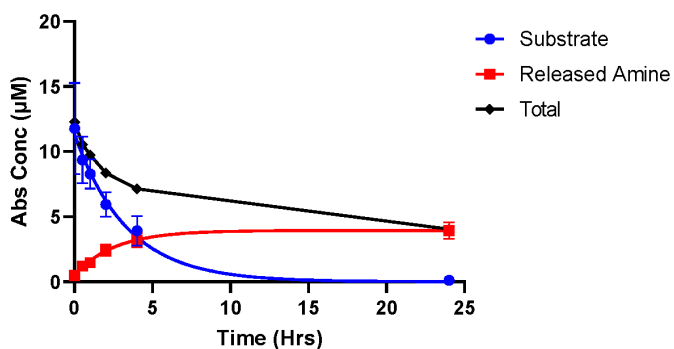
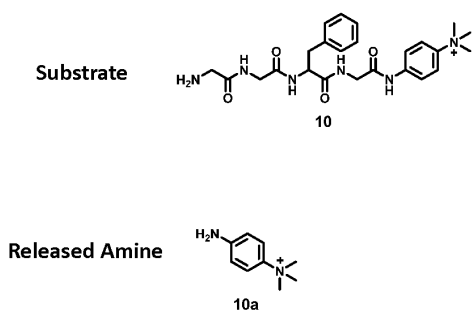
*9a not stable over time



Cathepsin B Kinetics	T ½ (hrs)	95% CI of t ½ (hrs)
	0.256 hrs	[0.209 – 0.309]

Analyte	Condition	24 hrs Stability (%)
9	pH 5.0 Buffer Control	89
9a	pH 5.0 Buffer Control	3

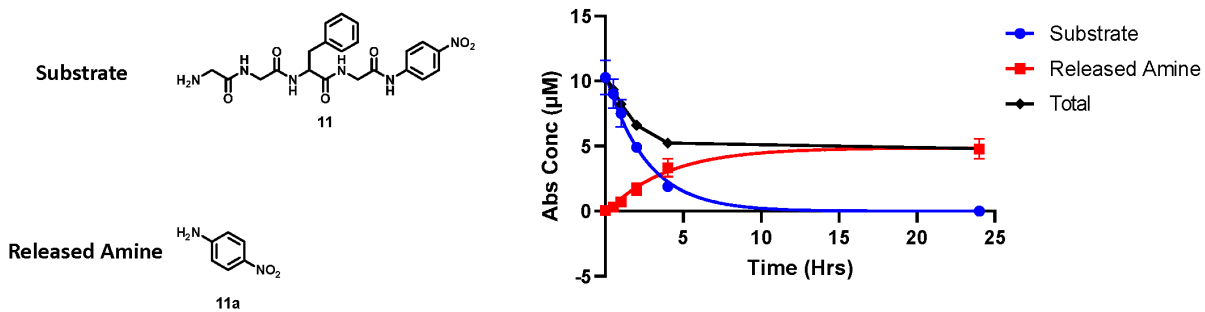
9



Cathepsin B Kinetics	T ½ (hrs)	95% CI of t ½ (hrs)
	2.32 hrs	[1.59 – 3.70]

Analyte	Condition	24 hrs Stability (%)
10	pH 5.0 Buffer Control	85
10a	pH 5.0 Buffer Control	98

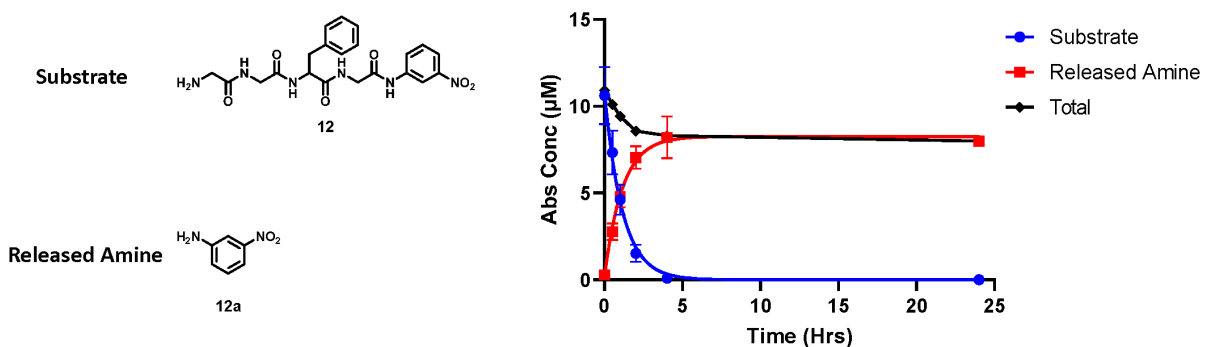
10



Cathepsin B Kinetics	T ½ (hrs)	95% CI of t ½ (hrs)
	1.80 hrs	[1.50 – 2.19]

Analyte	Condition	24 hrs Stability (%)
11	pH 5.0 Buffer Control	93
11a	pH 5.0 Buffer Control	108

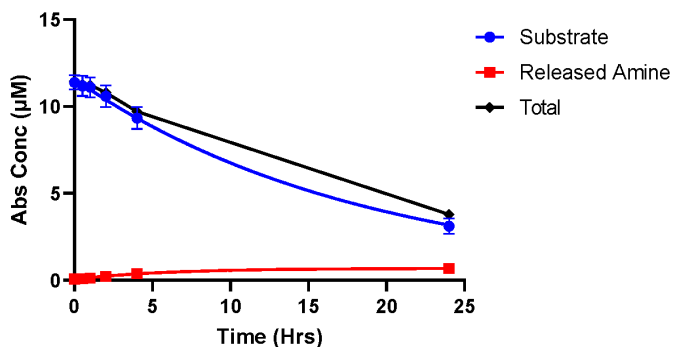
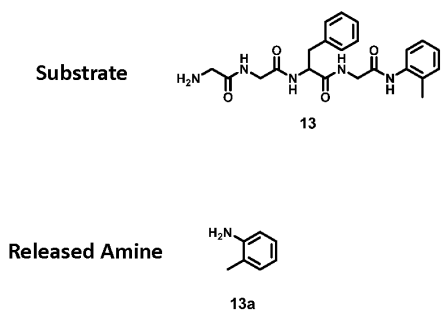
11



Cathepsin B Kinetics	T ½ (hrs)	95% CI of t ½ (hrs)
	0.793 hrs	[0.654 – 0.971]

Analyte	Condition	24 hrs Stability (%)
12	pH 5.0 Buffer Control	96
12a	pH 5.0 Buffer Control	100

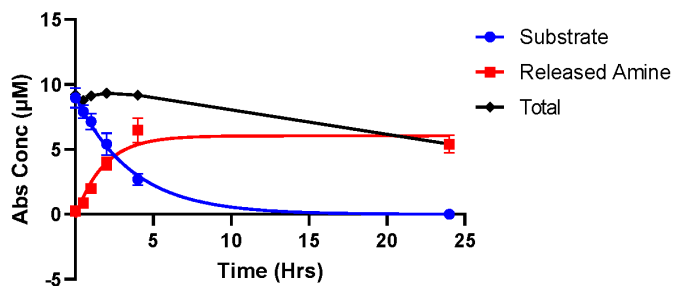
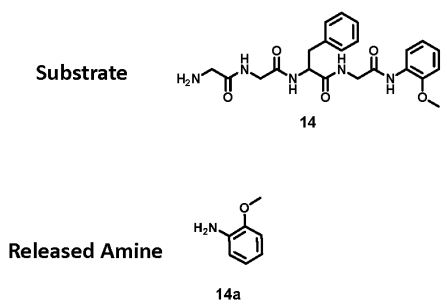
12



Cathepsin B Kinetics	T ½ (hrs)	95% CI of t ½ (hrs)
	12.9 hrs	[11.1 – 14.8]

Analyte	Condition	24 hrs Stability (%)
13	pH 5.0 Buffer Control	95
13a	pH 5.0 Buffer Control	23

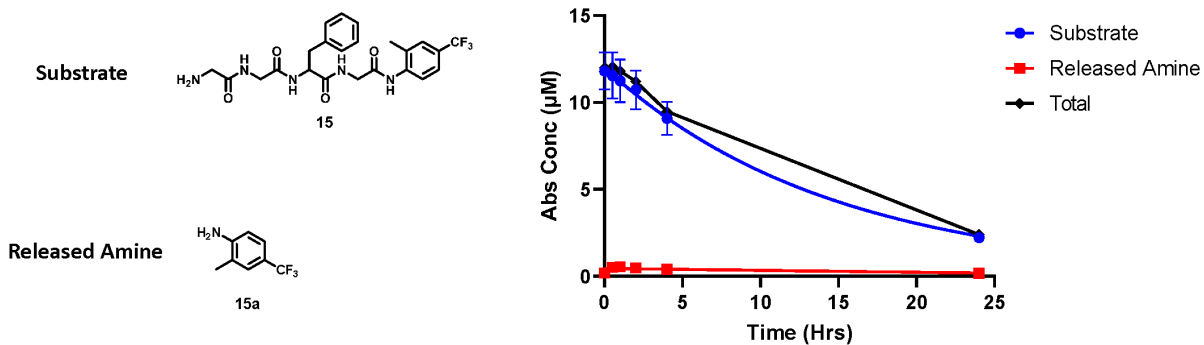
13



Cathepsin B Kinetics	T ½ (hrs)	95% CI of t ½ (hrs)
	2.49 hrs	[2.11 – 2.97]

Analyte	Condition	24 hrs Stability (%)
14	pH 5.0 Buffer Control	89
14a	pH 5.0 Buffer Control	83

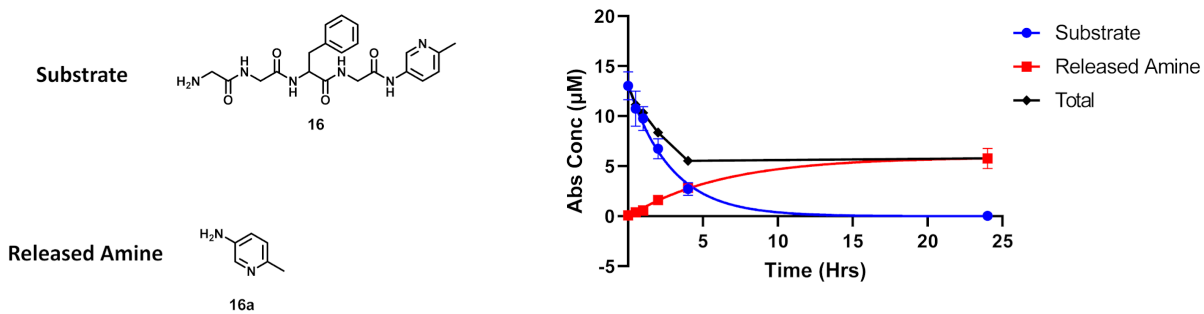
14



Cathepsin B Kinetics	T $\frac{1}{2}$ (hrs)	95% CI of t $\frac{1}{2}$ (hrs)
	10.1 hrs	[7.70 – 13.1]

Analyte	Condition	24 hrs Stability (%)
15	pH 5.0 Buffer Control	92
15a	pH 5.0 Buffer Control	0

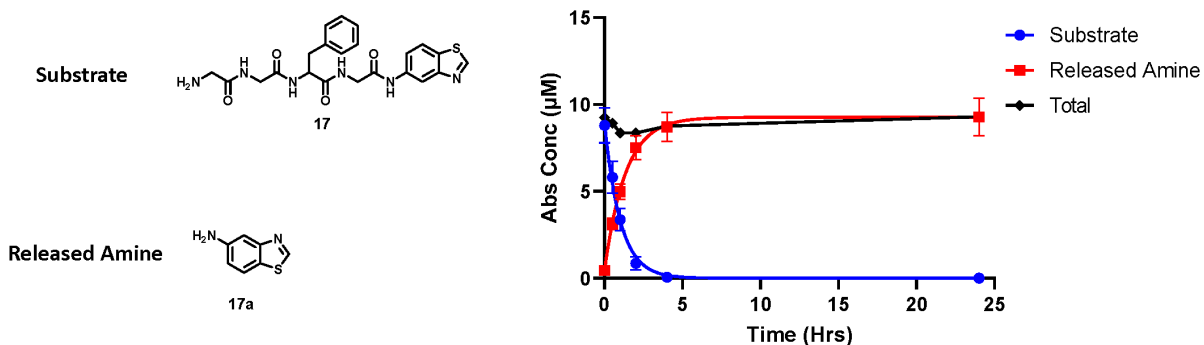
15



Cathepsin B Kinetics	T $\frac{1}{2}$ (hrs)	95% CI of t $\frac{1}{2}$ (hrs)
	1.97 hrs	[1.60 – 2.46]

Analyte	Condition	24 hrs Stability (%)
16	pH 5.0 Buffer Control	105
16a	pH 5.0 Buffer Control	102

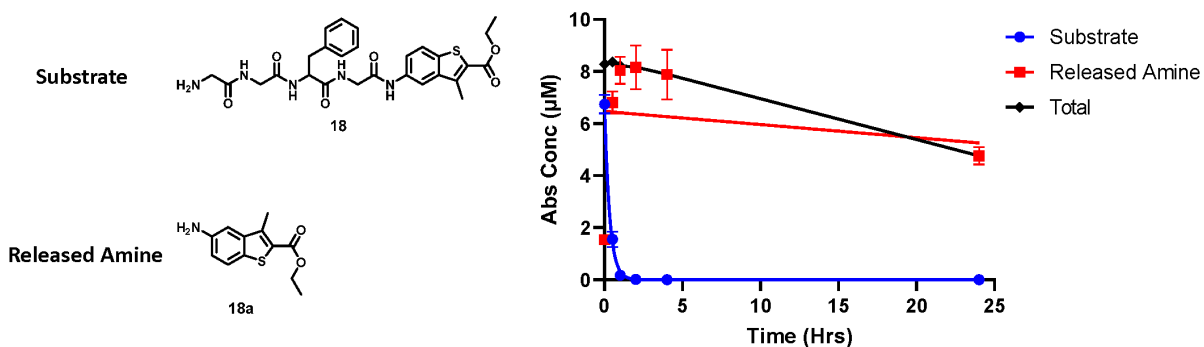
16



Cathepsin B Kinetics	T $\frac{1}{2}$ (hrs)	95% CI of t $\frac{1}{2}$ (hrs)
	0.701 hrs	[0.596 – 0.831]

Analyte	Condition	24 hrs Stability (%)
17	pH 5.0 Buffer Control	94
17a	pH 5.0 Buffer Control	100

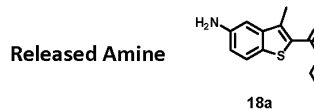
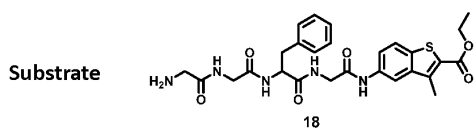
17



Cathepsin B Kinetics	T $\frac{1}{2}$ (hrs)	95% CI of t $\frac{1}{2}$ (hrs)
	0.229 hrs	[0.209 – 0.250]

Analyte	Condition	24 hrs Stability (%)
18	pH 5.0 Buffer Control	94
18a	pH 5.0 Buffer Control	63

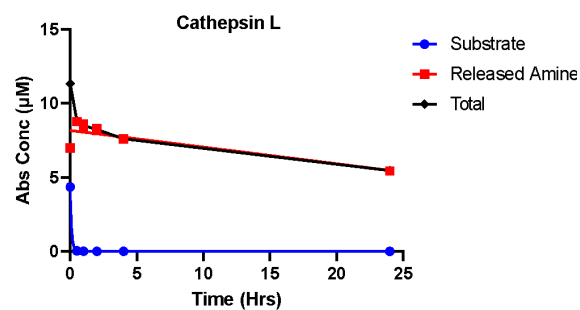
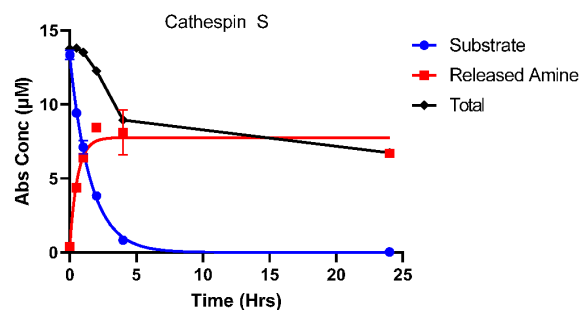
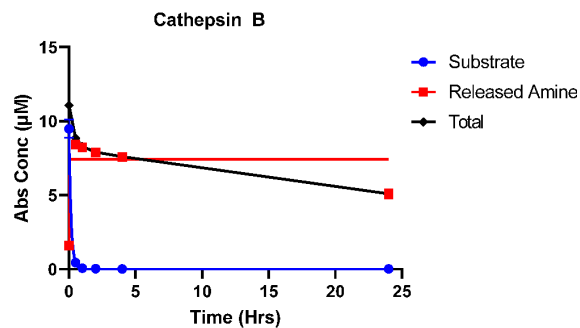
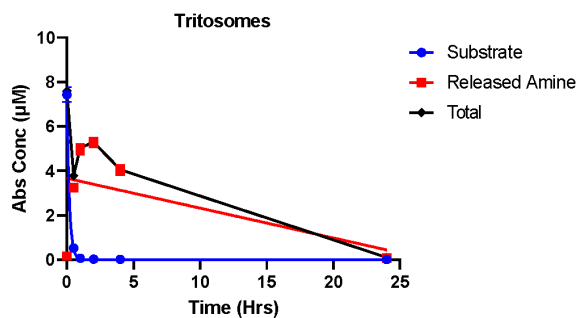
18

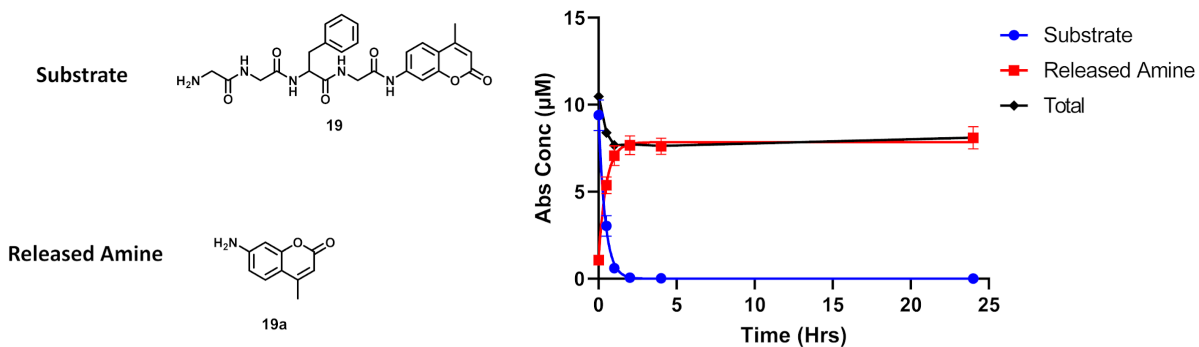


Cathepsin B Kinetics	T ½ (hrs)	95% CI of t ½ (hrs)
	0.114 hrs	[0.0872 – 0.135]
Cathepsin L Kinetics	T ½ (hrs)	95% CI of t ½ (hrs)
	0.0733 hrs	[0.0512 – 0.0845]
Cathepsin S Kinetics	T ½ (hrs)	95% CI of t ½ (hrs)
	1.09 hrs	[1.02 – 1.17]
Tritosome Kinetics	T ½ (hrs)	95% CI of t ½ (hrs)
	0.132 hrs	[0.118 – 0.146]

Analyte	Condition	24 hrs Stability (%)
18	pH 5.0 Buffer Control	94
18a	pH 5.0 Buffer Control	63

Multi enzyme 18

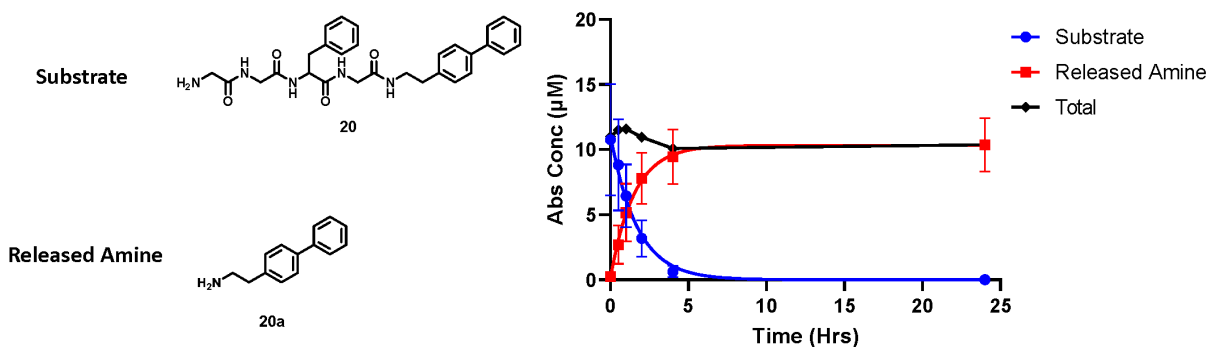




Cathepsin B Kinetics	T $\frac{1}{2}$ (hrs)	95% CI of t $\frac{1}{2}$ (hrs)
	0.291 hrs	[0.256 – 0.329]

Analyte	Condition	24 hrs Stability (%)
19	pH 5.0 Buffer Control	98
19a	pH 5.0 Buffer Control	102

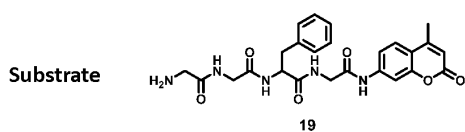
19



Cathepsin B Kinetics	T $\frac{1}{2}$ (hrs)	95% CI of t $\frac{1}{2}$ (hrs)
	1.18 hrs	[0.737 – 2.03]

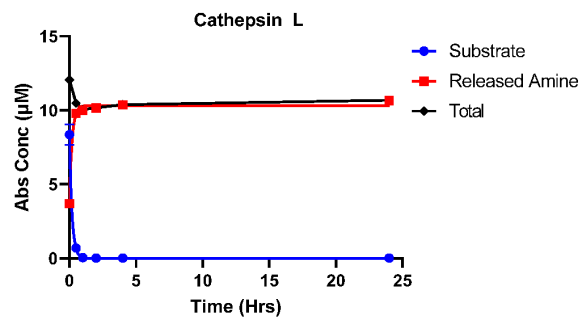
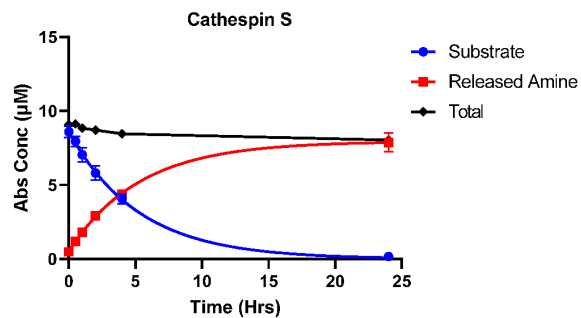
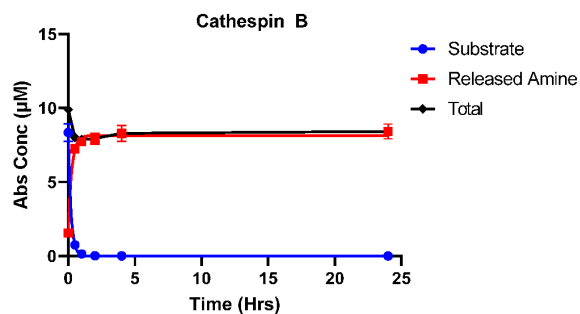
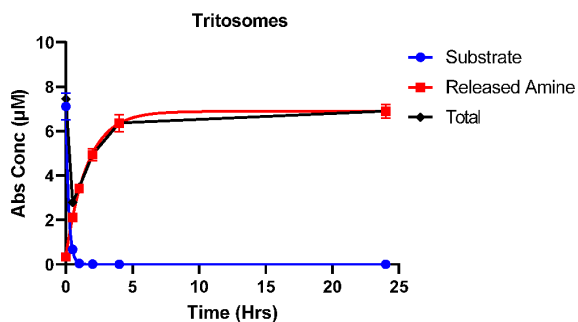
Analyte	Condition	24 hrs Stability (%)
20	pH 5.0 Buffer Control	99
20a	pH 5.0 Buffer Control	95

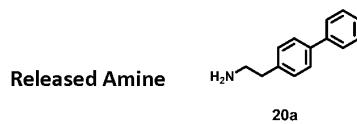
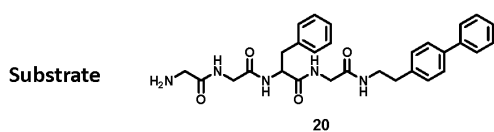
20



Cathepsin B Kinetics	T ½ (hrs)	95% CI of t ½ (hrs)
	0.146 hrs	[0.124 – 0.166]
Cathepsin L Kinetics	T ½ (hrs)	95% CI of t ½ (hrs)
	0.139 hrs	[0.113 – 0.162]
Cathepsin S Kinetics	T ½ (hrs)	95% CI of t ½ (hrs)
	3.56 hrs	[3.18 – 4.24]
Tritosome Kinetics	T ½ (hrs)	95% CI of t ½ (hrs)
	0.147 hrs	[0.122 – 0.171]
Analyte	Condition	24 hrs Stability (%)
19	pH 5.0 Buffer Control	97
19a	pH 5.0 Buffer Control	95

Multi enzyme 19

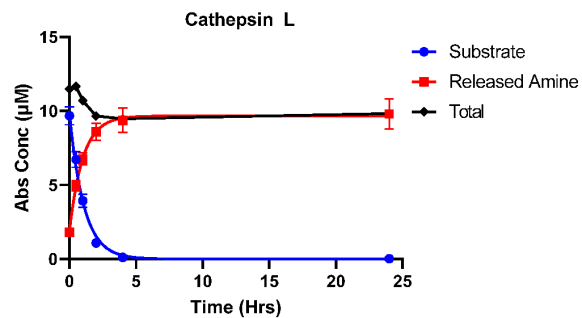
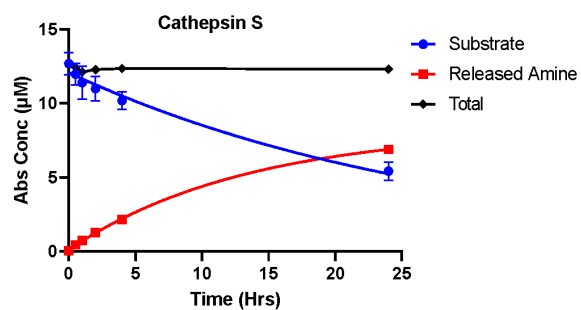
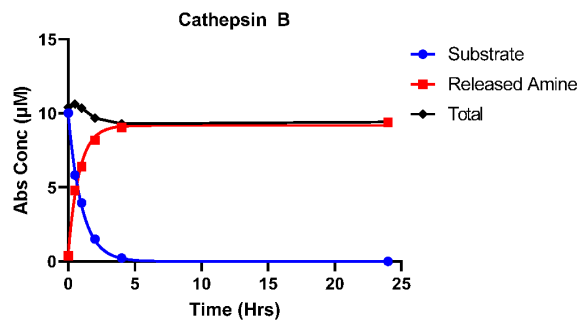
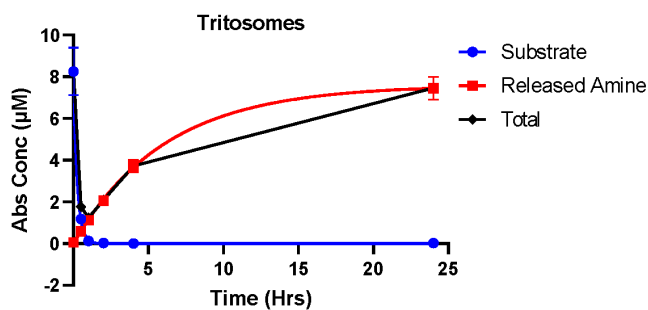


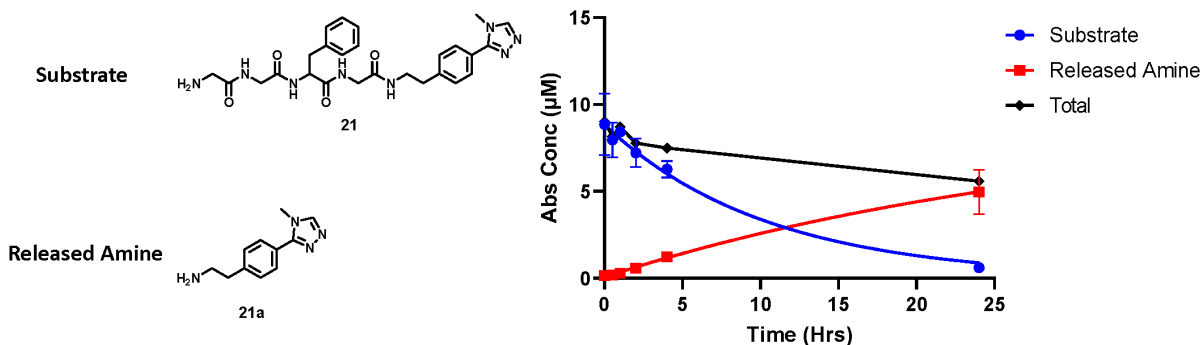


Cathepsin B Kinetics	T ½ (hrs)	95% CI of t ½ (hrs)
	0.718 hrs	[0.682 – 0.755]
Cathepsin L Kinetics	T ½ (hrs)	95% CI of t ½ (hrs)
	0.748 hrs	[0.668 – 0.839]
Cathepsin S Kinetics	T ½ (hrs)	95% CI of t ½ (hrs)
	7.69 hrs	[6.01 – N/A]
Tritosome Kinetics	T ½ (hrs)	95% CI of t ½ (hrs)
	0.177 hrs	[0.139 – 0.215]

Analyte	Condition	24 hrs Stability (%)
20	pH 5.0 Buffer Control	99
20a	pH 5.0 Buffer Control	95

Multi enzyme 20

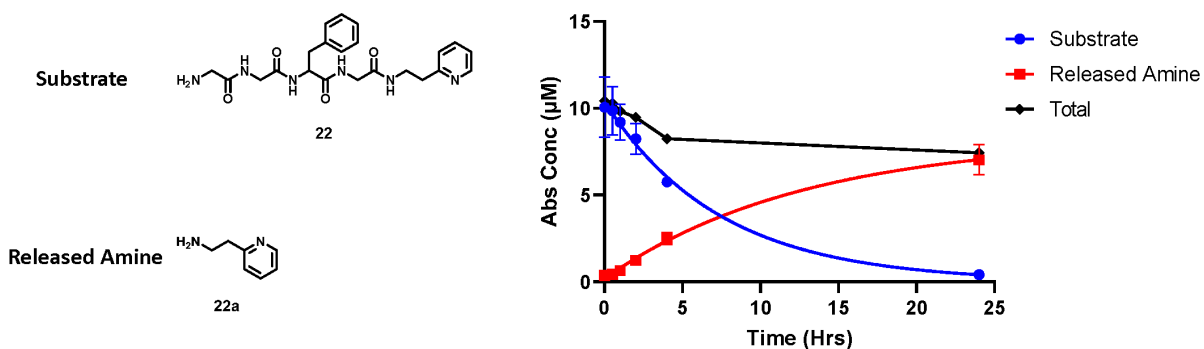




Cathepsin B Kinetics	T $\frac{1}{2}$ (hrs)	95% CI of t $\frac{1}{2}$ (hrs)
	7.23 hrs	[5.12 – 10.2]

Analyte	Condition	24 hrs Stability (%)
21	pH 5.0 Buffer Control	98
21a	pH 5.0 Buffer Control	95

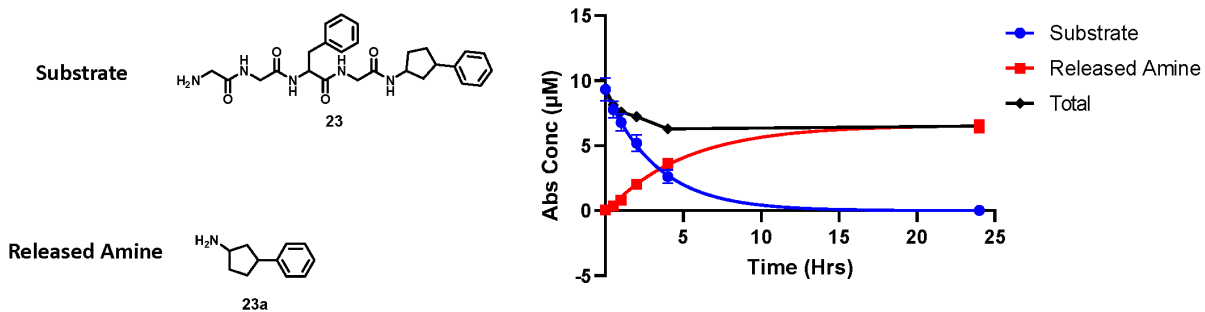
21



Cathepsin B Kinetics	T $\frac{1}{2}$ (hrs)	95% CI of t $\frac{1}{2}$ (hrs)
	5.13 hrs	[3.71 – 7.39]

Analyte	Condition	24 hrs Stability (%)
22	pH 5.0 Buffer Control	87
22a	pH 5.0 Buffer Control	86

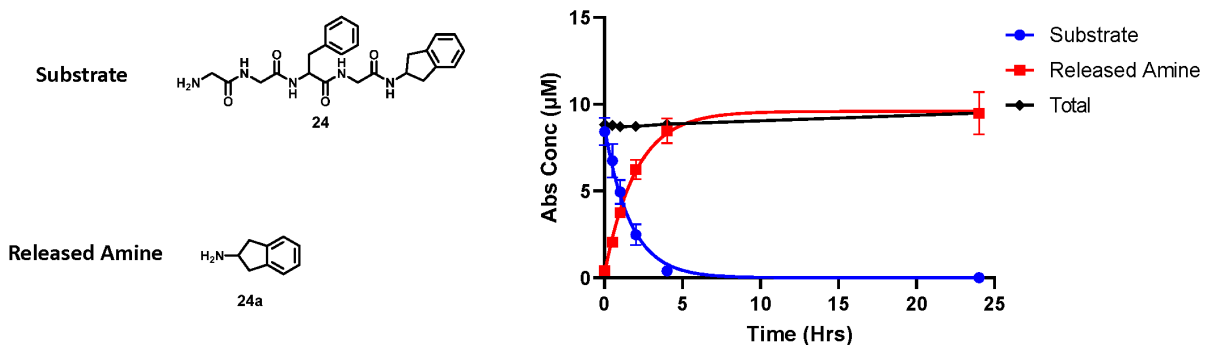
22



Cathepsin B Kinetics	T $\frac{1}{2}$ (hrs)	95% CI of t $\frac{1}{2}$ (hrs)
	2.26 hrs	[1.93 – 2.69]

Analyte	Condition	24 hrs Stability (%)
23	pH 5.0 Buffer Control	102
23a	pH 5.0 Buffer Control	99

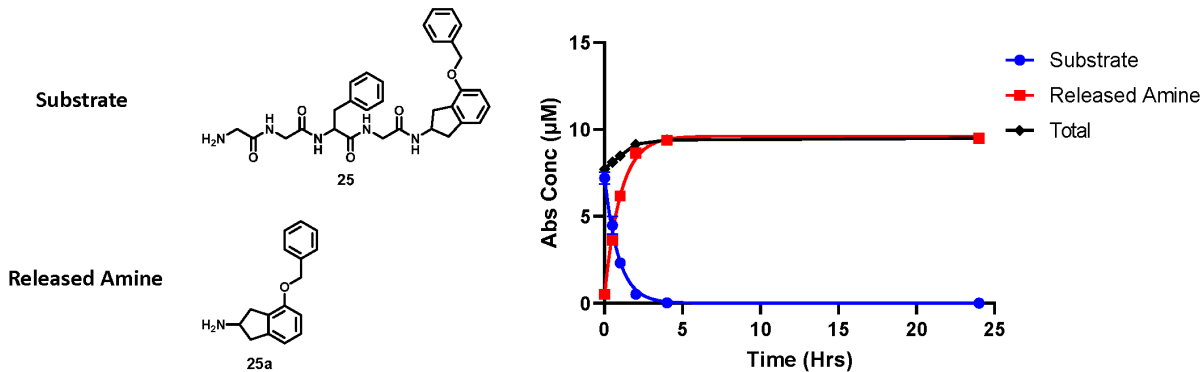
23



Cathepsin B Kinetics	T $\frac{1}{2}$ (hrs)	95% CI of t $\frac{1}{2}$ (hrs)
	1.15 hrs	[0.971 – 1.38]

Analyte	Condition	24 hrs Stability (%)
24	pH 5.0 Buffer Control	97
24a	pH 5.0 Buffer Control	107

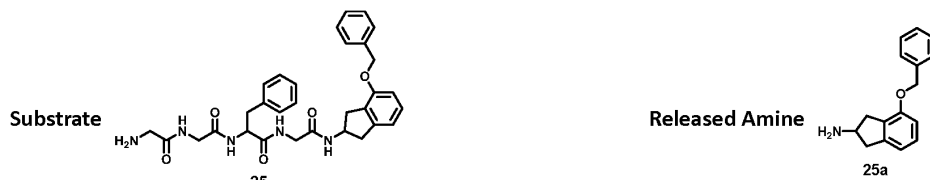
24



Cathepsin B Kinetics	T ½ (hrs)	95% CI of t ½ (hrs)
	0.619 hrs	[0.560 – 0.686]

Analyte	Condition	24 hrs Stability (%)
25	pH 5.0 Buffer Control	95
25a	pH 5.0 Buffer Control	100

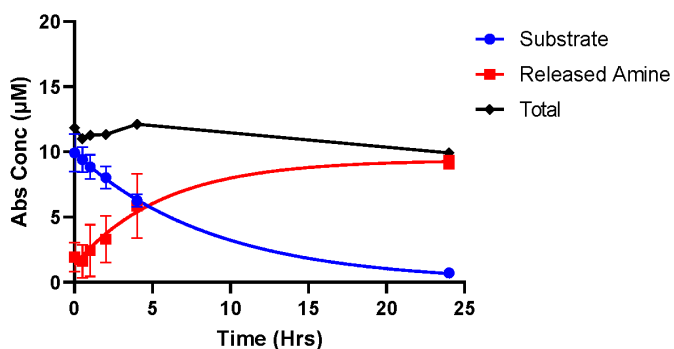
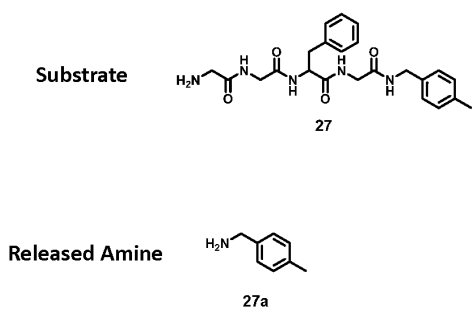
25



Cathepsin B Kinetics	T ½ (hrs)	95% CI of t ½ (hrs)
	0.667 hrs	[0.521 – 0.864]
Cathepsin L Kinetics	T ½ (hrs)	95% CI of t ½ (hrs)
	0.144 hrs	[0.139 – 0.149]
Cathepsin S Kinetics	T ½ (hrs)	95% CI of t ½ (hrs)
	4.04 hrs	[3.18 – 6.77]
Tritosome Kinetics	T ½ (hrs)	95% CI of t ½ (hrs)
	0.102 hrs	[N/A – 0.151]

Analyte	Condition	24 hrs Stability (%)
25	pH 5.0 Buffer Control	95
25a	pH 5.0 Buffer Control	100

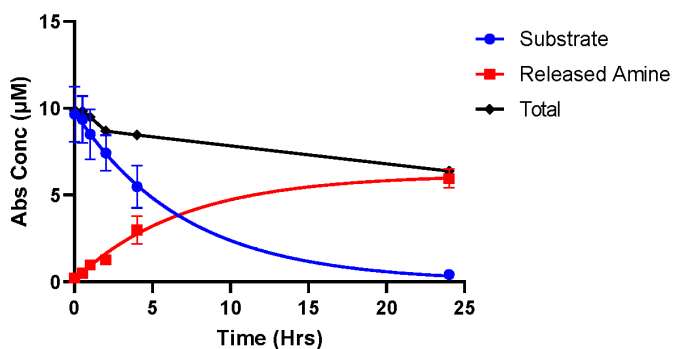
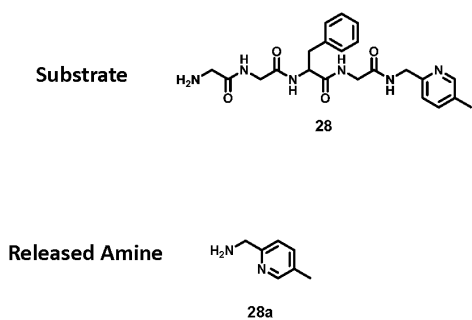
Multi enzyme 25



Cathepsin B Kinetics	T ½ (hrs)	95% CI of t ½ (hrs)
	6.15 hrs	[4.56 – 8.39]

Analyte	Condition	24 hrs Stability (%)
27	pH 5.0 Buffer Control	92
27a	pH 5.0 Buffer Control	93

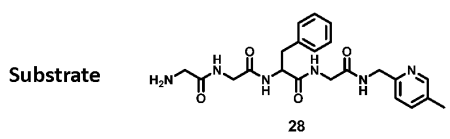
27



Cathepsin B Kinetics	T ½ (hrs)	95% CI of t ½ (hrs)
	4.89 hrs	[3.36 – 7.61]

Analyte	Condition	24 hrs Stability (%)
28	pH 5.0 Buffer Control	105
28a	pH 5.0 Buffer Control	93

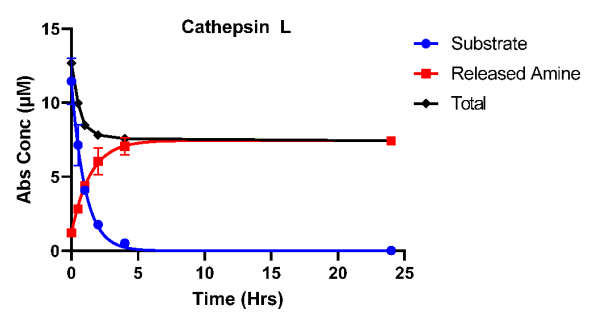
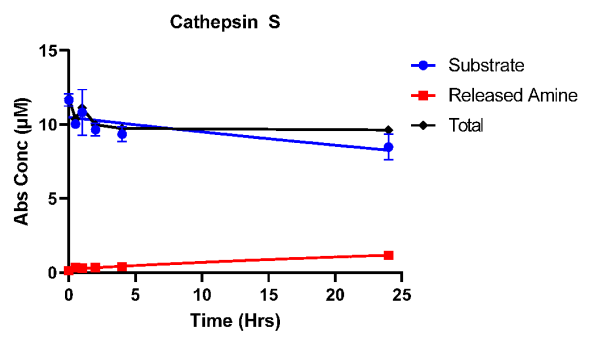
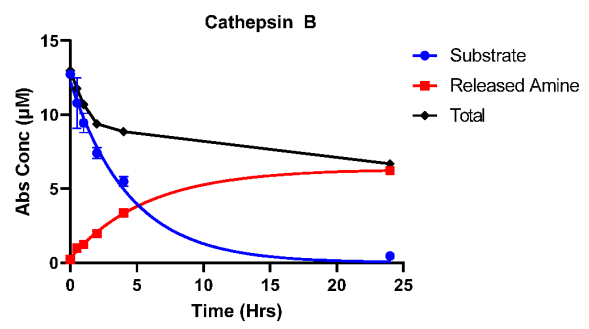
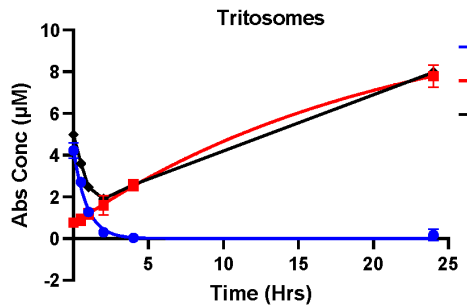
28

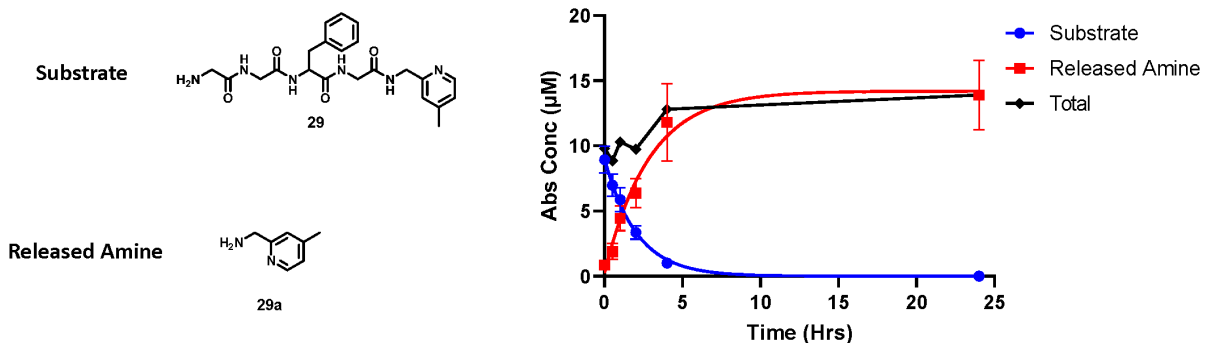


Cathepsin B Kinetics	T ½ (hrs)	95% CI of t ½ (hrs)
	3.08 hrs	[2.52 – 3.87]
Cathepsin L Kinetics	T ½ (hrs)	95% CI of t ½ (hrs)
	0.713 hrs	[0.600 – 0.854]
Cathepsin S Kinetics	T ½ (hrs)	95% CI of t ½ (hrs)
	No Cleavage	
Tritosome Kinetics	T ½ (hrs)	95% CI of t ½ (hrs)
	0.615 hrs	[0.535 – 0.710]

Analyte	Condition	24 hrs Stability (%)
28	pH 5.0 Buffer Control	82
28a	pH 5.0 Buffer Control	93

Multi enzyme 28

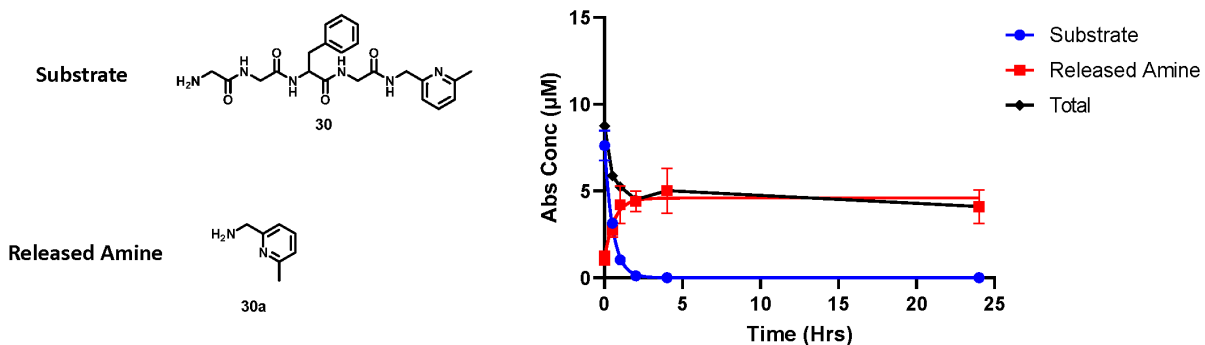




Cathepsin B Kinetics	T ½ (hrs)	95% CI of t ½ (hrs)
	1.41 hrs	[1.19 – 1.71]

Analyte	Condition	24 hrs Stability (%)
29	pH 5.0 Buffer Control	93
29a	pH 5.0 Buffer Control	99

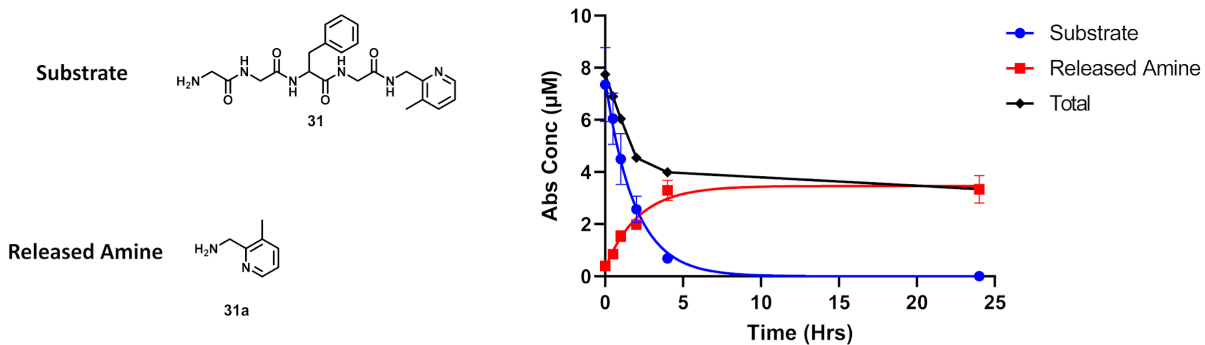
29



Cathepsin B Kinetics	T ½ (hrs)	95% CI of t ½ (hrs)
	0.371 hrs	[0.330 – 0.417]

Analyte	Condition	24 hrs Stability (%)
30	pH 5.0 Buffer Control	96
30a	pH 5.0 Buffer Control	91

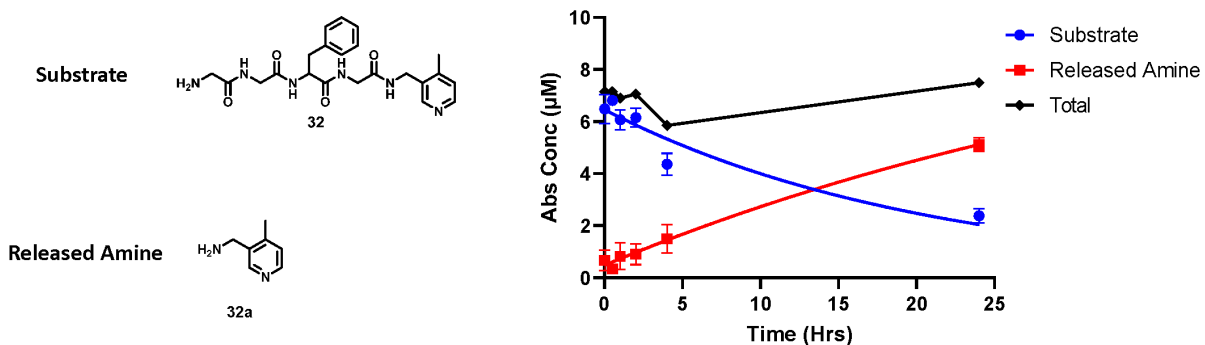
30



Cathepsin B Kinetics	T $\frac{1}{2}$ (hrs)	95% CI of t $\frac{1}{2}$ (hrs)
	1.31 hrs	[1.03 – 1.70]

Analyte	Condition	24 hrs Stability (%)
31	pH 5.0 Buffer Control	105
31a	pH 5.0 Buffer Control	100

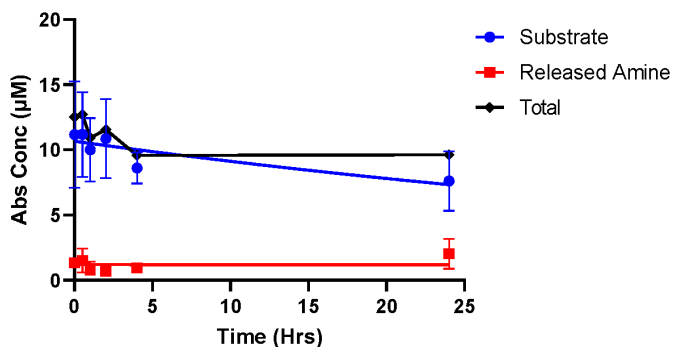
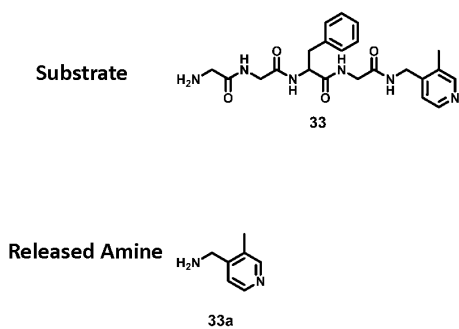
31



Cathepsin B Kinetics	T $\frac{1}{2}$ (hrs)	95% CI of t $\frac{1}{2}$ (hrs)
	14.5 hrs	[10.3 – 20.4]

Analyte	Condition	24 hrs Stability (%)
32	pH 5.0 Buffer Control	99
32a	pH 5.0 Buffer Control	97

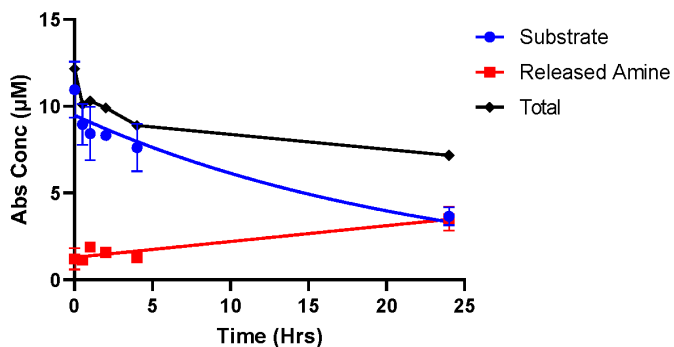
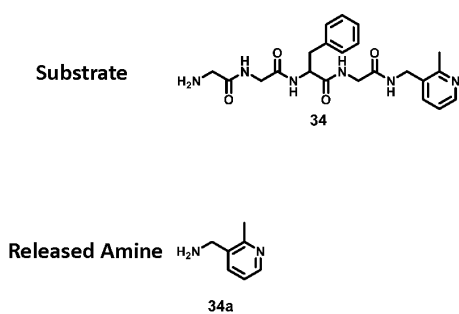
32



Cathepsin B Kinetics	T ½ (hrs)	95% CI of t ½ (hrs)
	no cleavage	

Analyte	Condition	24 hrs Stability (%)
33	pH 5.0 Buffer Control	95
33a	pH 5.0 Buffer Control	96

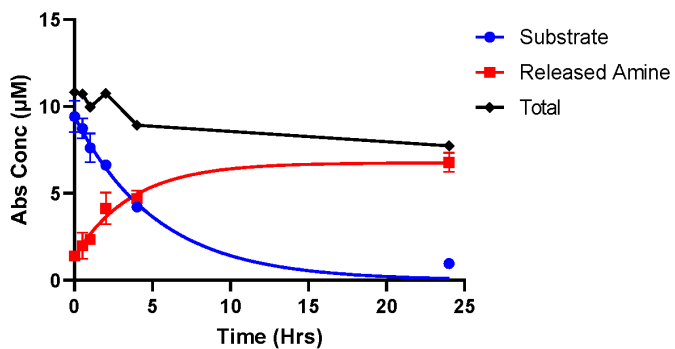
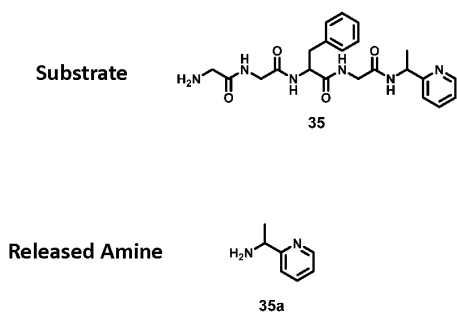
33



Cathepsin B Kinetics	T ½ (hrs)	95% CI of t ½ (hrs)
	15.9 hrs	[9.86 – 26.50]

Analyte	Condition	24 hrs Stability (%)
34	pH 5.0 Buffer Control	88
34a	pH 5.0 Buffer Control	99

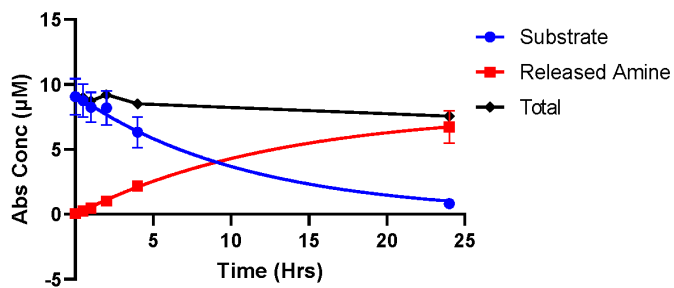
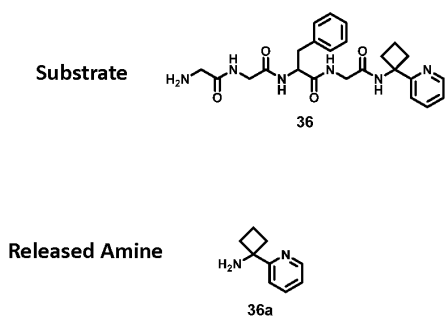
34



Cathepsin B Kinetics	T ½ (hrs)	95% CI of t ½ (hrs)
	3.65 hrs	[2.93 – 4.77]

Analyte	Condition	24 hrs Stability (%)
35	pH 5.0 Buffer Control	96
35a	pH 5.0 Buffer Control	96

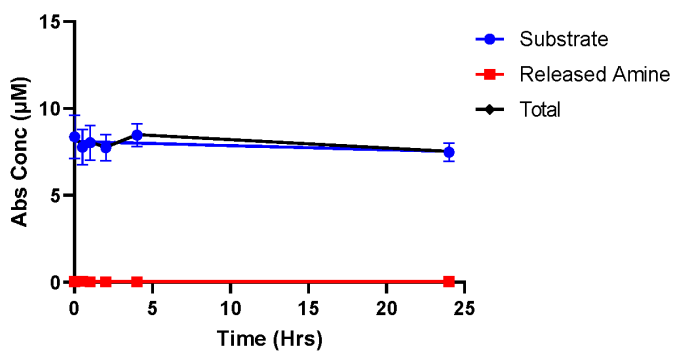
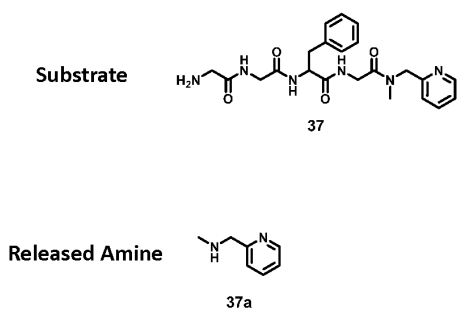
35



Cathepsin B Kinetics	T ½ (hrs)	95% CI of t ½ (hrs)
	7.57 hrs	[5.04 – 11.3]

Analyte	Condition	24 hrs Stability (%)
36	pH 5.0 Buffer Control	91
36a	pH 5.0 Buffer Control	86

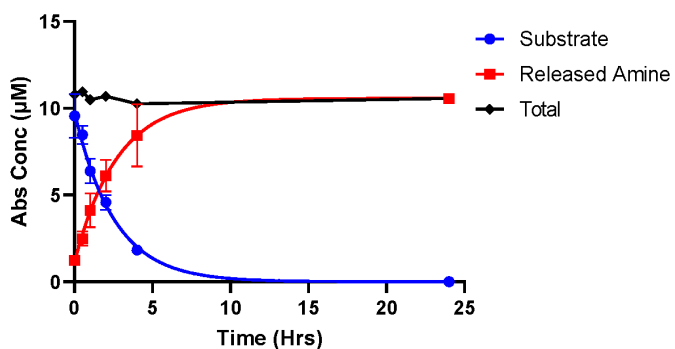
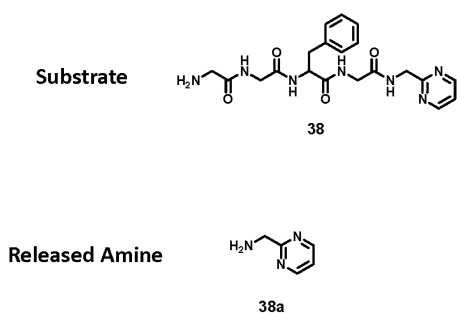
36



Cathepsin B Kinetics	T ½ (hrs)	95% CI of t ½ (hrs)
	No cleavage	

Analyte	Condition	24 hrs Stability (%)
37	pH 5.0 Buffer Control	96
37a	pH 5.0 Buffer Control	96

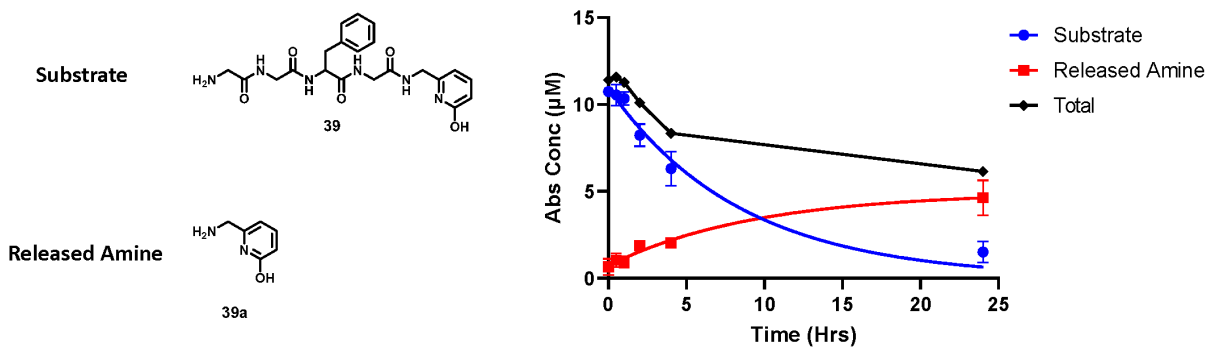
37



Cathepsin B Kinetics	T ½ (hrs)	95% CI of t ½ (hrs)
	1.75 hrs	[1.49 – 2.09]

Analyte	Condition	24 hrs Stability (%)
38	pH 5.0 Buffer Control	100
38a	pH 5.0 Buffer Control	111

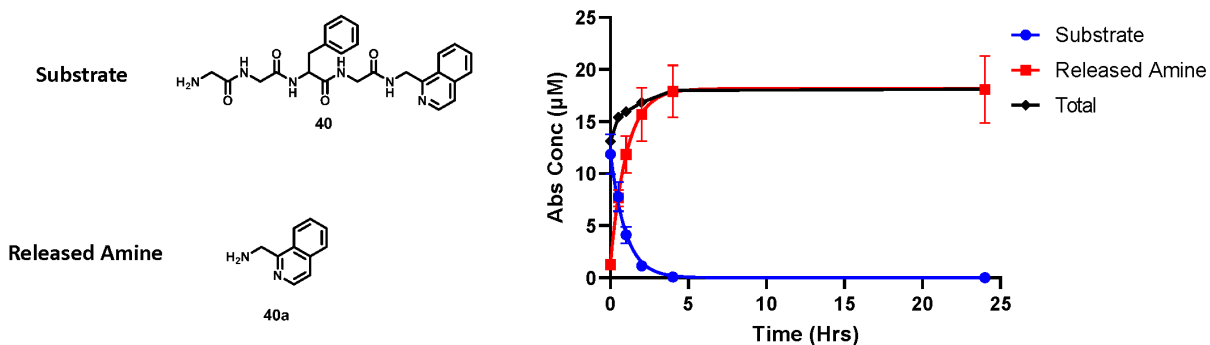
38



Cathepsin B Kinetics	T $\frac{1}{2}$ (hrs)	95% CI of t $\frac{1}{2}$ (hrs)
	5.86 hrs	[4.31 – 8.18]

Analyte	Condition	24 hrs Stability (%)
39	pH 5.0 Buffer Control	99
39a	pH 5.0 Buffer Control	80

39

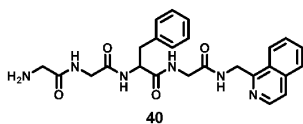


Cathepsin B Kinetics	T $\frac{1}{2}$ (hrs)	95% CI of t $\frac{1}{2}$ (hrs)
	0.669 hrs	[0.552 – 0.818]

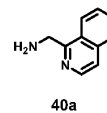
Analyte	Condition	24 hrs Stability (%)
40	pH 5.0 Buffer Control	79
40a	pH 5.0 Buffer Control	99

40

Substrate



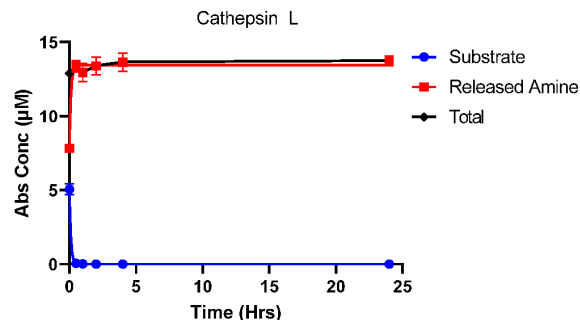
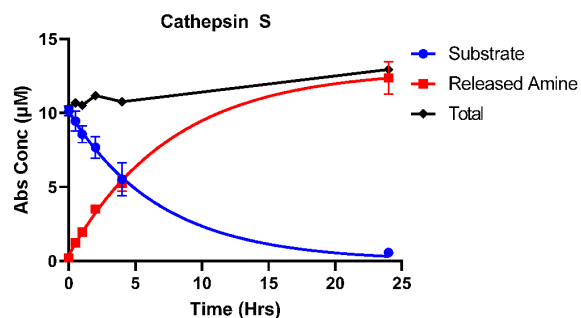
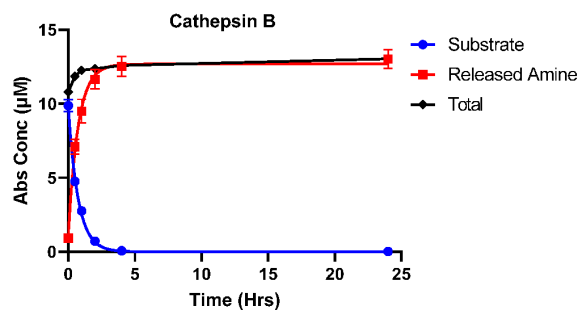
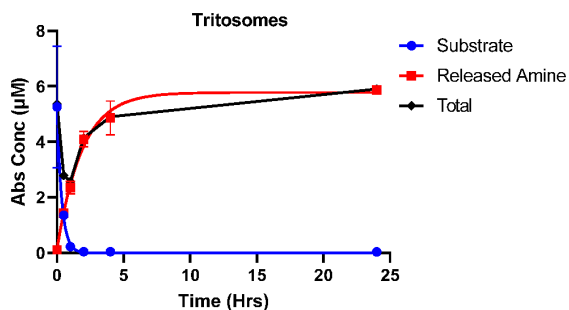
Released Amine

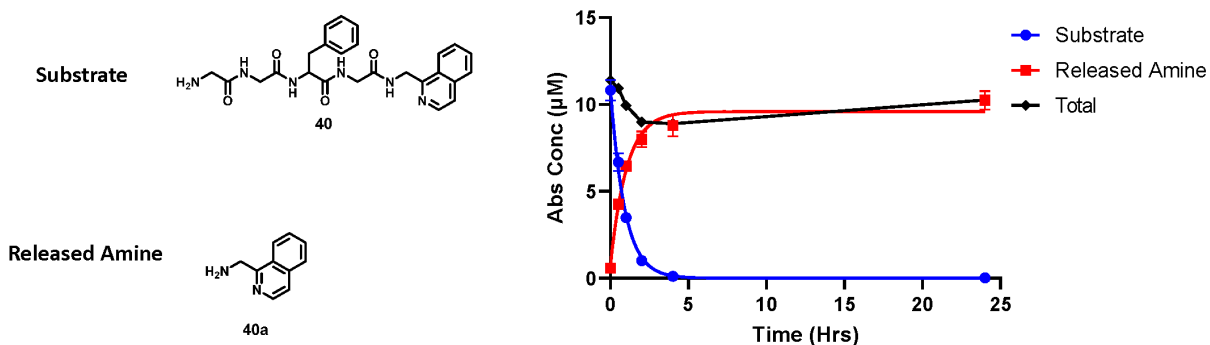


Enzyme	T ½ (hrs)	95% CI of t ½ (hrs)
Cathepsin B Kinetics	0.516 hrs	[0.487 – 0.546]
Cathepsin L Kinetics	0.0786 hrs	[N/A – 0.111]
Cathepsin S Kinetics	4.44 hrs	[3.75 – 6.55]
Tritosome Kinetics	0.249 hrs	[0.136 – 0.389]

Analyte	Condition	24 hrs Stability (%)
40	pH 5.0 Buffer Control	79
40a	pH 5.0 Buffer Control	99

Multi enzyme AF-049

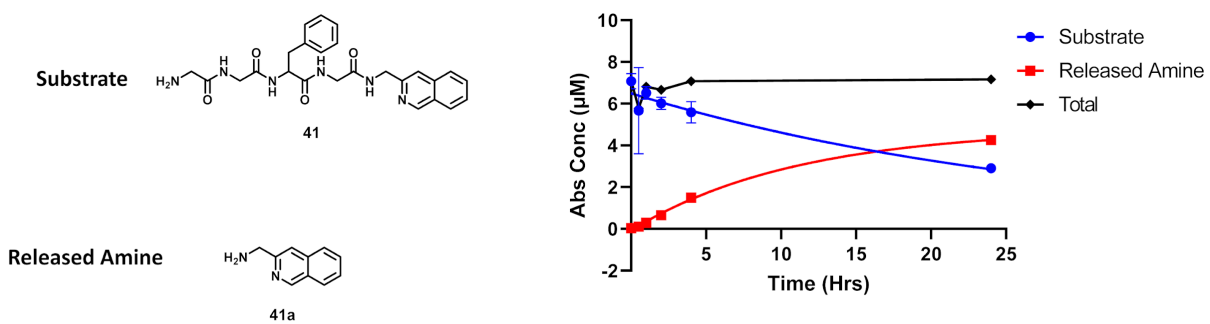




Cathepsin B Kinetics	T ½ (hrs)	95% CI of t ½ (hrs)
	0.631 hrs	[0.580 – 0.686]

Analyte	Condition	24 hrs Stability (%)
40	pH 5.0 Buffer Control	79
40a	pH 5.0 Buffer Control	99

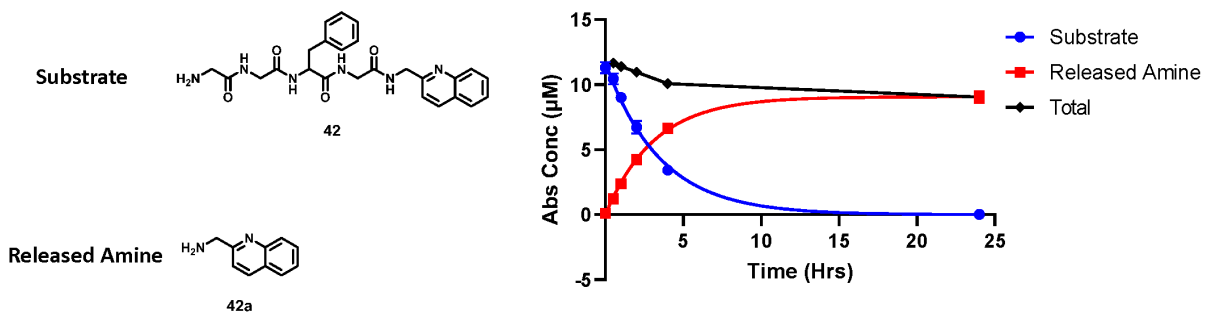
N-Capped 40



Cathepsin B Kinetics	T ½ (hrs)	95% CI of t ½ (hrs)
	20.2 hrs	[12.8 – 34.8]

Analyte	Condition	24 hrs Stability (%)
41	pH 5.0 Buffer Control	116
41a	pH 5.0 Buffer Control	96

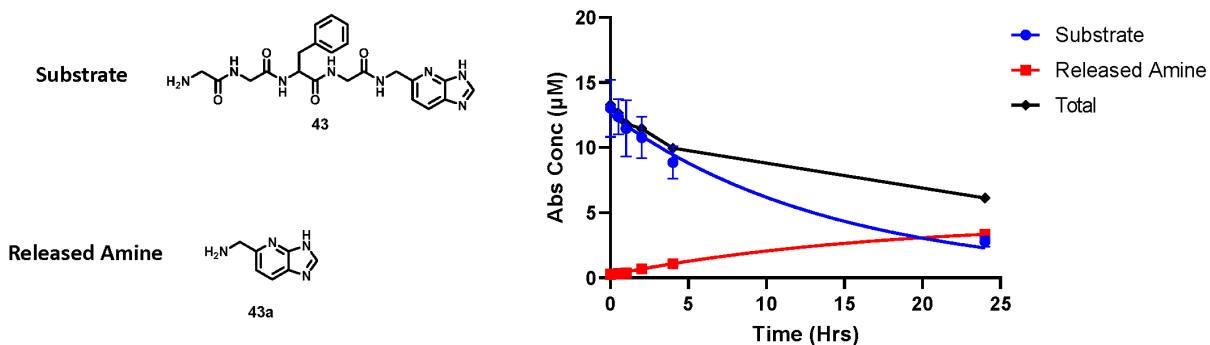
41



Cathepsin B Kinetics	T $\frac{1}{2}$ (hrs)	95% CI of t $\frac{1}{2}$ (hrs)
	2.44 hrs	[2.20 – 2.71]

Analyte	Condition	24 hrs Stability (%)
42	pH 5.0 Buffer Control	90
42a	pH 5.0 Buffer Control	94

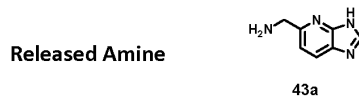
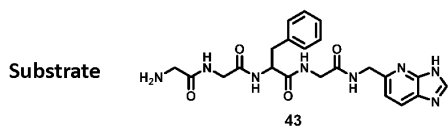
42



Cathepsin B Kinetics	T $\frac{1}{2}$ (hrs)	95% CI of t $\frac{1}{2}$ (hrs)
	9.78 hrs	[6.10 – 15.0]

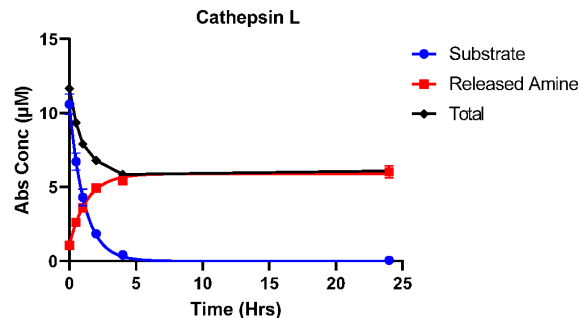
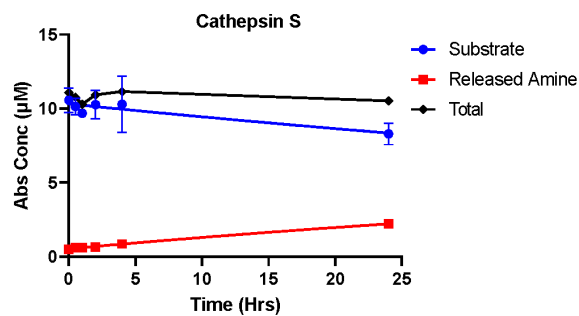
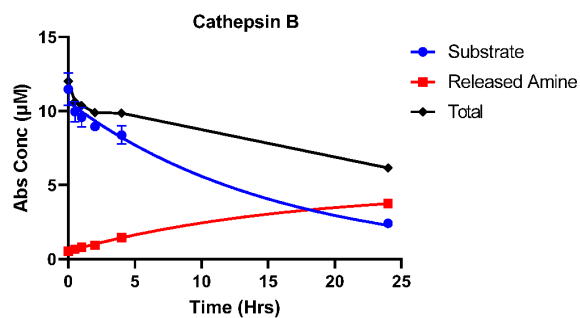
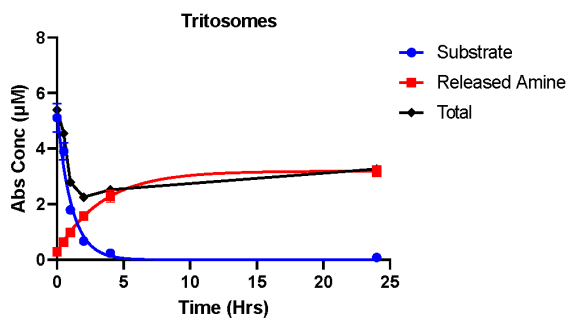
Analyte	Condition	24 hrs Stability (%)
43	pH 5.0 Buffer Control	106
43a	pH 5.0 Buffer Control	105

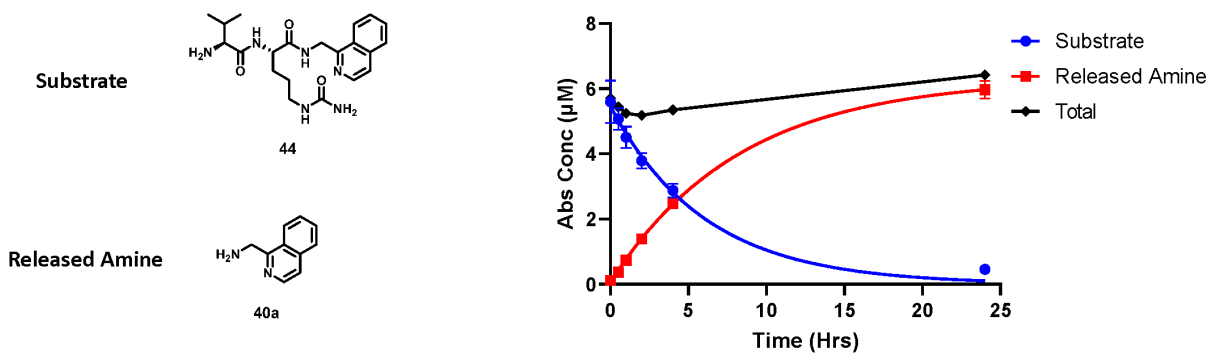
43



Cathepsin B Kinetics	T $\frac{1}{2}$ (hrs)	95% CI of t $\frac{1}{2}$ (hrs)
	10.8 hrs	[8.46 – 13.8]
Cathepsin L Kinetics	T $\frac{1}{2}$ (hrs)	95% CI of t $\frac{1}{2}$ (hrs)
	0.781 hrs	[0.709 – 0.862]
Cathepsin S Kinetics	T $\frac{1}{2}$ (hrs)	95% CI of t $\frac{1}{2}$ (hrs)
	No cleavage	
Tritosome Kinetics	T $\frac{1}{2}$ (hrs)	95% CI of t $\frac{1}{2}$ (hrs)
	0.756 hrs	[0.636 – 0.907]
Analyte	Condition	24 hrs Stability (%)
43	pH 5.0 Buffer Control	100
43a	pH 5.0 Buffer Control	105

Multi enzyme 43

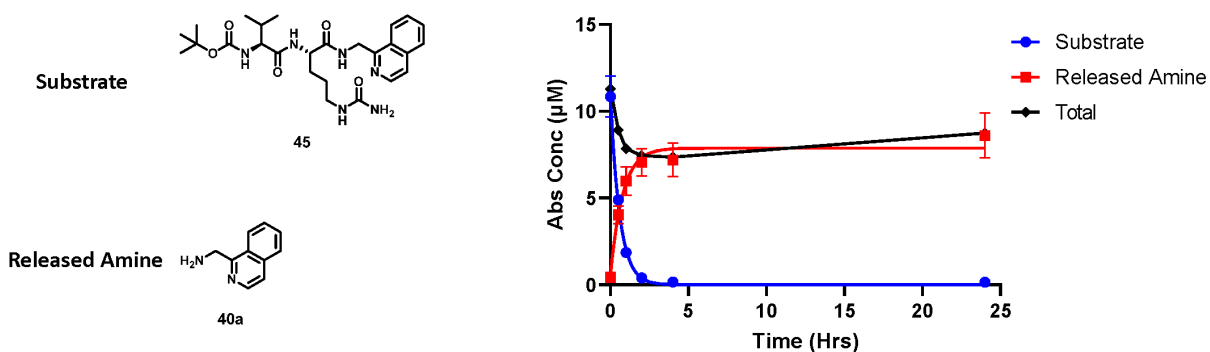




Cathepsin B Kinetics	T ½ (hrs)	95% CI of t ½ (hrs)
	4.19 hrs	[3.32 – 5.54]

Analyte	Condition	24 hrs Stability (%)
44	pH 5.0 Buffer Control	59
40a	pH 5.0 Buffer Control	63

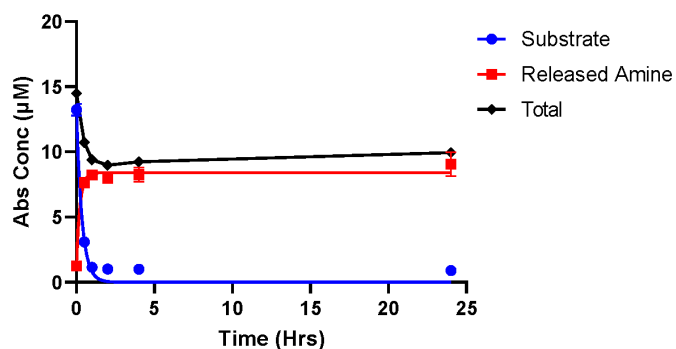
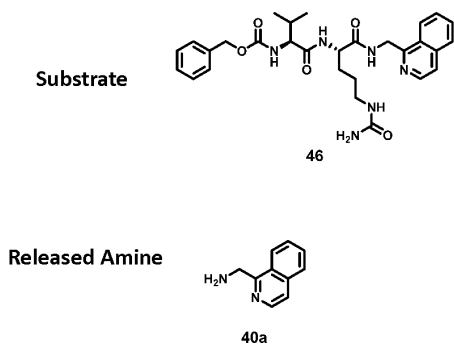
44



Cathepsin B Kinetics	T ½ (hrs)	95% CI of t ½ (hrs)
	0.416 hrs	[0.372 – 0.465]

Analyte	Condition	24 hrs Stability (%)
45	pH 5.0 Buffer Control	98
40a	pH 5.0 Buffer Control	63

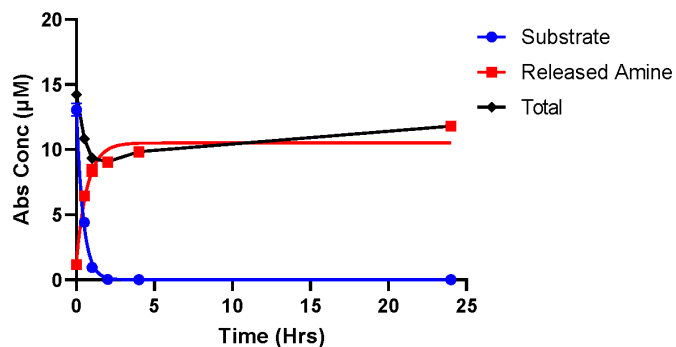
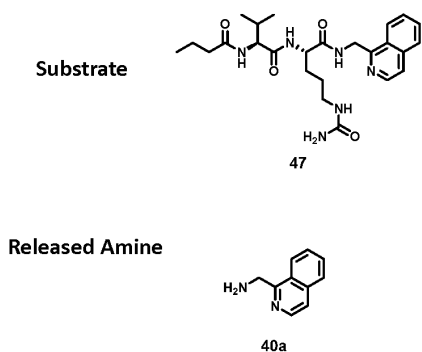
45



Cathepsin B Kinetics	T ½ (hrs)	95% CI of t ½ (hrs)
	0.250 hrs	[0.204 – 0.301]

Analyte	Condition	24 hrs Stability (%)
46	pH 5.0 Buffer Control	108
40a	pH 5.0 Buffer Control	63

46

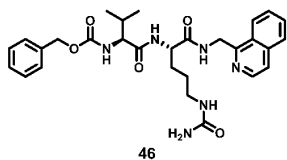


Cathepsin B Kinetics	T ½ (hrs)	95% CI of t ½ (hrs)
	0.302 hrs	[0.283 – 0.321]

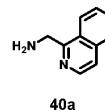
Analyte	Condition	24 hrs Stability (%)
47	pH 5.0 Buffer Control	94
40a	pH 5.0 Buffer Control	63

47

Substrate

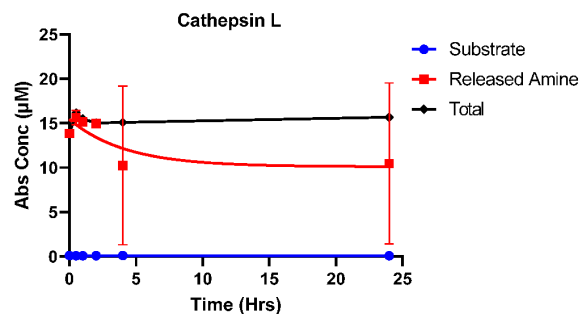
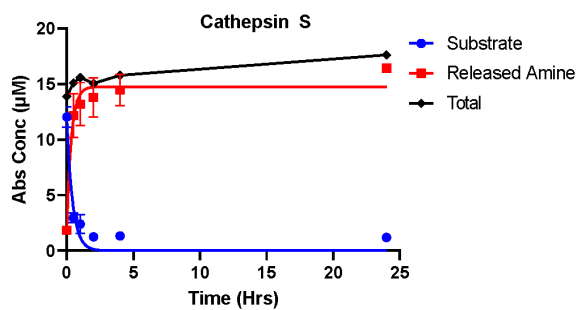
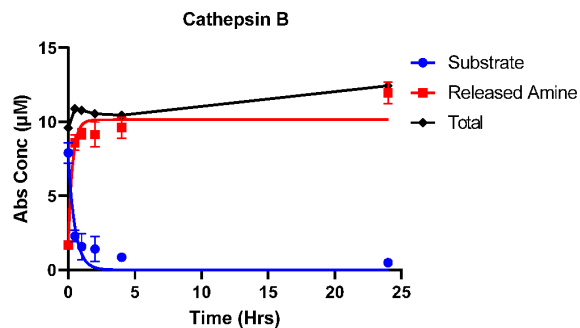
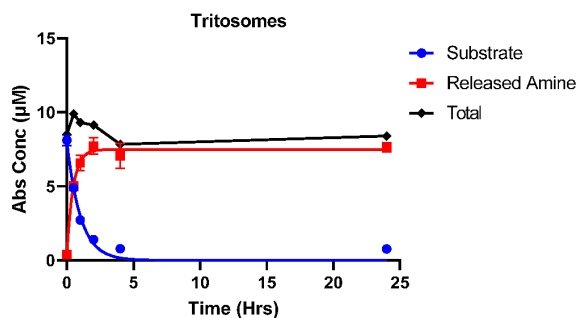


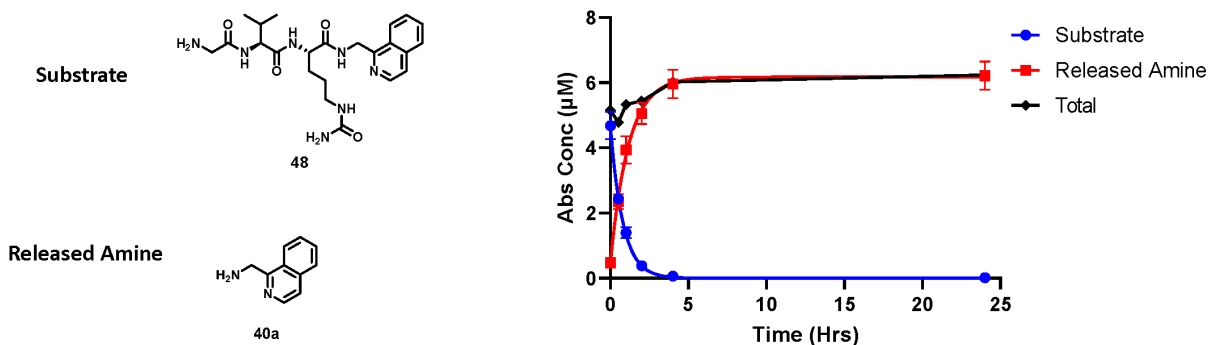
Released Amine



Cathepsin B Kinetics	T $\frac{1}{2}$ (hrs)	95% CI of t $\frac{1}{2}$ (hrs)
	0.355 hrs	[0.233 – 0.534]
Cathepsin L Kinetics	T $\frac{1}{2}$ (hrs)	95% CI of t $\frac{1}{2}$ (hrs)
	Immediate	
Cathepsin S Kinetics	T $\frac{1}{2}$ (hrs)	95% CI of t $\frac{1}{2}$ (hrs)
	0.193 hrs	[0.147 – 0.559]
Tritosome Kinetics	T $\frac{1}{2}$ (hrs)	95% CI of t $\frac{1}{2}$ (hrs)
	0.710 hrs	[0.601 – 0.845]
Analyte	Condition	24 hrs Stability (%)
46	pH 5.0 Buffer Control	108
40a	pH 5.0 Buffer Control	63

Multi enzyme 46

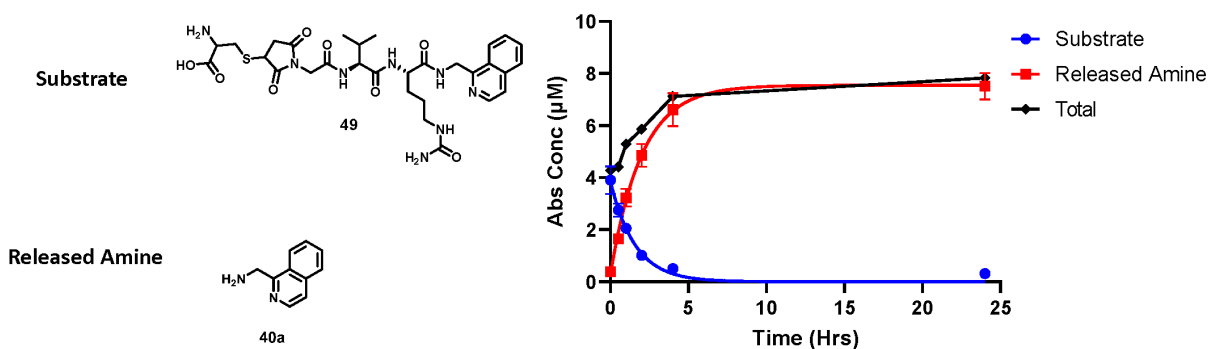




Cathepsin B Kinetics	T ½ (hrs)	95% CI of t ½ (hrs)
	0.555 hrs	[0.505 – 0.612]

Analyte	Condition	24 hrs Stability (%)
47	pH 5.0 Buffer Control	62
40a	pH 5.0 Buffer Control	63

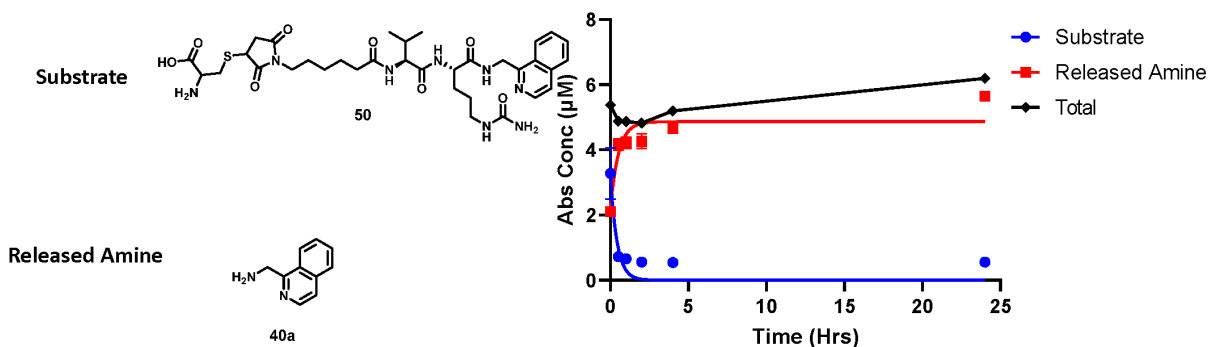
48



Cathepsin B Kinetics	T ½ (hrs)	95% CI of t ½ (hrs)
	1.01 hrs	[0.908 – 1.34]

Analyte	Condition	24 hrs Stability (%)
49	pH 5.0 Buffer Control	87
40a	pH 5.0 Buffer Control	63

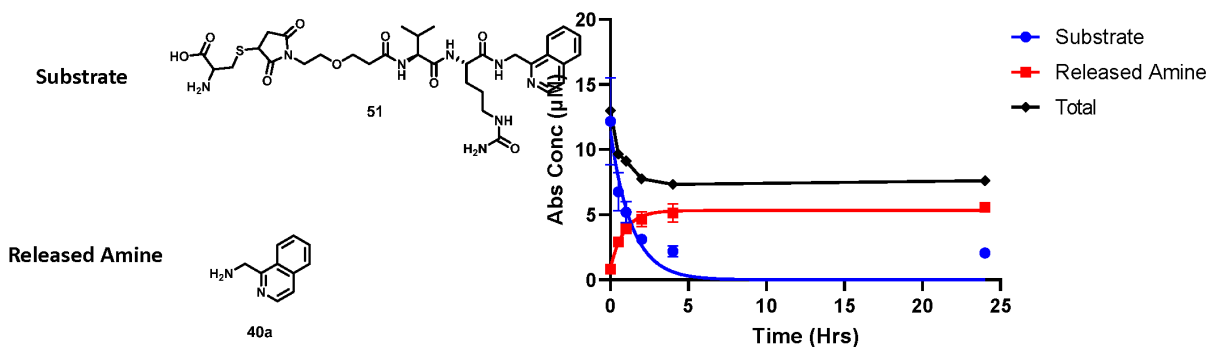
49



Cathepsin B Kinetics	T ½ (hrs)	95% CI of t ½ (hrs)
	0.295 hrs	[0.141 – 0.538]

Analyte	Condition	24 hrs Stability (%)
50	pH 5.0 Buffer Control	98
40a	pH 5.0 Buffer Control	63

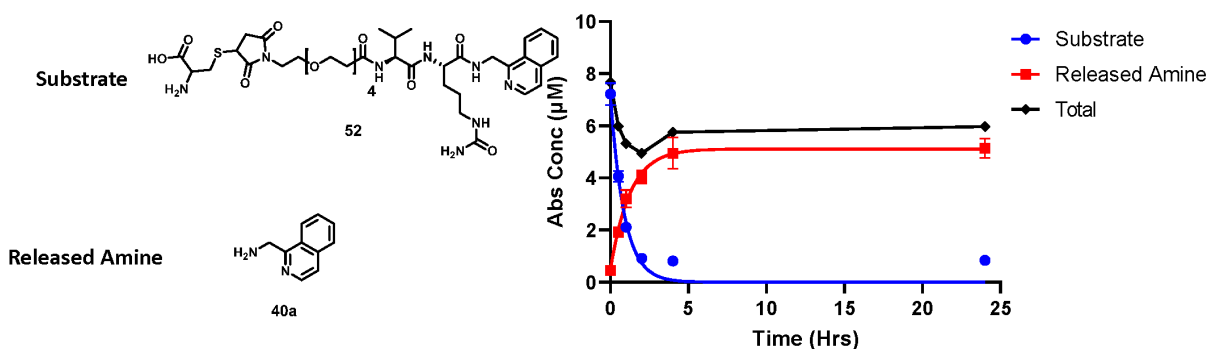
50



Cathepsin B Kinetics	T ½ (hrs)	95% CI of t ½ (hrs)
	0.947 hrs	[0.587 – 1.64]

Analyte	Condition	24 hrs Stability (%)
51	pH 5.0 Buffer Control	100
40a	pH 5.0 Buffer Control	63

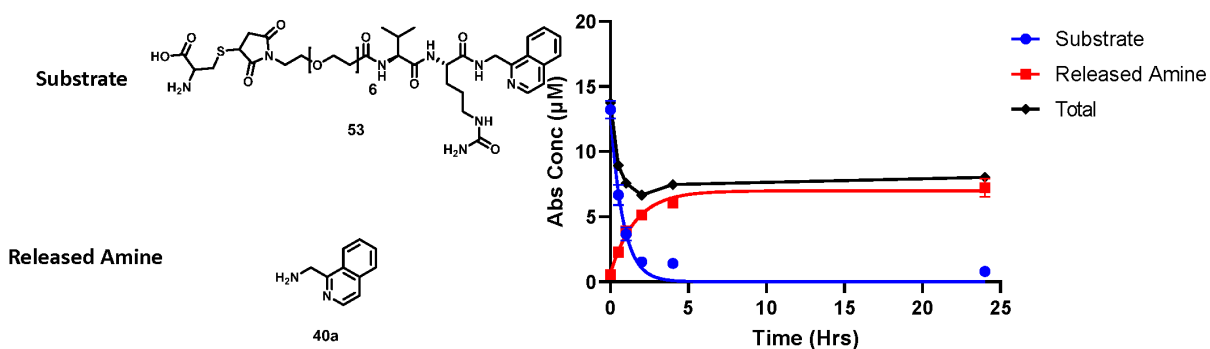
51



Cathepsin B Kinetics	T $\frac{1}{2}$ (hrs)	95% CI of t $\frac{1}{2}$ (hrs)
	0.612 hrs	[0.503 – 0.754]

Analyte	Condition	24 hrs Stability (%)
52	pH 5.0 Buffer Control	102
40a	pH 5.0 Buffer Control	63

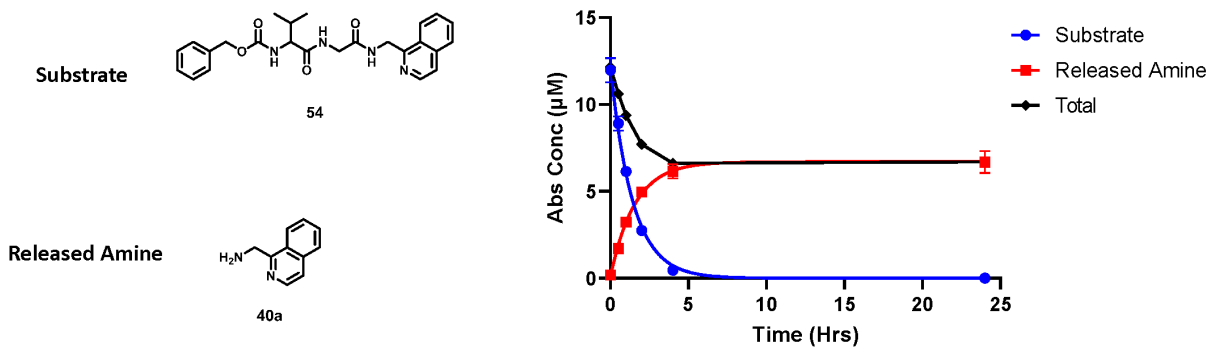
52



Cathepsin B Kinetics	T $\frac{1}{2}$ (hrs)	95% CI of t $\frac{1}{2}$ (hrs)
	0.554 hrs	[0.466 – 0.664]

Analyte	Condition	24 hrs Stability (%)
53	pH 5.0 Buffer Control	110
40a	pH 5.0 Buffer Control	63

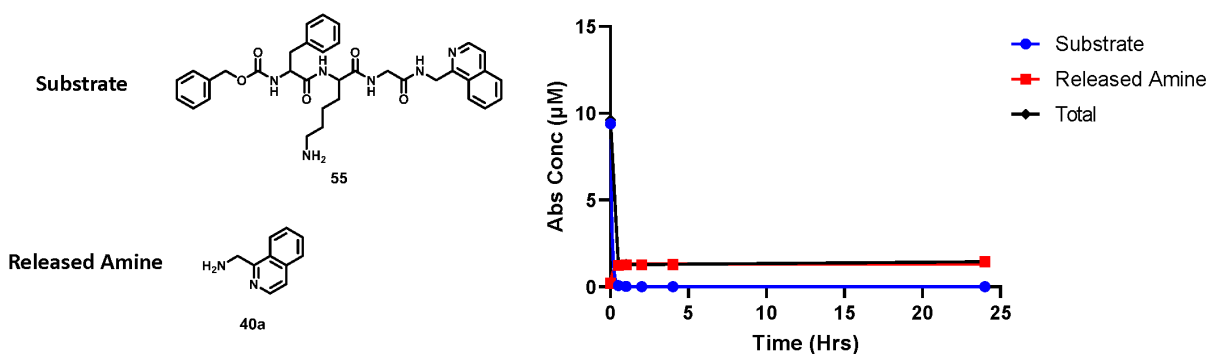
53



Cathepsin B Kinetics	T ½ (hrs)	95% CI of t ½ (hrs)
	0.982 hrs	[0.910 – 1.06]

Analyte	Condition	24 hrs Stability (%)
54	pH 5.0 Buffer Control	93
40a	pH 5.0 Buffer Control	63

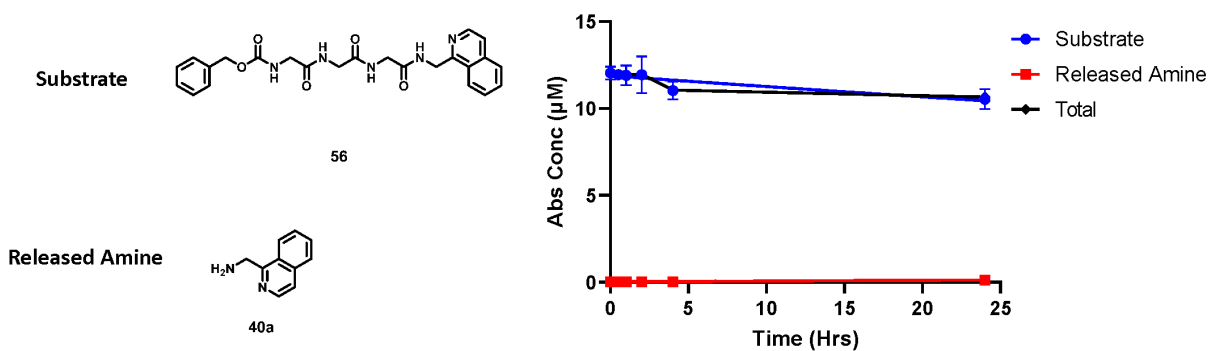
54



Cathepsin B Kinetics	T ½ (hrs)	95% CI of t ½ (hrs)
	0.0704 hrs	[N/A – 0.0872]

Analyte	Condition	24 hrs Stability (%)
55	pH 5.0 Buffer Control	97
40a	pH 5.0 Buffer Control	63

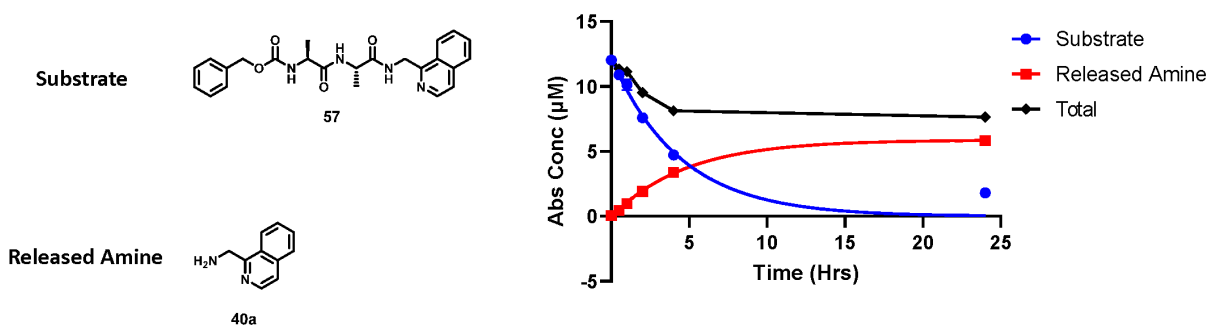
55



Cathepsin B Kinetics	T ½ (hrs)	95% CI of t ½ (hrs)
	No cleavage	

Analyte	Condition	24 hrs Stability (%)
56	pH 5.0 Buffer Control	100
40a	pH 5.0 Buffer Control	63

56

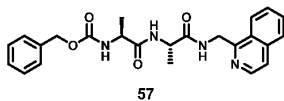


Cathepsin B Kinetics	T ½ (hrs)	95% CI of t ½ (hrs)
	3.06 hrs	[2.50 – 0.391]

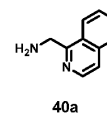
Analyte	Condition	24 hrs Stability (%)
57	pH 5.0 Buffer Control	93
40a	pH 5.0 Buffer Control	63

57

Substrate



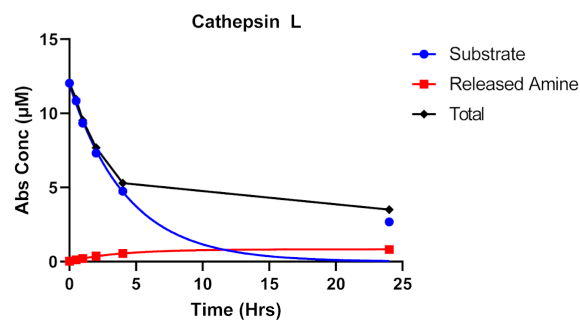
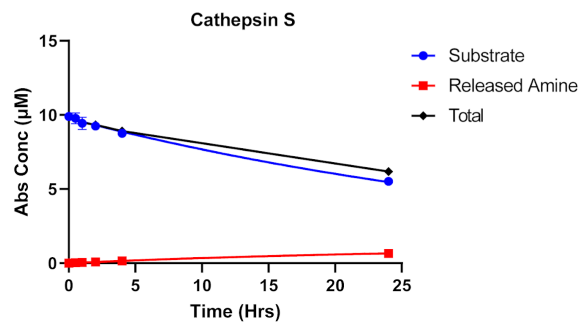
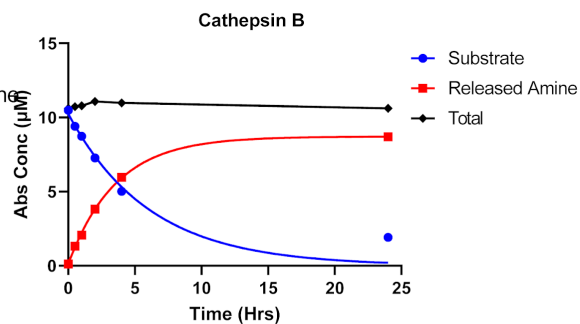
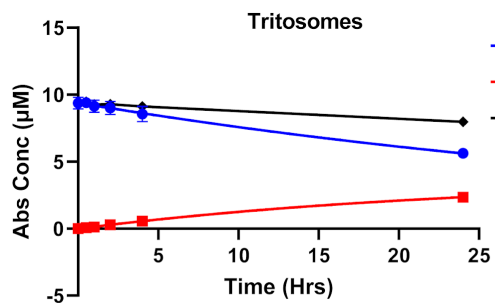
Released Amine

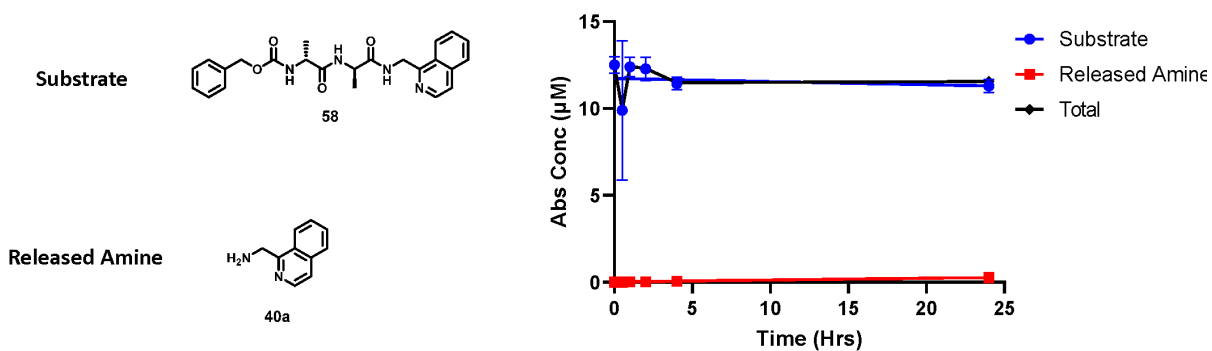


Cathepsin B Kinetics	T ½ (hrs)	95% CI of t ½ (hrs)
	4.23 hrs	[3.16 – 6.40]
Cathepsin L Kinetics	T ½ (hrs)	95% CI of t ½ (hrs)
	2.98 hrs	[2.23 – 4.39]
Cathepsin S Kinetics	T ½ (hrs)	95% CI of t ½ (hrs)
	13.4 hrs	[11.4 – N/A]
Tritosome Kinetics	T ½ (hrs)	95% CI of t ½ (hrs)
	32.3 hrs	[27.2 – 39.2]

Analyte	Condition	24 hrs Stability (%)
57	pH 5.0 Buffer Control	98
40a	pH 5.0 Buffer Control	63

Multi enzyme 57

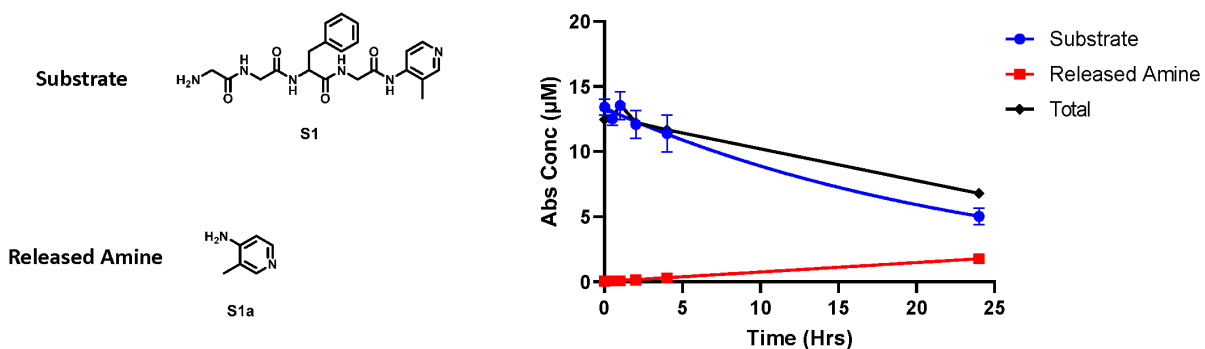




Cathepsin B Kinetics	T ½ (hrs)	95% CI of t ½ (hrs)
	No cleavage	

Analyte	Condition	24 hrs Stability (%)
58	pH 5.0 Buffer Control	96
40a	pH 5.0 Buffer Control	63

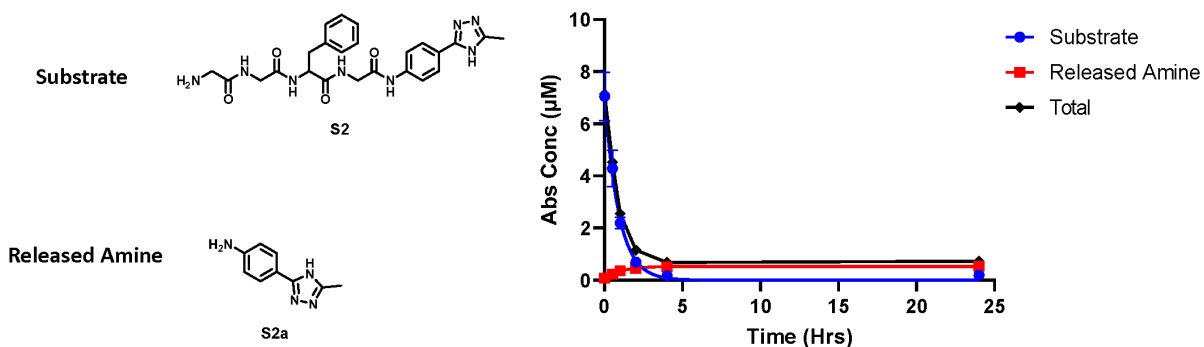
58



Cathepsin B Kinetics	T ½ (hrs)	95% CI of t ½ (hrs)
	17.1 hrs	[13.5 – 21.9]

Analyte	Condition	24 hrs Stability (%)
S1	pH 5.0 Buffer Control	92
S1a	pH 5.0 Buffer Control	97

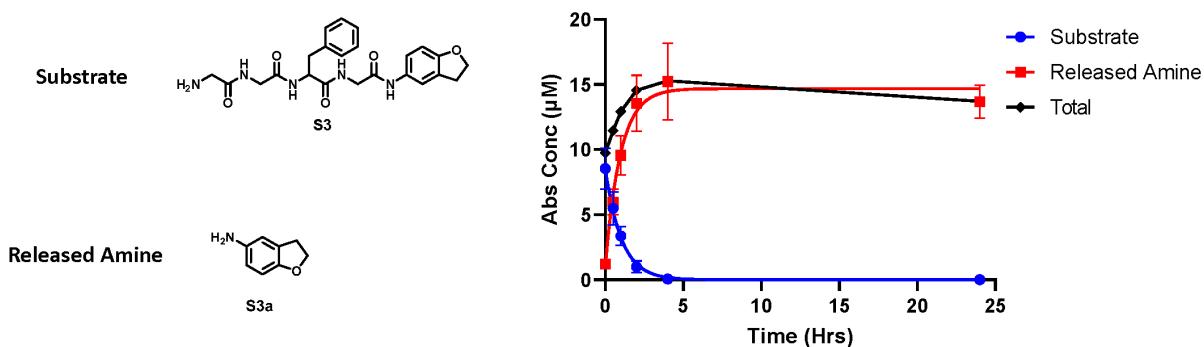
S1



Cathepsin B Kinetics	T ½ (hrs)	95% CI of t ½ (hrs)
	0.623 hrs	[0.531 – 0.735]

Analyte	Condition	24 hrs Stability (%)
S2	pH 5.0 Buffer Control	87
S2a	pH 5.0 Buffer Control	84

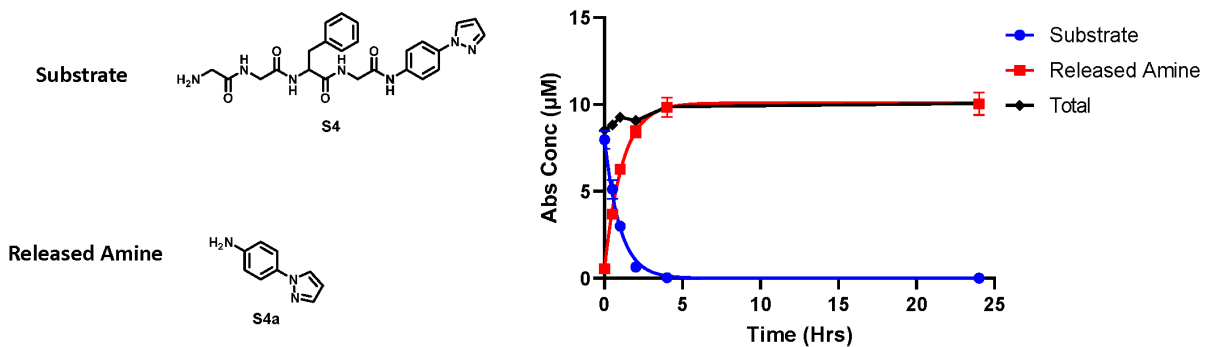
S2



Cathepsin B Kinetics	T ½ (hrs)	95% CI of t ½ (hrs)
	0.715 hrs	[0.571 – 0.907]

Analyte	Condition	24 hrs Stability (%)
S3	pH 5.0 Buffer Control	93
S3a	pH 5.0 Buffer Control	81

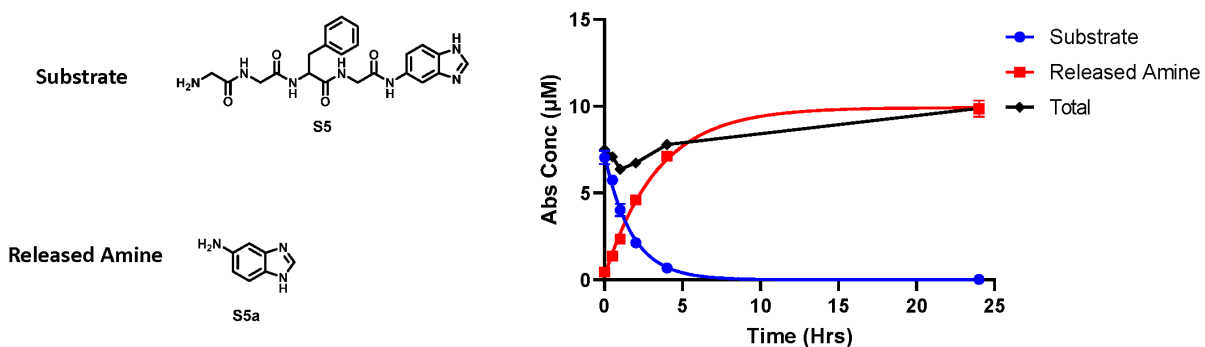
S3



Cathepsin B Kinetics	T ½ (hrs)	95% CI of t ½ (hrs)
	0.675hrs	[0.603 – 0.758]

Analyte	Condition	24 hrs Stability (%)
S4	pH 5.0 Buffer Control	96
S4a	pH 5.0 Buffer Control	98

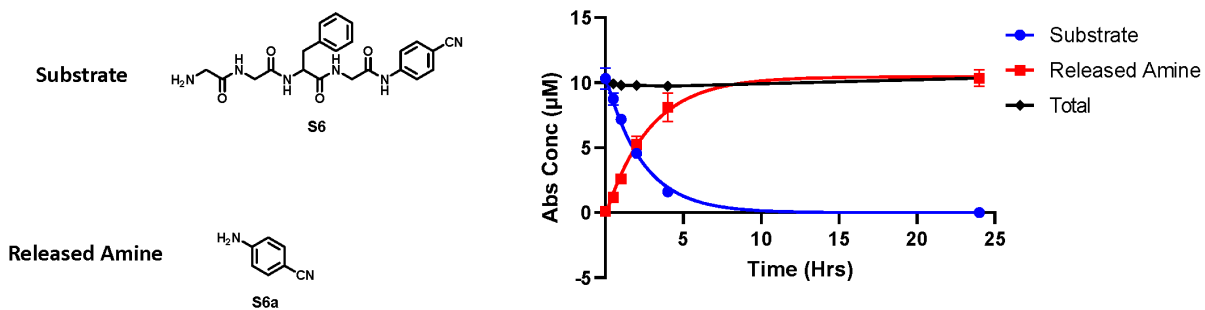
S4



Cathepsin B Kinetics	T ½ (hrs)	95% CI of t ½ (hrs)
	1.20 hrs	[1.09 – 1.33]

Analyte	Condition	24 hrs Stability (%)
S5	pH 5.0 Buffer Control	101
S5a	pH 5.0 Buffer Control	101

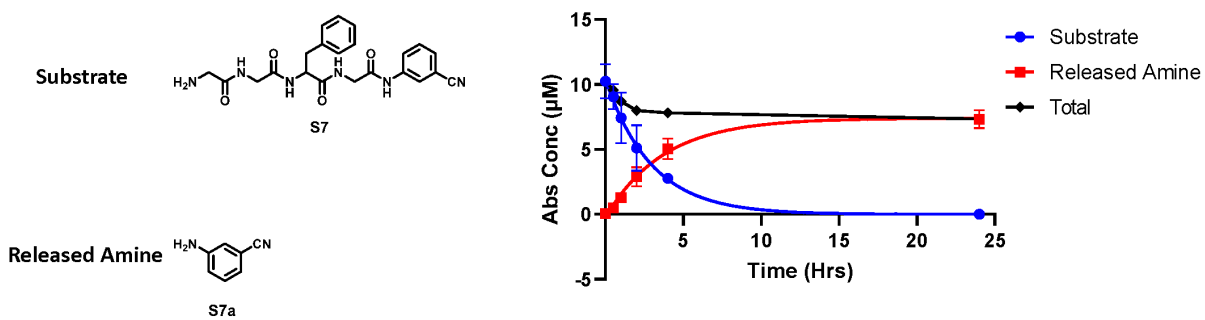
S5



Cathepsin B Kinetics	T $\frac{1}{2}$ (hrs)	95% CI of t $\frac{1}{2}$ (hrs)
	1.64 hrs	[1.48 – 1.83]

Analyte	Condition	24 hrs Stability (%)
S6	pH 5.0 Buffer Control	96
S6a	pH 5.0 Buffer Control	103

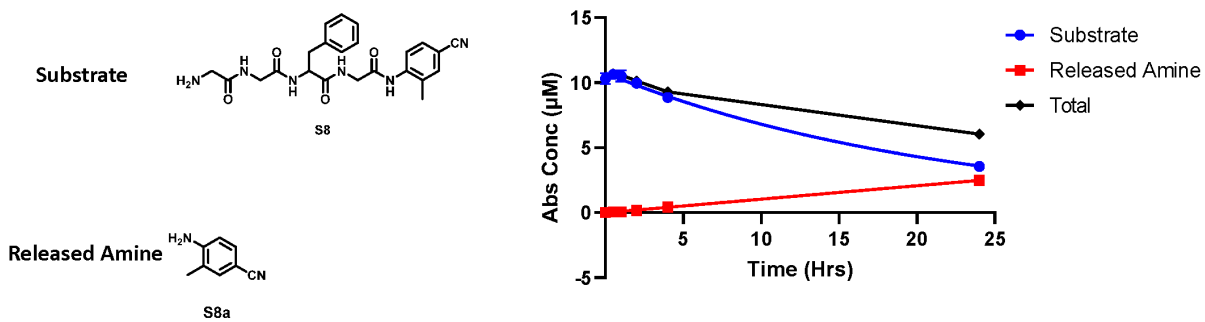
S6



Cathepsin B Kinetics	T $\frac{1}{2}$ (hrs)	95% CI of t $\frac{1}{2}$ (hrs)
	2.05 hrs	[1.55 – 2.82]

Analyte	Condition	24 hrs Stability (%)
S7	pH 5.0 Buffer Control	100
S7a	pH 5.0 Buffer Control	95

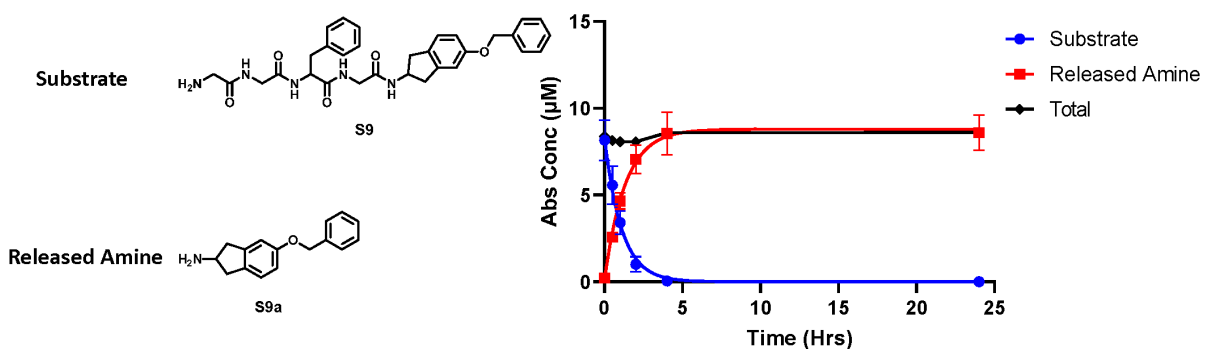
S7



Cathepsin B Kinetics	T ½ (hrs)	95% CI of t ½ (hrs)
	15.2 hrs	[13.6 – 17.0]

Analyte	Condition	24 hrs Stability (%)
S8	pH 5.0 Buffer Control	94
S8a	pH 5.0 Buffer Control	98

S8

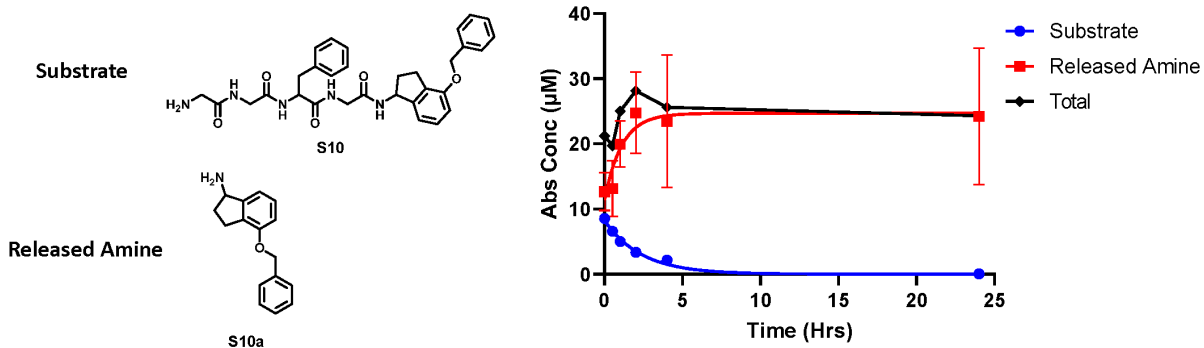


Cathepsin B Kinetics	T ½ (hrs)	95% CI of t ½ (hrs)
	0.759 hrs	[0.625 – 0.931]

Analyte	Condition	24 hrs Stability (%)
S9	pH 5.0 Buffer Control	105
S9a	pH 5.0 Buffer Control	100

S9

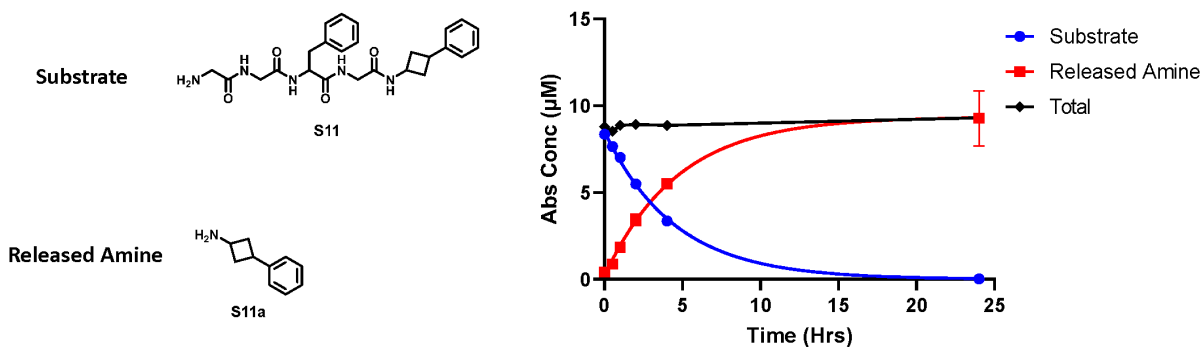
*S10a standard not pure, calculated payload exceeds 10 μM



Cathepsin B Kinetics	T $\frac{1}{2}$ (hrs)	95% CI of t $\frac{1}{2}$ (hrs)
	1.64 hrs	[1.43 – 1.90]

Analyte	Condition	24 hrs Stability (%)
S10	pH 5.0 Buffer Control	96
S10a	pH 5.0 Buffer Control	110

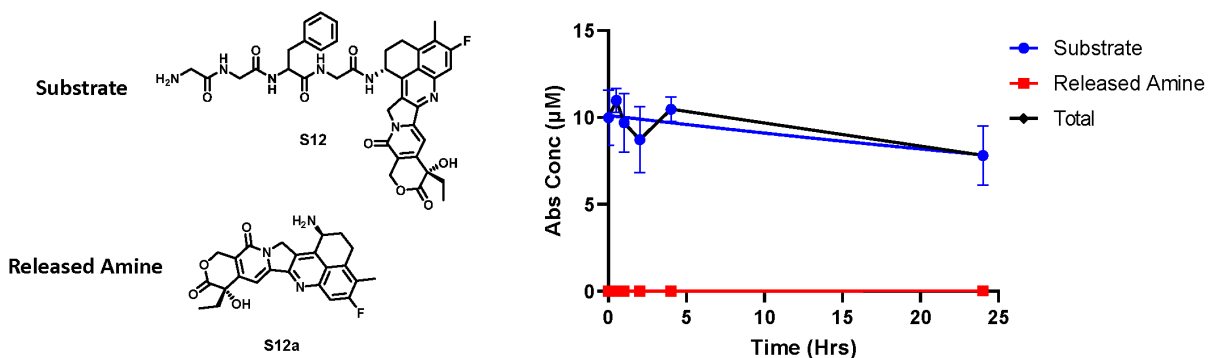
S10



Cathepsin B Kinetics	T $\frac{1}{2}$ (hrs)	95% CI of t $\frac{1}{2}$ (hrs)
	3.11 hrs	[2.88 – 3.37]

Analyte	Condition	24 hrs Stability (%)
S11	pH 5.0 Buffer Control	100
S11a	pH 5.0 Buffer Control	100

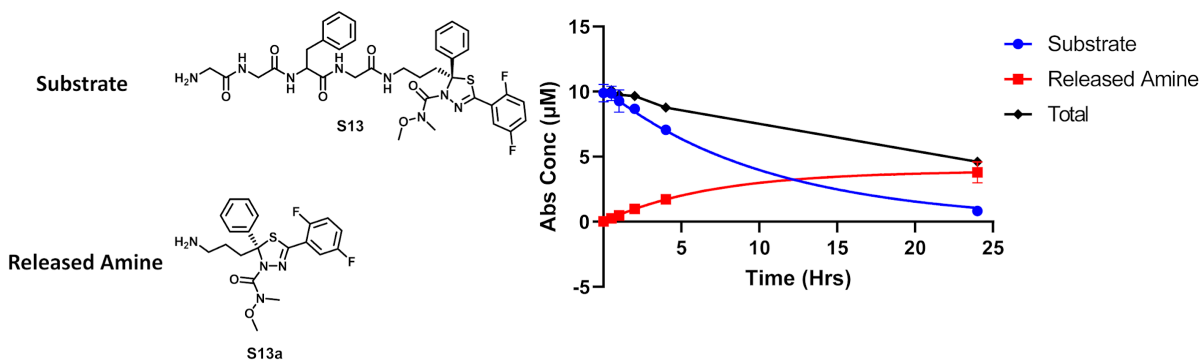
S11



Cathepsin B Kinetics	T ½ (hrs)	95% CI of t ½ (hrs)
	No cleavage	

Analyte	Condition	24 hrs Stability (%)
S12	pH 5.0 Buffer Control	94
S12a	pH 5.0 Buffer Control	100

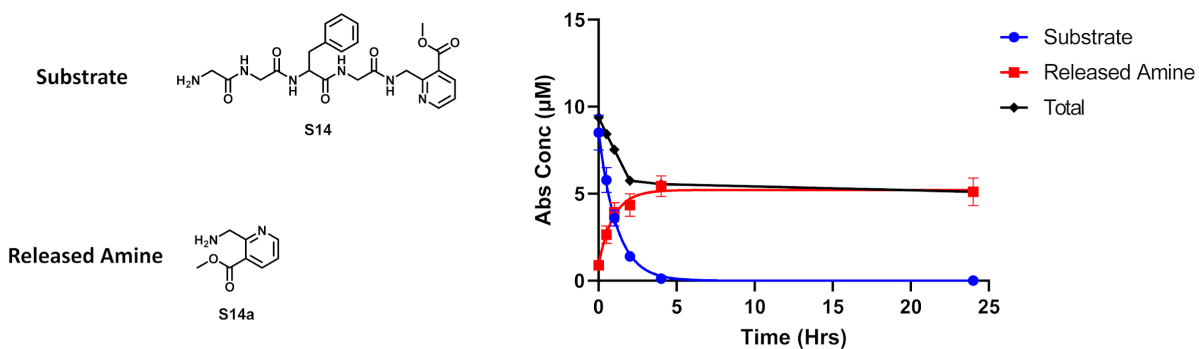
S12



Cathepsin B Kinetics	T ½ (hrs)	95% CI of t ½ (hrs)
	7.37 hrs	[6.17 – 8.78]

Analyte	Condition	24 hrs Stability (%)
S13	pH 5.0 Buffer Control	97
S13a	pH 5.0 Buffer Control	99

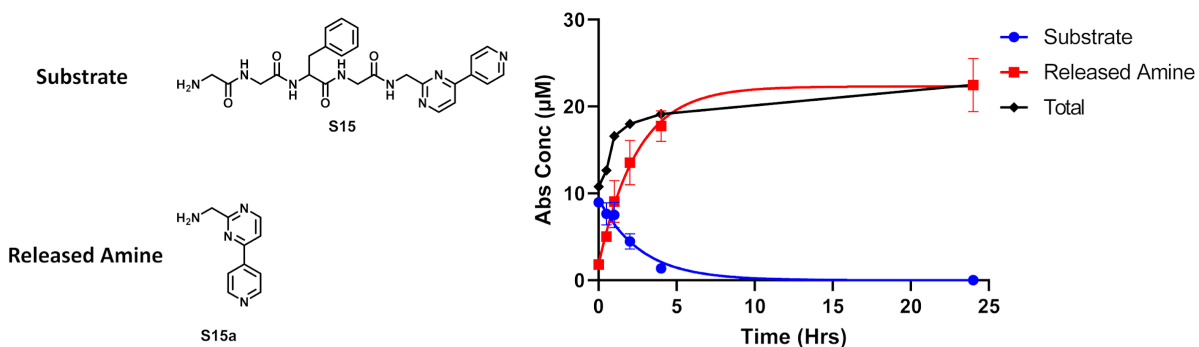
S13



Cathepsin B Kinetics	T $\frac{1}{2}$ (hrs)	95% CI of t $\frac{1}{2}$ (hrs)
	0.798 hrs	[0.694 – 0.922]

Analyte	Condition	24 hrs Stability (%)
S14	pH 5.0 Buffer Control	95
S14a	pH 5.0 Buffer Control	93

S14

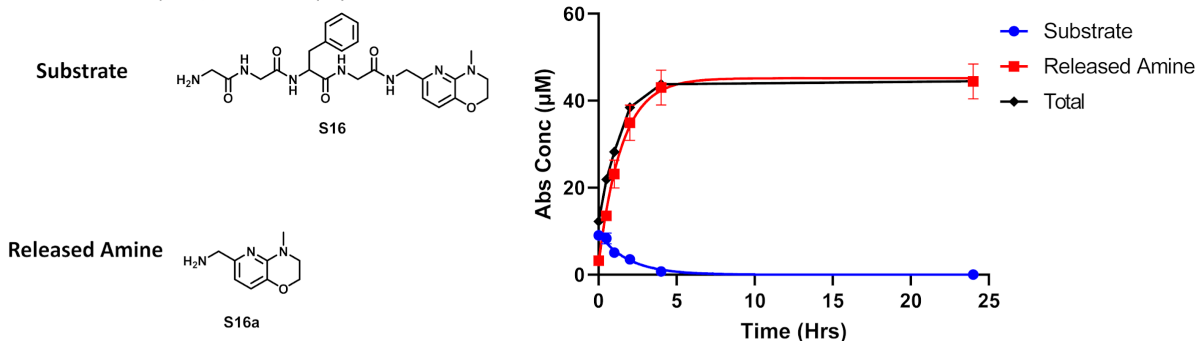


Cathepsin B Kinetics	T $\frac{1}{2}$ (hrs)	95% CI of t $\frac{1}{2}$ (hrs)
	1.86 hrs	[1.45 – 2.46]

Analyte	Condition	24 hrs Stability (%)
S15	pH 5.0 Buffer Control	97
S15a	pH 5.0 Buffer Control	107

S15

*S16a standard not pure, calculated payload exceeds 10 uM

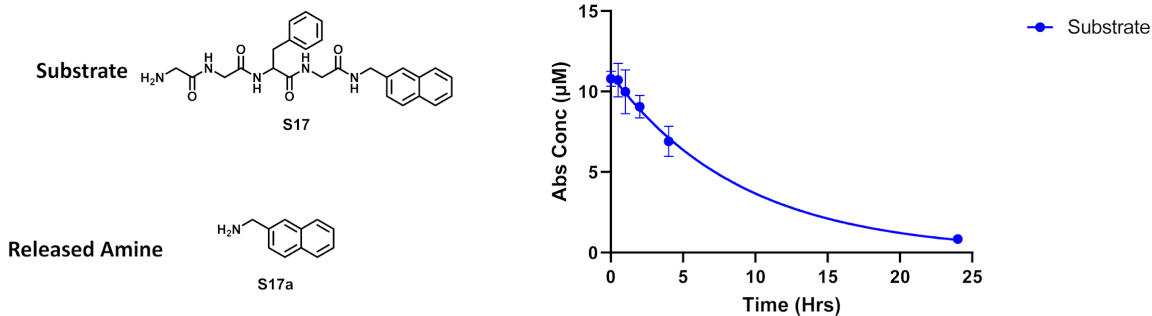


Cathepsin B Kinetics	T ½ (hrs)	95% CI of t ½ (hrs)
	1.32 hrs	[1.06 - 1.68]

Analyte	Condition	24 hrs Stability (%)
S16	pH 5.0 Buffer Control	99
S16a	pH 5.0 Buffer Control	101

S16

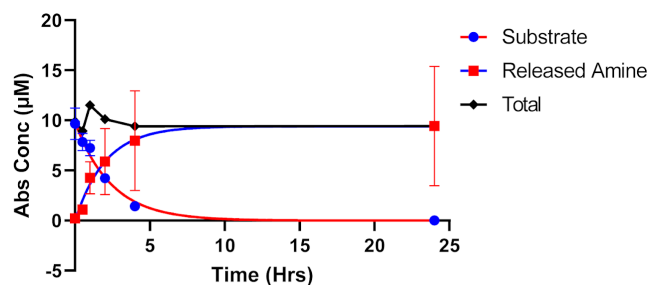
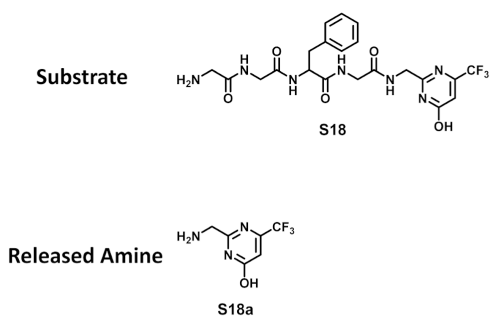
*Not able to detect S17a



Cathepsin B Kinetics	T ½ (hrs)	95% CI of t ½ (hrs)
	6.27 hrs	[4.79 – 8.26]

Analyte	Condition	24 hrs Stability (%)
S17	pH 5.0 Buffer Control	98
S17a	pH 5.0 Buffer Control	Cannot detect

S17

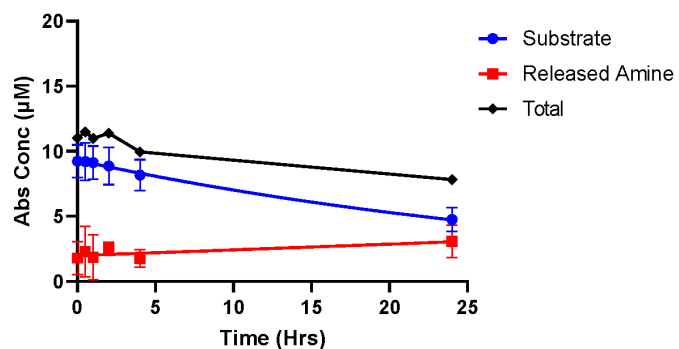
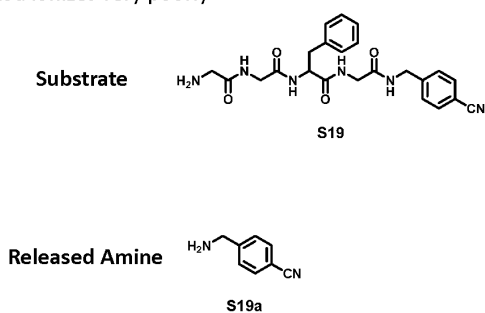


Cathepsin B Kinetics	T ½ (hrs)	95% CI of t ½ (hrs)
	1.67 hrs	[1.37 – 2.08]

Analyte	Condition	24 hrs Stability (%)
S18	pH 5.0 Buffer Control	90
S18a	pH 5.0 Buffer Control	92

S18

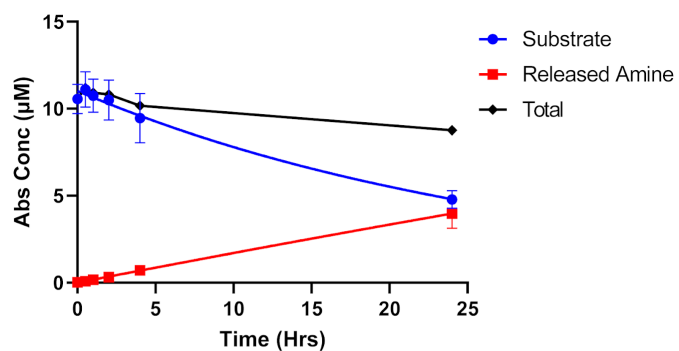
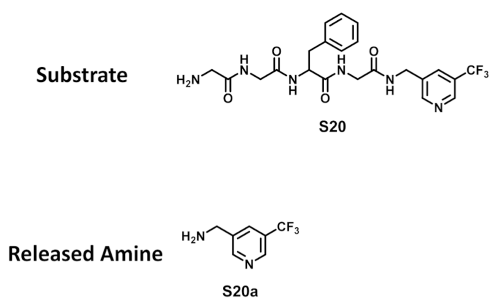
*S19a ionizes very poorly



Cathepsin B Kinetics	T ½ (hrs)	95% CI of t ½ (hrs)
	24.6 hrs	[16.3 – 41.0]

Analyte	Condition	24 hrs Stability (%)
S19	pH 5.0 Buffer Control	100
S19a	pH 5.0 Buffer Control	81

S19



Cathepsin B Kinetics	T ½ (hrs)	95% CI of t ½ (hrs)
	20.3 hrs	[15.1 – 27.4]

Analyte	Condition	24 hrs Stability (%)
S20	pH 5.0 Buffer Control	89
S20a	pH 5.0 Buffer Control	97

S20

Bibliography

1. Bornscheuer, U. T. *et al.* Engineering the third wave of biocatalysis. *Nature* **485**, 185–194 (2012).
2. Atanasov, A. G. *et al.* Discovery and resupply of pharmacologically active plant-derived natural products: A review. *Biotechnology Advances* **33**, 1582–1614 (2015).
3. Harvey, A. L., Edrada-Ebel, R. & Quinn, R. J. The re-emergence of natural products for drug discovery in the genomics era. *Nature Reviews Drug Discovery* **2015** *14*:2 **14**, 111–129 (2015).
4. Atanasov, A. G. *et al.* Natural products in drug discovery: advances and opportunities. *Nature Reviews Drug Discovery* **2021** *20*:3 **20**, 200–216 (2021).
5. Ye, L., Yang, C. & Yu, H. From molecular engineering to process engineering: development of high-throughput screening methods in enzyme directed evolution. *Applied Microbiology and Biotechnology* **102**, 559–567 (2018).
6. Leemhuis, H., Kelly, R. M. & Dijkhuizen, L. Directed evolution of enzymes: Library screening strategies. *IUBMB Life* **61**, 222–228 (2009).
7. Valavanidis, A. Biocatalysis and directed evolution in the pharmaceutical industry. New developments for ‘green’ synthetic methods of high value pharmaceuticals. *Pharmakeftiki* **28**, 117–130 (2016).
8. Shafee, T. Evolvability of a viral protease: experimental evolution of catalysis, robustness and specificity. (2014).
9. Wang, T.-W. *et al.* Mutant Library Construction in Directed Molecular Evolution. *Molecular Biotechnology* **34**, 55–68 (2006).
10. Wójcik, M., Telzerow, A., Quax, W. J. & Boersma, Y. L. High-throughput screening in protein engineering: Recent advances and future perspectives. *International Journal of Molecular Sciences* **16**, 24918–24945 (2015).
11. Xue, Y. P., Yang, Y. K., Lv, S. Z., Liu, Z. Q. & Zheng, Y. G. High-throughput screening methods for nitrilases. *Applied Microbiology and Biotechnology* **100**, 3421–3432 (2016).

12. Fallah-Araghi, A., Baret, J.-C., Ryckelynck, M. & Griffiths, A. D. A completely in vitro ultrahigh-throughput droplet-based microfluidic screening system for protein engineering and directed evolution. *Lab on a Chip* **12**, 882 (2012).
13. Hager, D. B., Dovichi, N. J., Klassen, J. & Kebarle, P. Droplet Electrospray Mass Spectrometry. *Analytical Chemistry* **66**, 3944–3949 (1994).
14. Koster, S. & Verpoorte, E. A decade of microfluidic analysis coupled with electrospray mass spectrometry: An overview. *Lab on a Chip* **7**, 1394–1412 (2007).
15. Xiang, F., Lin, Y., Wen, J., Matson, D. W. & Smith, R. D. An integrated microfabricated device for dual microdialysis and on-line ESI-ion trap mass spectrometry for analysis of complex biological samples. *Analytical Chemistry* **71**, 1485–1490 (1999).
16. Pei, J., Li, Q., Lee, M. S., Valaskovic, G. A. & Kennedy, R. T. Analysis of samples stored as individual plugs in a capillary by electrospray ionization mass spectrometry. *Analytical Chemistry* **81**, 6558–6561 (2009).
17. Xue, Q. *et al.* Multichannel microchip electrospray mass spectrometry. *Analytical Chemistry* **69**, 426–430 (1997).
18. Theberge, A. B. *et al.* Microdroplets in microfluidics: An evolving platform for discoveries in chemistry and biology. *Angewandte Chemie - International Edition* **49**, 5846–5868 (2010).
19. Bachler, S. *et al.* Microfluidic Platform for Multimodal Analysis of Enzyme Secretion in Nanoliter Droplet Arrays. *Analytical Chemistry* **91**, 2066–2073 (2019).
20. Price, A. K. & Paegel, B. M. Discovery in Droplets. *Analytical Chemistry* **88**, 339–353 (2016).
21. Wink, K. *et al.* An integrated chip-mass spectrometry and epifluorescence approach for online monitoring of bioactive metabolites from incubated Actinobacteria in picoliter droplets. *Analytical and Bioanalytical Chemistry* **410**, 7679–7687 (2018).
22. Ngernsutivorakul, T., Steyer, D. J., Valenta, A. C. & Kennedy, R. T. *In Vivo* Chemical Monitoring at High Spatiotemporal Resolution Using Microfabricated Sampling Probes and Droplet-Based Microfluidics Coupled to Mass Spectrometry. *Analytical Chemistry* **90**, 10943–10950 (2018).
23. Sun, X., Kelly, R. T., Tang, K. & Smith, R. D. Membrane-based emitter for coupling microfluidics with ultrasensitive nanoelectrospray ionization-mass spectrometry. *Analytical Chemistry* **83**, 5797–5803 (2011).
24. Zhu, Y. & Fang, Q. Integrated droplet analysis system with electrospray ionization-mass spectrometry using a hydrophilic tongue-based droplet extraction interface. *Analytical Chemistry* **82**, 8361–8366 (2010).

25. Smith, C. A. *et al.* Sensitive, high throughput detection of proteins in individual, surfactant-stabilized picoliter droplets using nanoelectrospray ionization mass spectrometry. *Analytical Chemistry* **85**, 3812–3816 (2013).
26. Kelly, R. T., Tang, K., Irimia, D., Toner, M. & Smith, R. D. Elastomeric Microchip Electrospray Emitter for Stable Cone-Jet Mode Operation in the Nano-Flow Regime. *Engineering in Medicine* **80**, 3824–3831 (2009).
27. Fidalgo, L. M. *et al.* Coupling Microdroplet Microreactors with Mass Spectrometry: Reading the Contents of Single Droplets Online. *Angewandte Chemie International Edition* **48**, 3665–3668 (2009).
28. Beck, A., Wurch, T., Bailly, C. & Corvaia, N. Strategies and challenges for the next generation of therapeutic antibodies. *Nature Reviews Immunology* **10**, 345–352 (2010).
29. McPherson, M. J. & Hobson, A. D. Pushing the Envelope: Advancement of ADCs Outside of Oncology. in *Antibody-Drug Conjugates* (ed. Tumej, L. N.) 23–36 (Humana New York, NY, 2020).
30. Bargh, J. D., Isidro-Llobet, A., Parker, J. S. & Spring, D. R. Cleavable linkers in antibody–drug conjugates. *Chemical Society Reviews* **48**, 4361–4374 (2019).
31. Su, Z. *et al.* Antibody–drug conjugates: Recent advances in linker chemistry. *Acta Pharmaceutica Sinica B* **11**, 3889–3907 (2021).
32. Tong, J. T. W., Harris, P. W. R., Brimble, M. A. & Kavianinia, I. An Insight into FDA Approved Antibody-Drug Conjugates for Cancer Therapy. *Molecules* **26**, 5847 (2021).
33. Dubowchik, G. M. *et al.* Cathepsin B-labile dipeptide linkers for lysosomal release of doxorubicin from internalizing immunoconjugates: Model studies of enzymatic drug release and antigen-specific in vitro anticancer activity. *Bioconjugate Chemistry* **13**, 855–869 (2002).
34. Nakada, T. *et al.* Novel antibody drug conjugates containing exatecan derivative-based cytotoxic payloads. *Bioorganic and Medicinal Chemistry Letters* **26**, 1542–1545 (2016).
35. Saber, H. & Leighton, J. K. An FDA oncology analysis of antibody-drug conjugates. *Regulatory Toxicology and Pharmacology* **71**, 444–452 (2015).
36. de Goeij, B. E. C. G. & Lambert, J. M. New developments for antibody-drug conjugate-based therapeutic approaches. *Current Opinion in Immunology* **40**, 14–23 (2016).
37. Yang, X. *et al.* Making smart drugs smarter: The importance of linker chemistry in targeted drug delivery. *Medicinal Research Reviews* **40**, 2682–2713 (2020).
38. Wei, B. *et al.* Discovery of Peptidomimetic Antibody-Drug Conjugate Linkers with Enhanced Protease Specificity. *Journal of Medicinal Chemistry* **61**, 989–1000 (2018).

39. Yaghoubi, S. *et al.* Potential drugs used in the antibody–drug conjugate (ADC) architecture for cancer therapy. *Journal of Cellular Physiology* **235**, 31–64 (2020).
40. Khongorzul, P., Ling, C. J., Khan, F. U., Ihsan, A. U. & Zhang, J. Antibody–Drug Conjugates: A Comprehensive Review. *Molecular Cancer Research* **18**, 3–19 (2020).
41. Nejadmoghaddam, M.-R. *et al.* Antibody-Drug Conjugates: Possibilities and Challenges. *Avicenna J Med Biotechnol* **11**, 3–23.
42. Drago, J. Z., Modi, S. & Chandarlapaty, S. Unlocking the potential of antibody–drug conjugates for cancer therapy. *Nature Reviews Clinical Oncology* **18**, 327–344 (2021).
43. Aebersold, R. & Mann, M. Mass spectrometry-based proteomics. *Nature* **422**, 198–207 (2003).
44. Bouslimani, A., Sanchez, L. M., Garg, N. & Dorrestein, P. C. Mass spectrometry of natural products: current, emerging and future technologies. *Natural Product Reports* **31**, 718 (2014).
45. Yates, J. R. Mass spectrometry: from genomics to proteomics. *Trends in Genetics* **16**, 5–8 (2000).
46. Sun, S. & Kennedy, R. T. Droplet Electrospray Ionization Mass Spectrometry for High Throughput Screening for Enzyme Inhibitors. *Analytical Chemistry* **86**, 9309–9314 (2014).
47. Shembekar, N., Chaipan, C., Utharala, R. & Merten, C. A. Droplet-based microfluidics in drug discovery, transcriptomics and high-throughput molecular genetics. *Lab on a Chip* **16**, 1314–1331 (2016).
48. Rivet, C., Lee, H., Hirsch, A., Hamilton, S. & Lu, H. Microfluidics for medical diagnostics and biosensors. *Chemical Engineering Science* **66**, 1490–1507 (2011).
49. Dittrich, P. S. & Manz, A. Lab-on-a-chip: microfluidics in drug discovery. *Nature Reviews Drug Discovery* **5**, 210–218 (2006).
50. Pei, J., Li, Q., Lee, M. S., Valaskovic, G. A. & Kennedy, R. T. Analysis of samples stored as individual plugs in a capillary by electrospray ionization mass spectrometry. *Analytical Chemistry* **81**, 6558–6561 (2009).
51. Kempa, E. E. *et al.* Coupling Droplet Microfluidics with Mass Spectrometry for Ultrahigh-Throughput Analysis of Complex Mixtures up to and above 30 Hz. *Analytical Chemistry* **92**, 12605–12612 (2020).
52. Diefenbach, X. W. *et al.* Enabling Biocatalysis by High-Throughput Protein Engineering Using Droplet Microfluidics Coupled to Mass Spectrometry. *ACS Omega* **3**, 1498–1508 (2018).

53. Holland-Moritz, D. A. *et al.* Mass Activated Droplet Sorting (MADS) Enables High-Throughput Screening of Enzymatic Reactions at Nanoliter Scale. *Angewandte Chemie* **132**, 4500–4507 (2020).
54. Alexandrov, M. L. *et al.* Extraction of ions from solutions under atmospheric pressure as a method for mass spectrometric analysis of bioorganic compounds. *Rapid Communications in Mass Spectrometry* **22**, 267–270 (2008).
55. Fenn, J. B., Mann, M., Meng, C. K., Wong, S. F. & Whitehouse, C. M. Electrospray Ionization for Mass Spectrometry of Large Biomolecules. *Science* **246**, 64–71 (1989).
56. Barinaga, C. J., Edmonds, C. G., Udseth, H. R. & Smith, R. D. Sequence determination of multiply charged peptide molecular ions by electrospray–ionization tandem mass spectrometry. *Rapid Communications in Mass Spectrometry* **3**, 160–164 (1989).
57. Tondeur, Y. *et al.* The determination of protein, oligonucleotide and peptide molecular weights by ion-spray mass spectrometry. *Rapid Communications in Mass Spectrometry* **2**, 249–256 (1988).
58. Banerjee, S. & Mazumdar, S. Electrospray Ionization Mass Spectrometry: A Technique to Access the Information beyond the Molecular Weight of the Analyte. *International Journal of Analytical Chemistry* **2012**, 1–40 (2012).
59. Kebarle, P. & Verkcerk, U. H. Electrospray: From ions in solution to ions in the gas phase, what we know now. *Mass Spectrometry Reviews* **28**, 898–917 (2009).
60. Konermann, L., Ahadi, E., Rodriguez, A. D. & Vahidi, S. Unraveling the Mechanism of Electrospray Ionization. *Analytical Chemistry* **85**, 2–9 (2013).
61. Iavarone, A. T. & Williams, E. R. Supercharging in electrospray ionization: effects on signal and charge. *International Journal of Mass Spectrometry* **219**, 63–72 (2002).
62. Iavarone, A. T. & Williams, E. R. Mechanism of Charging and Supercharging Molecules in Electrospray Ionization. *J Am Chem Soc* **125**, 2319–2327 (2003).
63. Metwally, H., Mcallister, R. G., Popa, V. & Konermann, L. Mechanism of Protein Supercharging by Sulfolane and m-Nitrobenzyl Alcohol: Molecular Dynamics Simulations of the Electrospray Process. *Analytical Chemistry* **88**, (2016).
64. Peters, I., Metwally, H. & Konermann, L. Mechanism of Electrospray Supercharging for Unfolded Proteins: Solvent-Mediated Stabilization of Protonated Sites During Chain Ejection. *Analytical Chemistry* **91**, 6943–6952 (2019).
65. Meyer, J. G. & Komives, E. A. Charge state coalescence during electrospray ionization improves peptide identification by tandem mass spectrometry. *J Am Soc Mass Spectrom* **23**, 1390–1399 (2012).

66. Kjeldsen, F., Giessing, A. M. B., Ingrell, C. R. & Jensen, O. N. Peptide sequencing and characterization of post-translational modifications by enhanced ion-charging and liquid chromatography electron-transfer dissociation tandem mass spectrometry. *Analytical Chemistry* **79**, 9243–9252 (2007).
67. Yost, R. A. & Enke, C. G. Selected ion fragmentation with a tandem quadrupole mass spectrometer. *J Am Chem Soc* **100**, 2274–2275 (1978).
68. Yost, R. A. & Enke, C. G. Triple Quadrupole Mass Spectrometry. *Analytical Chemistry* **51**, 1251A-1264A (1979).
69. Johnson, J. v., Yost, R. A., Kelley, P. E. & Bradford, D. C. Tandem-in-space and tandem-in-time mass spectrometry: triple quadrupoles and quadrupole ion traps. *Analytical Chemistry* **62**, 2162–2172 (1990).
70. Cumisarow, M. B. & Marshall, A. G. Fourier Transform Ion Cyclotron Resonance Spectroscopy. *Chemical Physics Letters* **25**, (1974).
71. Cho, Y., Ahmed, A., Islam, A. & Kim, S. Developments in FT-ICR MS instrumentation, ionization techniques, and data interpretation methods for petroleomics. *Mass Spectrometry Reviews* **34**, 248–263 (2015).
72. Schmid, D. G., Grosche, P., Bandel, H. & Jung, G. FTICR-mass spectrometry for high-resolution analysis in combinatorial chemistry. *Biotechnology and Bioengineering* **71**, 149–61 (2000).
73. Marshall, A. G. & Guant, S. Advantages of High Magnetic Field for Fourier Transform Ion Cyclotron Resonance Mass Spectrometry. *Rapid Communications in Mass Spectrometry* **10**, 1819–1823 (1996).
74. Caravatti, P. & Allemann, M. The ‘infinity cell’: A new trapped-ion cell with radiofrequency covered trapping electrodes for fourier transform ion cyclotron resonance mass spectrometry. *Organic Mass Spectrometry* **26**, 514–518 (1991).
75. Marshall, A. G. (Alan G. & Verdun, F. R. *Fourier transforms in NMR, optical, and mass spectrometry : a user’s handbook*. (Elsevier, 1989).
76. Marshall, A. G. & Verdun, F. R. *Fourier Transforms in NMR, Optical, and Mass Spectrometry*. (Elsevier, 1990).
77. Adamson, J. T. & Hakansson, K. *Electrospray Ionization Fourier Transform Ion Cyclotron Resonance Mass Spectrometry for Lectin Analysis. Lectins: Analytical Technologies* (Elsevier Science B.V., 2007).
78. Makarov, A. Electrostatic axially harmonic orbital trapping: A high-performance technique of mass analysis. *Analytical Chemistry* **72**, 1156–1162 (2000).

79. Hu, Q. *et al.* The Orbitrap: a new mass spectrometer. *Journal of Mass Spectrometry* **40**, 430–443 (2005).
80. Makarov, A. *et al.* Performance evaluation of a hybrid linear ion trap/orbitrap mass spectrometer. *Analytical Chemistry* **78**, 2113–2120 (2006).
81. Zubarev, R. A. & Makarov, A. Orbitrap Mass Spectrometry. *Analytical Chemistry* **85**, 5288–5296 (2013).
82. Hecht, E. S., Scigelova, M., Eliuk, S. & Makarov, A. Fundamentals and Advances of Orbitrap Mass Spectrometry. in *Encyclopedia of Analytical Chemistry* 1–40 (Wiley, 2019).
83. Biemann, K. Appendix 5. Nomenclature for peptide fragment ions (positive ions). in *Methods in Enzymology* vol. 193 886–887 (Academic Press, 1990).
84. McLuckey, S. A. Principles of collisional activation in analytical mass spectrometry. *J Am Soc Mass Spectrom* **3**, 599–614 (1992).
85. Mcluckey, S. A. & Goeringer, D. E. *Slow Heating Methods in Tandem Mass Spectrometry. Journal of the American Society in Mass Spectrometry* vol. 32 (1997).
86. Syka, J. E. P., Coon, J. J., Schroeder, M. J., Shabanowitz, J. & Hunt, D. F. Peptide and protein sequence analysis by electron transfer dissociation mass spectrometry. *Proceedings of the National Academy of Sciences* **101**, 9528–9533 (2004).
87. Kalli, A. & Håkansson, K. Comparison of the electron capture dissociation fragmentation behavior of doubly and triply protonated peptides from trypsin, Glu-C, and chymotrypsin digestion. *Journal of Proteome Research* **7**, 2834–2844 (2008).
88. Good, D. M., Wirtala, M., McAlister, G. C. & Coon, J. J. Performance Characteristics of Electron Transfer Dissociation Mass Spectrometry. *Molecular & Cellular Proteomics* **6**, 1942–1951 (2007).
89. Swaney, D. L. *et al.* Supplemental activation method for high-efficiency electron-transfer dissociation of doubly protonated peptide precursors. *Analytical Chemistry* **79**, 477–485 (2007).
90. Iavarone, A. T., Paech, K. & Williams, E. R. Effects of Charge State and Cationizing Agent on the Electron Capture Dissociation of a Peptide. *Analytical Chemistry* **76**, 2231–2238 (2004).
91. Biemann, K. *et al.* Peptide Sequencing and Characterization of Post-Translational Modifications by Enhanced Ion-Charging and Liquid Chromatography Electron-Transfer Dissociation Tandem Mass Spectrometry. *Proc. Natl. Acad. Sci. U.S.A* **6**, 9243–9252 (1987).
92. Mikesch, L. M. *et al.* The utility of ETD mass spectrometry in proteomic analysis. *Biochimica et Biophysica Acta (BBA) - Proteins and Proteomics* **1764**, 1811–1822 (2006).

93. Pitteri, S. J., Chrisman, P. A. & McLuckey, S. A. Electron-transfer ion/ion reactions of doubly protonated peptides: Effect of elevated bath gas temperature. *Analytical Chemistry* **77**, 5662–5669 (2005).
94. Zhurov, K. O., Fornelli, L., Wodrich, M. D., Laskay, Ü. A. & Tsybin, Y. O. Principles of electron capture and transfer dissociation mass spectrometry applied to peptide and protein structure analysis. *Chemical Society Reviews* **42**, 5014–5030 (2013).
95. Englander, S. W. Hydrogen exchange and mass spectrometry: A historical perspective. *J Am Soc Mass Spectrom* **17**, 1481–1489 (2006).
96. Walter, S. & Kallenbach, N. R. Hydrogen exchange and structural dynamics of proteins and nucleic acids. *Quarterly Review of Biophysics* **16**, 1 (1984).
97. Hvidt, A. & Nielsen, S. O. Hydrogen Exchange in Proteins. *Advances in Protein Chemistry* **21**, 287–386 (1966).
98. Srivastava, A., Nagai, T., Srivastava, A., Miyashita, O. & Tama, F. Role of Computational Methods in Going beyond X-ray Crystallography to Explore Protein Structure and Dynamics. *International Journal of Molecular Sciences* **19**, 3401 (2018).
99. Hoofnagle, A. N., Resing, K. A. & Ahn, N. G. Protein Analysis by Hydrogen Exchange Mass Spectrometry. *Annual Review of Biophysics and Biomolecular Structure* **32**, 1–25 (2003).
100. Chalmers, M. J. *et al.* Probing protein ligand interactions by automated hydrogen/deuterium exchange mass spectrometry. *Analytical Chemistry* **78**, 1005–1014 (2006).
101. Bou-Assaf, G. M. & Marshall, A. G. Biophysical mass spectrometry for biopharmaceutical process development. in *Biophysical Characterization of Proteins in Developing Biopharmaceuticals* 333–374 (Elsevier, 2020).
102. Rand, K. D., Zehl, M. & Jørgensen, T. J. D. Measuring the hydrogen/deuterium exchange of proteins at high spatial resolution by mass spectrometry: Overcoming gas-phase hydrogen/deuterium scrambling. *Accounts of Chemical Research* **47**, 3018–3027 (2014).
103. Fajer, P. G., Bou-Assaf, G. M. & Marshall, A. G. Improved Sequence Resolution by Global Analysis of Overlapped Peptides in Hydrogen/ Deuterium Exchange Mass Spectrometry. *J. Am. Soc. Mass Spectrom* **23**, 1202–1208 (2012).
104. Zehl, M., Rand, K. D., Jensen, O. N. & Jørgensen, T. J. D. Electron transfer dissociation facilitates the measurement of deuterium incorporation into selectively labeled peptides with single residue resolution. *J Am Chem Soc* **130**, 17453–17459 (2008).
105. Rand, K. D., Adams, C. M., Zubarev, R. A. & Jørgensen, T. J. D. Electron capture dissociation proceeds with a low degree of intramolecular migration of peptide amide hydrogens. *J Am Chem Soc* **130**, 1341–1349 (2008).

106. Wang, Q., Borotto, N. B. & Håkansson, K. Gas-Phase Hydrogen/Deuterium Scrambling in Negative-Ion Mode Tandem Mass Spectrometry. *J Am Soc Mass Spectrom* **30**, 855–863 (2019).
107. Abzalimov, R. R., Kaplan, D. A., Easterling, M. L. & Kaltashov, I. A. Protein conformations can be probed in top-down HDX MS experiments utilizing electron transfer dissociation of protein ions without hydrogen scrambling. *J Am Soc Mass Spectrom* **20**, 1514–1517 (2009).
108. Abzalimov, R. R. & Kaltashov, I. A. Controlling hydrogen scrambling in multiply charged protein ions during collisional activation: Implications for top-down hydrogen/deuterium exchange ms utilizing collisional activation in the gas phase. *Analytical Chemistry* **82**, 942–950 (2010).
109. Chakrabarty, S., Romero, E. O., Pyser, J. B., Yazarians, J. A. & Narayan, A. R. H. Chemoenzymatic Total Synthesis of Natural Products. *Accounts of Chemical Tesearch* **54**, 1374–1384 (2021).
110. Li, J., Amatuni, A. & Renata, H. Recent advances in the chemoenzymatic synthesis of bioactive natural products. *Current Opinion in Chemical Biology* **55**, 111–118 (2020).
111. Tao, J. & Xu, J. H. Biocatalysis in development of green pharmaceutical processes. *Current Opinion in Chemical Biology* **13**, 43–50 (2009).
112. Yi, D. *et al.* Recent trends in biocatalysis. *Chemical Society Reviews* **50**, 8003–8049 (2021).
113. Chun, S. W., Hinze, M. E., Skiba, M. A. & Narayan, A. R. H. Chemistry of a Unique Polyketide-like Synthase. *J Am Chem Soc* **140**, 2430–2433 (2018).
114. Chun, S. W. & Narayan, A. R. H. Biocatalytic Synthesis of α -Amino Ketones. *Synlett* **30**, 1269–1274 (2019).
115. Tsuchiya, S. *et al.* Synthesis and identification of proposed biosynthetic intermediates of saxitoxin in the cyanobacterium *Anabaena circinalis* (TA04) and the dinoflagellate *Alexandrium tamarense* (Axat-2). *Organic & Biomolecular Chemistry* **12**, 3016–3020 (2014).
116. Chun, S. W. Chemoenzymatic Synthesis of Chiral Amines by Carrier Protein-Dependent Enzymes. (2022).
117. Wang, Y. *et al.* Directed Evolution: Methodologies and Applications. *Chemical Reviews* **121**, 12384–12444 (2021).
118. Packer, M. S. & Liu, D. R. Methods for the directed evolution of proteins. *Nature Reviews Genetics* **16**, 379–394 (2015).
119. Arnold, F. H. Directed Evolution: Bringing New Chemistry to Life. *Angewandte Chemie International Edition* **57**, 4143–4148 (2018).

120. Arnold, F. H. Design by Directed Evolution. *Accounts of Chemical Research* **31**, 125–131 (1998).
121. Sun, S., Slaney, T. R. & Kennedy, R. T. Label free screening of enzyme inhibitors at femtomole scale using segmented flow electrospray ionization mass spectrometry. *Analytical Chemistry* **84**, 5794–5800 (2012).
122. Myers, J. N., Rekhadevi, P. & Ramesh, A. Comparative Evaluation of Different Cell Lysis and Extraction Methods for Studying Benzo(a)pyrene Metabolism in HT-29 Colon Cancer Cell Cultures. *Cellular Physiology and Biochemistry* **2**, 209–218 (2011).
123. Ser, Z., Liu, X., Tang, N. N. & Locasale, J. W. Extraction parameters for metabolomics from cultured cells. *Analytical Biochemistry* **475**, 22–28 (2015).
124. Liang, Y., Neta, P., Yang, X. & Stein, S. E. Collision-Induced Dissociation of Deprotonated Peptides. Relative Abundance of Side-Chain Neutral Losses, Residue-Specific Product Ions, and Comparison with Protonated Peptides. *J Am Soc Mass Spectrom* **29**, 463–469 (2018).
125. Zhang, P. *et al.* Revisiting Fragmentation Reactions of Protonated α -Amino Acids by High-Resolution Electrospray Ionization Tandem Mass Spectrometry with Collision-Induced Dissociation. *Scientific Reports* **9**, 6453 (2019).
126. Poreba, M. Protease-activated prodrugs: strategies, challenges, and future directions. *The FEBS Journal* **287**, 1936–1969 (2020).
127. Kramer, L., Turk, D. & Turk, B. The Future of Cysteine Cathepsins in Disease Management. *Trends in Pharmacological Sciences* **38**, 873–898 (2017).
128. Turk, V. *et al.* Cysteine cathepsins: From structure, function and regulation to new frontiers. *Biochimica et Biophysica Acta - Proteins and Proteomics* **1824**, 68–88 (2012).
129. Gondi, C. S. & Rao, J. S. Cathepsin B as a cancer target. *Expert Opinion on Therapeutic Targets* **17**, 281–291 (2013).
130. Mitrović, A., Mirković, B., Sosič, I., Gobec, S. & Kos, J. Inhibition of endopeptidase and exopeptidase activity of cathepsin B impairs extracellular matrix degradation and tumour invasion. *Biological Chemistry* **397**, 164–174 (2016).
131. Turk, D. & Gunčar, G. Lysosomal cysteine proteases (cathepsins): Promising drug targets. *Acta Crystallographica - Section D Biological Crystallography* **59**, 203–213 (2003).
132. Schechter, I. & Berger, A. On the size of the active site in proteases. I. Papain. *Biochemical and Biophysical Research Communications* **27**, 157–162 (1967).
133. Biniössek, M. L., Nägler, D. K., Becker-Pauly, C. & Schilling, O. Proteomic Identification of Protease Cleavage Sites Characterizes Prime and Non-prime Specificity of Cysteine Cathepsins B, L, and S. *Journal of Proteome Research* **10**, 5363–5373 (2011).

134. Salomon, P. L. *et al.* Optimizing Lysosomal Activation of Antibody–Drug Conjugates (ADCs) by Incorporation of Novel Cleavable Dipeptide Linkers. *Molecular Pharmaceutics* **16**, 4817–4825 (2019).
135. Illy, C. *et al.* Role of the Occluding Loop in Cathepsin B Activity. *Journal of Biological Chemistry* **272**, 1197–1202 (1997).
136. Caculitan, N. G. *et al.* Cathepsin B is dispensable for cellular processing of cathepsin B-cleavable antibody–drug conjugates. *Cancer Research* **77**, 7027–7037 (2017).
137. MacLean, B. *et al.* Skyline: an open source document editor for creating and analyzing targeted proteomics experiments. *Bioinformatics* **26**, 966–968 (2010).
138. Nakada, T. *et al.* Novel antibody drug conjugates containing exatecan derivative-based cytotoxic payloads. *Bioorganic & Medicinal Chemistry Letters* **26**, 1542–1545 (2016).
139. Shiose, Y., Ochi, Y., Kuga, H., Yamashita, F. & Hashida, M. Relationship between Drug Release of DE-310, Macromolecular Prodrug of DX-8951f, and Cathepsins Activity in Several Tumors. *Biological and Pharmaceutical Bulletin* **30**, 2365–2370 (2007).
140. Harada, M., Sakakibara, H., Yano, T., Suzuki, T. & Okuno, S. Determinants for the drug release from T-0128, camptothecin analogue-carboxymethyl dextran conjugate. *Journal of Controlled Release* **69**, 399–412 (2000).
141. Jia, Z. *et al.* Crystal structures of recombinant rat cathepsin B and a cathepsin B-inhibitor complex: Implications for structure-based inhibitor design. *Journal of Biological Chemistry* **270**, 5527–5533 (1995).
142. Turk, D. *et al.* Crystal Structure of Cathepsin B Inhibited with CA030 at 2.0-Å Resolution: A Basis for the Design of Specific Epoxysuccinyl Inhibitors. *Biochemistry* **34**, 4791–4797 (1995).
143. Li, W. *et al.* Antibody Aggregation: Insights from Sequence and Structure. *Antibodies* 2016, Vol. 5, Page 19 **5**, 19 (2016).
144. Singh, R. *et al.* A New Triglycyl Peptide Linker for Antibody–Drug Conjugates (ADCs) with Improved Targeted Killing of Cancer Cells. *Molecular Cancer Therapeutics* **15**, 1311–1320 (2016).
145. Dai, Z. *et al.* Synthesis of site-specific antibody-drug conjugates by ADP-ribosyl cyclases. *Science Advances* **6**, (2020).
146. McGrath, M. E., Palmer, J. T., Brömme, D. & Somoza, J. R. Crystal structure of human cathepsin S. *Protein Science* **7**, 1294–1302 (1998).
147. Fujishima, A. *et al.* The crystal structure of human cathepsin L complexed with E-64. *FEBS Letters* **407**, 47–50 (1997).

148. Turk, B., Turk, D. & Turk, V. Lysosomal cysteine proteases: more than scavengers. *Biochimica et Biophysica Acta (BBA) - Protein Structure and Molecular Enzymology* **1477**, 98–111 (2000).
149. Lübke, T., Lobel, P. & Sleat, D. E. Proteomics of the lysosome. *Biochimica et Biophysica Acta (BBA) - Molecular Cell Research* **1793**, 625–635 (2009).
150. Bolleddula, J. *et al.* Pharmacokinetics and Catabolism of [3H]TAK-164, a Guanylyl Cyclase C Targeted Antibody-Drug Conjugate. *Drug Metabolism and Disposition* **48**, 1239–1245 (2020).
151. Schmitz, J. *et al.* Cathepsin B: Active site mapping with peptidic substrates and inhibitors. *Bioorganic & Medicinal Chemistry* **27**, 1–15 (2019).
152. Oganesyan, I., Lento, C. & Wilson, D. J. Contemporary hydrogen deuterium exchange mass spectrometry. *Methods* **144**, 27–42 (2018).
153. Hamuro, Y. Quantitative Hydrogen/Deuterium Exchange Mass Spectrometry. *J Am Soc Mass Spectrom* **32**, 2711–2727 (2021).
154. Masson, G. R., Jenkins, M. L. & Burke, J. E. An overview of hydrogen deuterium exchange mass spectrometry (HDX-MS) in drug discovery. *Expert Opinion on Drug Discovery* **12**, 981–994 (2017).
155. Zehl, M., Rand, K. D., Jensen, O. N. & Jorgensen, T. J. D. Electron transfer dissociation facilitates the measurement of deuterium incorporation into selectively labeled peptides with single residue resolution. *J Am Chem Soc* **130**, 17453–17459 (2008).
156. Rand, K. D., Zehl, M., Jensen, O. N. & Jørgensen, T. J. D. Protein hydrogen exchange measured at single-residue resolution by electron transfer dissociation mass spectrometry. *Analytical Chemistry* **81**, 5577–5584 (2009).
157. Li, X., Li, Z., Xie, B. & Sharp, J. S. Supercharging by *m*-NBA Improves ETD-Based Quantification of Hydroxyl Radical Protein Footprinting. *J Am Soc Mass Spectrom* **26**, 1424–1427 (2015).
158. Möller, I. R. *et al.* Improving the Sequence Coverage of Integral Membrane Proteins during Hydrogen/Deuterium Exchange Mass Spectrometry Experiments. *Analytical Chemistry* **91**, 10970–10978 (2019).
159. Wang, Q. Protein-Protein Interaction Analysis: Expanded Hydrogen/Deuterium Exchange Tandem Mass Spectrometry and Host Cell Protein Characterization. (2019).
160. Umezawa, H. *et al.* Pepstatin, a new pepsin inhibitor produced by Actinomycetes. *The Journal of Antibiotics* **23**, 259–262 (1970).
161. Marciniszyn, J., Hartsuck, J. A. & Tang, J. Mode of inhibition of acid proteases by pepstatin. *Journal of Biological Chemistry* **251**, 7088–7094 (1976).

162. Eng, J. K., Fischer, B., Grossmann, J. & MacCoss, M. J. A fast SEQUEST cross correlation algorithm. *Journal of Proteome Research* **7**, 4598–4602 (2008).
163. Frank, A. M. A Ranking-Based Scoring Function for Peptide–Spectrum Matches. *Journal of Proteome Research* **8**, 2241–2252 (2009).
164. Leemhuis, H., Kelly, R. M. & Dijkhuizen, L. Directed evolution of enzymes: Library screening strategies. *IUBMB Life* **61**, 222–228 (2009).
165. Cybulski, O., Jakiela, S. & Garstecki, P. Whole Teflon valves for handling droplets. *Lab on a Chip* **16**, 2198–2210 (2016).
166. Hébert, M., Huissoon, J. & Ren, C. L. A perspective of active microfluidic platforms as an enabling tool for applications in other fields. *Journal of Micromechanics and Microengineering* **32**, 043001 (2022).
167. della Valle, M. C. *et al.* Classification of Subcellular Location by Comparative Proteomic Analysis of Native and Density-shifted Lysosomes. *Molecular & Cellular Proteomics* **10**, 1–14 (2011).